Energy Transfer Kinetics in Mn-doped Lead Halide Perovskite Nanocrystals

Hyejin Choe

Department of Chemistry

The Graduate School of Sungshin Women's University

Energy Transfer Kinetics in Mn-doped Lead Halide Perovskite Nanocrystals

A Master's Thesis

Submitted to the

Graduate School of Sungshin Women's University

in partial fulfillment of the requirements

for the degree of

Master of Science

Hyejin Choe

Dec, 2023

This is to certify that we have examined the

Master's Thesis of

Hyejin Choe

Submitted to Department of Chemistry

Approved as to style and content:

Committee Chairman: Minjeong Shin

Committee Member: Seongsoon Park Seong Soon Park

Committee Member: Junsang Cho

The Graduate School of Sungshin Women's University

ABSTRACT

Understanding Energy Transfer Kinetics and Mechanism in Mn−doped Lead Halide Perovskite Nanocrystals

Hyejin Choe
Department of Chemistry
Graduate School of
Sungshin Women's University

The introduction of Mn into lead halide perovskite provides considerable opportunities for the improvement of its optoelectronic and magnetic properties. However, an understanding of the complicated dynamics in excited states is necessarily required to fully understand the excited states dynamics within host lattices and competing energy transfer between exciton and dopant. It is challenging to predict Mn sensitization in perovskite nanocrystals because of the competing energy transfer processes, exciton recombination, and Mn recombination, which complicate the excited interactions. Here, we studied the competing processes between exciton recombination and exciton−to−Mn energy transfer dynamics in $CsPb(Cl_{1-y}Br_y)_3$ nanocrystals (vice versa) by systematically controlling the Mn concentration and halide composition. And we created a machine learning−guided model to predict the degree of Mn sensitization. The K−nearest neighbor (KNN) based machine learning model and the lifetime using time−correlated single photon counting (TCSPC) measurements allows for elucidating the competing exciton−to−energy transfer kinetics in Mn−doped halide perovskites. The understanding of these competitive energy transfer processes can provide insights into how to fully utilize the dual emission properties of transition Mn−doped lead halide perovskite nanocrystals. Also, our machine learning−based approaches not only facilitates efficient navigation the vast reaction design space, but also provide us with valuable insight into complex physical phenomena.

TABLE OF CONTENTS

LIST OF FIGURES

LIST OF TABLES

CHAPTER I

Introduction

Structure and properties of Perovskites

A lot of attention has been paid to metal halide perovskites (MHPs) as promising materials for the fabrication of solar cells, light−emitting diodes (LEDs), lasers, photodetectors, and photo−catalysts.[3–8] They have high efficiency and remarkable optoelectronic properties such as high photoluminescence quantum yield (PLQY), high color purity and adjustable emission wavelengths and band gap.[8–11] MHPs have advanced substantially over the last decade, both in terms of their fundamental understanding and potential applications.[12–17] The convenience of tuning the emission wavelength, combined with high PLQY and moisture stability, has led to extensive studies on perovskite LEDs.[18–21] These studies aim to enhance performance characteristics such as external quantum efficiency (EQE), LED lifetime, and overall stability. PeLEDs with red, green, and blue EQEs achieved peak values of 24.4%[22], 28.1%[23], and 13.8%[24], respectively. And particularly, the emission of Mn^{2+} ions around ~600nm can avoid reabsorption of exciton emission due to the distinct absorption of the perovskite host. Therefore, it is possible to apply it to solar cells, and Mn^{2+} doped $CsPbCl_3$ NC solar cells have been successfully manufactured.[25,26]

Moreover, extensive researches have led to an improvement in power conversion efficiency of perovskite solar cell from 3.8% to 25%.[27,28]

The general formula of three-dimensional (3D) perovskites is ABX_3, where A is a monovalent cation, such as methylammonium ($CH_3NH_3^+$), formamidinium ($NH_2CHNH_2^+$). B is metal cation, typically Pb^{2+} or Sn^{2+} and X is halide (Cl^-, Br^-, I^-).[29,30] **(Figure I.1)** At the B site, six nearest neighboring anion X sites are located, while the A sites are located within the structure composed of corner-sharing BX_6 octahedra. The structure-property relationships are affected by the ability to adjust numerous elements in combinations.[31] Unlike other semiconductor materials, MHPs have strong ionic bonding properties, which enable the formation of highly crystalline nanocrystals (NCs).[32,33] Moreover, MHPs can easily adjust their bandgap, size and dimension by changing halide composition, synthesis temperature, and controlling ligands.[8,32,33]

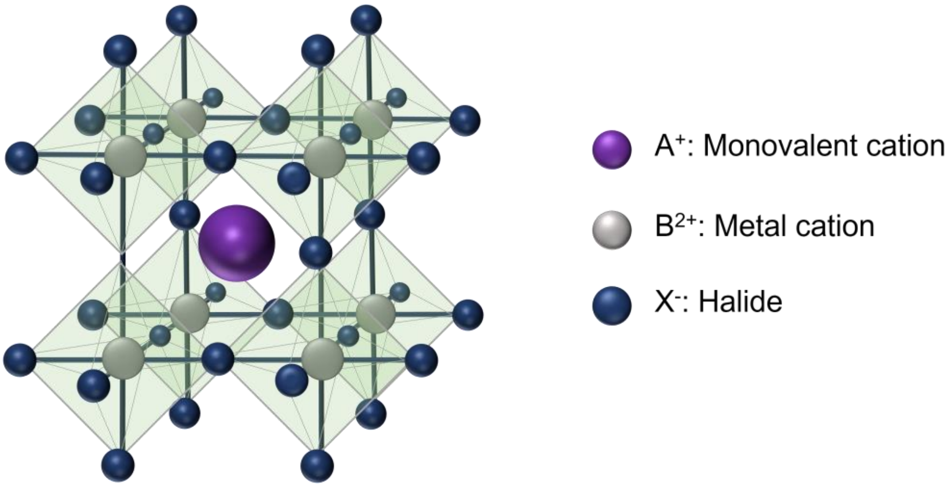

Figure I.1. Illustration of crystal structure of three-dimensional (3D) perovskites

Doping and Characteristic of Mn Emission

Doping is the process of introducing additives into a semiconductor lattice.[34] While it can give the semiconductor unique chemical and physical properties, the core structure of the host lattice and its fundamental properties remain unchanged.[35–39] The doping process adds small amounts of additives to a semiconductor, which is different from alloying.

For II–VI semiconductors, transition metal doping with elements like Mn^{2+}, Cu^{2+}, Ni^{2+}, Bi^{3+}, K^{+}, and lanthanides has been widely studied to change their electrical, magnetic, and optical properties.[10,40–47] The doping of such transition metals has led to impressive change in optical properties, such as the increase in PLQY, enhanced stability, and the emergence of new emissions, which are beneficial for the enhancing the performance of optoelectronic devices.[45,46] In particular, Mn doping has been extensively researched among transition metals. Since the Mn emission with a long lifetime, increased PLQY, and reduced defect state density are advantageous for optoelectronic device applications.[36,39,48] Manganese ion (Mn^{2+}) is a transition metal which the atomic number is 25. The common oxidation states of manganese ion can be varied from +2, +3, +4, +6, and +7, with the +2 state being the most thermodynamically stable.[49]

When Mn^{2+} is doped into quantum dots, a new orange-red emission arises in the wavelength range of 580–600nm.[50] The electronic states of d^5 ions can be shown as Tanabe–Sugano diagrams. **(Figure I.2)** [51]

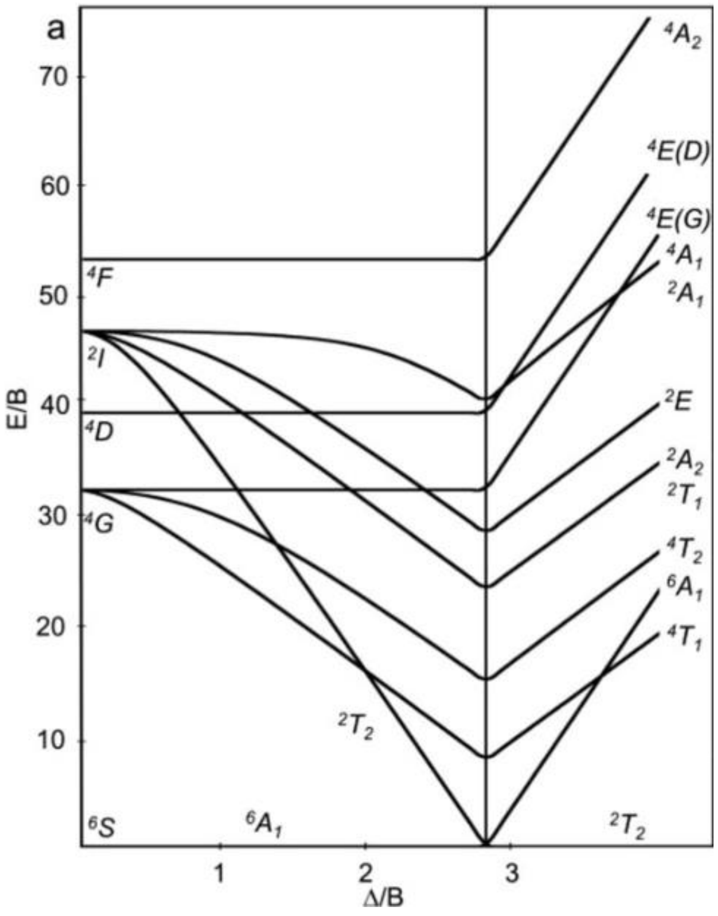

Figure I.2. Tanabe−Sugano diagram for d^5 electronic states in octahedral complex. B is a Racah parameter. Reprinted with permission from ref [51]. Copyright 2021 Elsevier.

The emission properties of Mn^{2+} can be influenced by its coordination geometry and the surrounding ligand environment. As depicted in the Tanabe−Sugano diagram, Mn emission can shift from green to red depending on the strength of the crystal field. When it comes to lead halide perovskite, Mn^{2+} has an octahedral coordination with halides, which shows an orange−red emission.[52] Many studies have shown that the emission of Mn^{2+} originates from the transition between the $^4T_1$ and $^6A_1$ states, which are the lowest energy multiplets in the Mn^{2+} ion with crystal field strength.[53–55] The transition between the $^4T_1$ excited state and the $^6A_1$

ground state produces visible PL for Mn^{2+} ions. [56] As a consequence of spin–forbidden d–d transitions between $^4T_1$ and $^6A_1$, Mn^{2+} has an emission that shows a long–lived decay time.[39,45,52] While the exciton lifetime of the semiconductor host is short on nanosecond scale, the decay lifetime of Mn emission is much longer on the microsecond to millisecond scales. The d electrons of the Mn^{2+} ion typically exist in a high–spin state in octahedral coordination.[52] It implies that there are three electrons of parallel spin in the t_{2g} orbitals and two in the e_g orbitals.[52] Spin selection rules prohibit transitions between states with different spin multiplicities. In this rule, transitions are permitted only when the total intrinsic spin ($\triangle S$) is same. Therefore, in d–d transitions, when electrons in the t_{2g} orbitals move to the e_g orbitals, they must move in such a way that their spin direction is antiparallel to the electrons in the e_g orbitals. Also, parity allowed transitions must have the different orbital angular momentum, $\triangle l = \pm 1$. However, the $^4T_1$–$^6A^1$ transition in Mn^{2+} is both spin– and parity–forbidden transition, which produce an emission with a long PL lifetime.[57]

When the amount of Mn dopant increases or incorporated into hosts with heavier atoms, the manganese ion PL decay time can be shortened by the spin–orbit coupling of Mn–Mn pairs or magnetic exchange interaction.[58]

Energy transfer in Mn-doped halide perovskites

The Mn photoluminescence in Mn-doped quantum dots is a consequence of the exchange coupling caused by the wave function overlap between the d electrons of Mn dopant and the exciton. [59,60] Therefore, the chemical composition and structure of the Mn-doped samples determine the strength of the exchange coupling between exciton and Mn dopant. Especially, the size of nanocrystals and spatial distribution can be important factor for the exchange coupling.[2,61] The quantum confinement effect in II-VI quantum dots enhances the exchange coupling between the exciton and Mn dopant, leading to an increased rate of energy transfer from exciton to Mn. [2,62] The excitation within the Mn d-state cannot occur directly due to the forbidden transition. It can be only sensitized by the excitation of the NCs host and energy transfer.[63] Thus, the photo-excited electron and hole pair within the host is most important for Mn-d state excitation. When the sufficient high-energy photons are absorbed within the host, electron gets excited to the unoccupied level, then they produce an electron-hole pair (exciton). As the electron and hole are combined, it leads to the release of a bandgap emission. However, from the excited state, some of charge carriers are transferred to Mn through the energy transfer process, causing a d-d transition of Mn. Within the doped framework, the energy of the electron-hole pair is transferred to sensitize the $^4T_1$ state of the Mn^{2+} ion. **(Figure I.3A)**

This energy transfer process occurs quickly within picosecond scale.[64] However, in perovskite nanocrystals, the energy transfer occurs on a sub−nanosecond scale (~ns), which is notably slower than II−VI

The d−d transition of Mn emission is a spin and parity forbidden transition, which leads to a very long lifetime in the μs~ms time scale.[63,65] It is important to note that the rate of exciton−to−dopant energy transfer is faster than that of the d−d transition of Mn. If the energy transfer rate were not fast, the primary pathway would have been excitonic recombination or non−radiative decay via surface trap states rather than through the Mn d−d transition. [66] The decay lifetime associated with surface states typically appears in less than nano seconds, and it is faster than the bandgap recombination. This is why passivating the surface is essential to achieve effective band−edge emission.[66] **(Figure I.3B)**

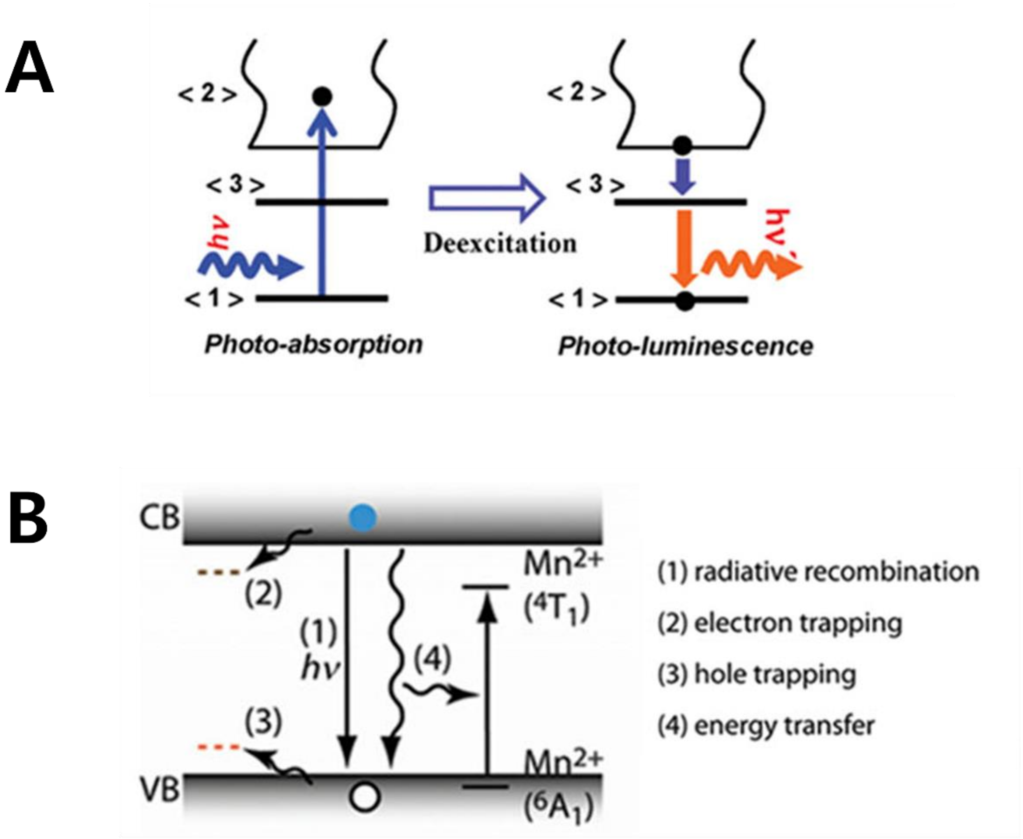

Figure I.3. (A) Schematic of energy diagram of the exciton and recombination process in Mn-doped quantum dots. Reprinted with permission from ref [1]. Copyright 2011 America Chemical Society. (B) Energy transfer processes in Mn-doped semiconductor nanocrystals. Reprinted with permission from ref [2]. Copyright 2011 America Chemical Society.

Energy transfer occurs from excited electron-hole pairs in the band gap to the Mn results in the excited Mn states, but defect states can also activate Mn d-d transitions.[66,67] **(Figure I.4)** The radiative decay appears from the $^4T_1$ state to the $^6A_1$ state of the excited Mn^{2+}, and this dopant emission shows a red-shifted emission compared to the excitonic emission.[52] The energy transfer to the surface trap states competes with the energy transfer to the exciton−to−Mn. However, since there is also a possibility of energy transfer from the surface trap state to Mn, the Mn emission is relatively less sensitive even with higher surface states than undoped samples.[68–72] It means that even the nanocrystals are not fully passivated and have numerous surface states, they can produce the narrow dopant emission. In the host of nanocrystal, the excited electron−hole pair follows a non−radiative Auger−like recombination process to transfer energy from the host to Mn^{2+}, enabling the Mn^{2+} to be excited from the $^6A_1$ ground state to the $^4A_1$ state.[73] The Auger recombination process occurs when an electron wandering in the conduction band collides with another electron, transferring its lost energy to the collided electron, which then drops to the valence band and recombines with a hole. The electron that gained energy transitions to a higher energy level, then loses energy and drops to the boundary of the conduction band, with the energy release occurring in a stepwise manner. [74]

semiconductor nanocrystals.[75,76] This discrepancy may be attributed to the antiferromagnetic coupling of Mn^{2+} ions with stronger coupling observed in lead halide nanocrystals than in II−VI quantum dots. [77]

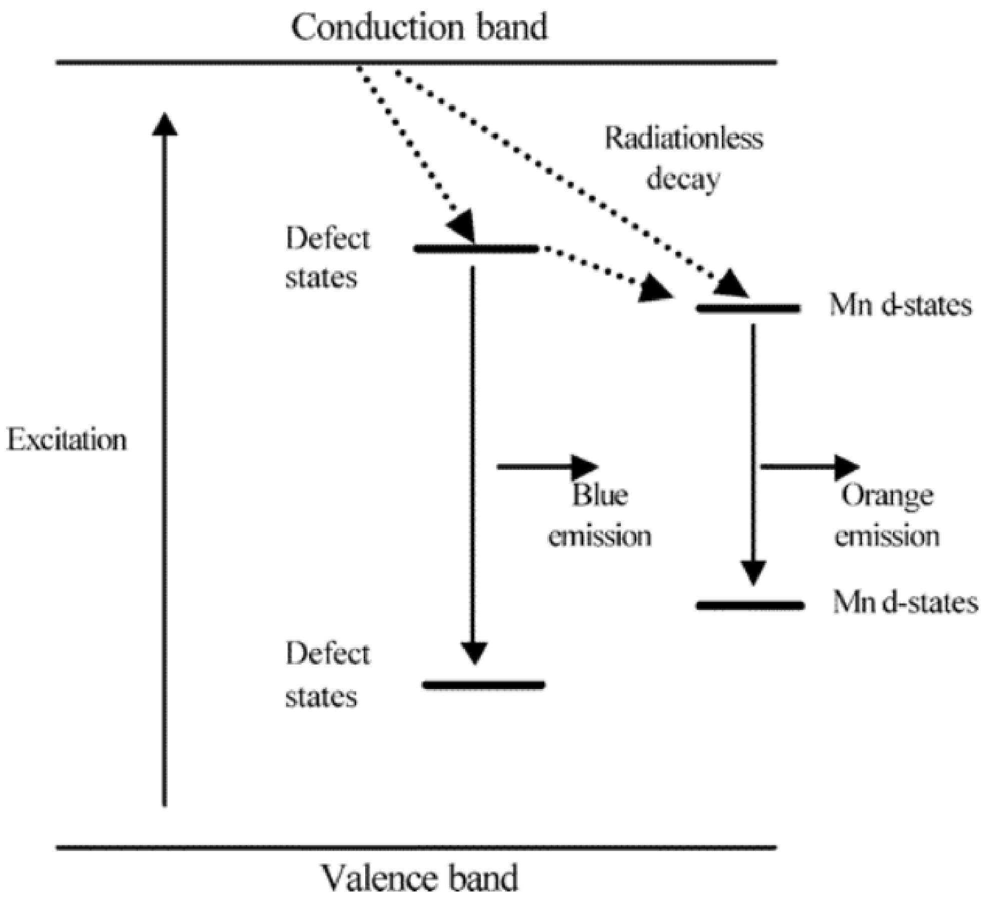

Figure I.4. Schematic for the decay channels through defect state. Reprinted with permission from ref [66]. Copyright 2005 America Chemical Society.

Machine Learning for Predicting Material Characteristics

A machine learning is a subset of artificial intelligence in which computers learn patterns from data and analyze them to improve model performance.[78] It is rapidly advancing among scientists in the artificial intelligence field as well as experts in various other fields who utilize these tools. Especially, the machine learning is helpful as a tool for scientists to find new materials or predicting material properties. For example, scientists can find efficient solar cell materials, predict shape and size in organic materials, predict accurate band gap of inorganic materials using machine learning.[79–81]

The first step to start machine learning is to obtain and select the proper data. **(Figure I.5)** For this procedure, the researcher must consider the type, quality, and format of the data to acquire good results.[82] After data selection, it is essential to extract features of the data related to the target. In cases with abundant data characteristics, feature selection with manual can be difficult. Using deep learning tool can be helpful to overcome these issues.[83] Machine learning is categorized into supervised learning, unsupervised learning, and semi−supervised learning.[84] Supervised learning is a method of machine learning that deduces a function from training data. [85] The training data typically includes properties of the input objects in vector form, and each vector is labeled with the desired outcome. A supervised learning requires an understanding of the relationship between an input variable X and an output variable Y. This relationship is then used to predict outputs for data that has not been observed before. Supervised learning is important in machine learning and has significant relevance in multidata processing.[85] Supervised learning is divided into classification and regression. Classification is an algorithm that categorizes given data based on specific categories. On the other hand, regression predicts continuous values based on the features of certain data. This is primarily used to predict trends of the data. Unlike supervised learning, this is a learning method that predicts the future by clustering similar data without providing the correct results. Unsupervised learning is sometimes used as a preprocessing technique to identify appropriate features in supervised learning.[86] In this study, we used supervised learning with regression to predict the trend of the energy transfer in Mn−doped perovskite nanocrystals.

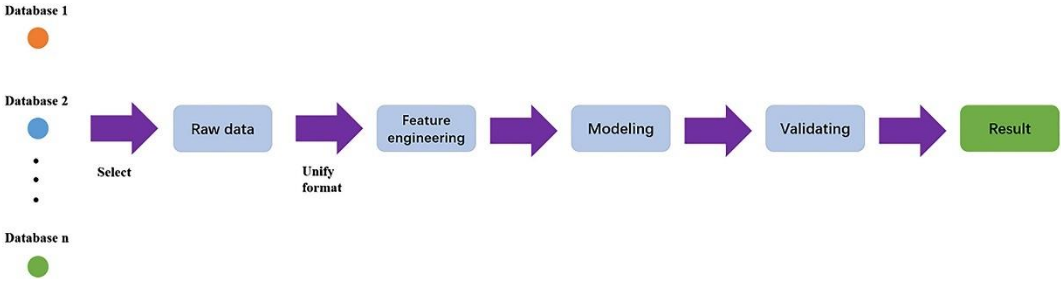

Figure I.5. Workflow of machine learning. Reprinted with permission from ref [82]. Copyright 2019 John Wiley and Sons.

CHAPTER II

Exciton Recombination versus Energy Transfer: Mapping Competing Excited-State Dynamics in Various Mn-Doped $CsPb(Cl_{1-y}Br_y)_3$ Perovskite Nanocrystals *

II.1 EXPERIMENTAL

Materials

Cesium carbonate (Cs_2CO_3, 99.9%, Alfa Aesar), lead chloride ($PbCl_2$, 99%, Alfa Aesar), lead bromide ($PbBr_2$, 98.5%, Alfa Aesar), manganese(II) chloride tetrahydrate ($MnCl_2 \cdot 4H_2O$, 98+%, Sigma-Aldrich), oleic acid (OA, 90%, Sigma-Aldrich), oleylamine (OLAm, 70%, Sigma-aldrich), 1-octadecene (ODE, 90%, Sigma-Aldrich), hexane (Samchun Chemicals, 96%). All chemicals were used without any further purification after received from manufacturers.

Preparation of Cesium oleate (Cs-OA)

The preparation of Cs-oleate adapts the previously reported literatures.[87] Briefly, Cs_2CO_3 (0.4 g), OA (1.25 mL), and ODE (15 mL) were

---

* Reprinted with permission from "Exciton Recombination versus Energy Transfer: Mapping Competing Excited-State Dynamics in Various Mn-Doped $CsPb(Cl_{1-y}Br_y)_3$ Perovskite Nanocrystals for Achieving White Light Emission" by H.Choe, H.Jin, S.J.Lee, J.Cho., *ACS Appl. Nano Mater.* 2022, 5, 12, 18385-18395. ©2022 American Chemical Society. All rights reserved.

mixed into a 20 mL vial under heating at 150 ℃ using a hot plate for 1 hr until the solid inside was dissolved to make a clear solution. The yellowish solution was stored at room temperature and used for the synthesis of $CsPbCl_3$ or Mn-doped $CsPbCl_3$ nanocrystals. Before use of the Cs-OA, if the solution turned into cloudy, it was gently heated at 120 ℃ to make a transparent solution.

Synthesis of undoped $CsPbCl_3$ and Mn-doped $CsPbCl_3$ nanocrystals.

Synthesis of undoped versus Mn-doped $CsPbCl_3$ nanocrystals is illustrated in **Figure II.1**. For the synthesis of $CsPbCl_3$ nanocrystals, briefly, a $PbCl_2$ (0.2 mmol; 0.0556 g), OA (0.5 mL), OLAm (0.5 mL), and ODE (5 mL) were loaded into a 50 mL 3-neck round bottom flask, heated at 105 ℃ under vigorous stirring, and degassed under for 30 min. The reaction mixture was further heated to 185 ℃ under N_2 flow. Once the temperature reaches at 185 ℃, as-prepared Cs-oleate (0.45 mL) solution was swiftly injected into the flask. After 10 sec, the reaction was quickly quenched by putting the flask into an ice-water bath. For the synthesis of Mn-doped $CsPbCl_3$ with different Mn concentration, the mole fraction of Mn defined as x in the precursor stoichiometry of Mn/(Mn+Pb) was systematically varied in the range of x = 0-0.8. As a representative example, for x = 0.44, a $PbCl_2$ (0.111 mmol; 0.0309 g), $MnCl_2 \cdot 4H_2O$ (0.089 mmol; 0.0176 g), OA (0.5 mL), OLAm (0.5 mL) and ODE (5 mL) were added into a 50 mL 3-neck round bottom flask. The other remaining synthetic process for the Mn doping was identical with the synthesis of undoped $CsPbCl_3$

nanocrystals. For the purification of the synthesized nanocrystals, the reaction solution was spun down at 4000 rpm for 10 min. The precipitates were taken while the supernatant solution was thrown away. The precipitates were further resuspended in 3 mL of hexanes (corresponding to $CsPbCl_3$ 66 nM with $\varepsilon = 4.5*10^6\ M^{-1}cm^{-1}$)[88–90] for further reactions and characterizations.

Anion exchange reaction for Mn-doped $CsPb(Cl_{1-y}Br_y)_3$.

First, a 0.05 M lead bromide ($PbBr_2$) precursor solution were prepared by dissolving a $PbBr_2$ (0.4 mmol; 0.147 g) into a mixed solution including OA (0.5 mL), OLAm (0.5 mL) and ODE (7 mL) in a 20 mL vial. The reaction mixture was further heated at 150℃ to make a transparent bromide precursor solution. For the anion exchange reaction, a 0.5 mL of Mn-doped $CsPbCl_3$ nanocrystals (66 nM) were loaded into a 5mL vial in which lead bromide solution (0.05 M) was added under vigorous stirring. Depending on the amount of added bromide source, the stoichiometric ratio of Cl/Br in the resulting nanocrystals of $CsPb(Cl_{1-y}Br_y)_3$ were determined. When the anion exchange was complete, the nanocrystals were purified by adding ethyl acetates 6 mL and centrifuged at 4000 rpm. The precipitates were taken and redispersed in hexanes for further characterizations.

Characterizations

UV-vis absorption spectra were acquired using a Cary 60 UV-vis spectrophotometer system (Agilent Technology) in the spectral range of 300-800nm with a scan rate of 4800 nm/min. The Photoluminescence (PL) emission spectra were obtained using Ocean Optics Spectrometer using a 365 nm excitation diode laser and Ocean HDX (FM-OH100) as a photodetector. The PL lifetime was collected using a fluorescence lifetime spectrometer (Fluorolog-QM, Horiba) and PL decay traces were further fitted with multiexponential functions. The PL quantum yield (QY) of nanocrystals dispersed in hexanes solution were acquired using an absolute PL quantum yield spectrometer (C13534, Hamamatsu) with 365 nm excitation wavelength. The transmission electron microscopy (TEM) images were taken using a JEM-2100F (HR) (JEOL LTD) at an operating voltage at 200kV.

Determination of recombination rate constants of exciton and Mn using PL QY

Corersponding PL QY meausred from absolute PL QY instrument can be further expressed using two different competing PL decay terms mainly including radiative and non-radiative recombinations (k_r and k_{nr}) for exciton and Mn emission, respectively, as seen in the following equation (1).

$$\mathrm{PL\ QY}^{Exciton} = \frac{k_r^{Exciton}}{k_r^{Exciton}+k_{nr}^{Exciton}}\ ,\quad \mathrm{PL\ QY}^{Mn} = \frac{k_r^{Mn}}{k_r^{Mn}+k_{nr}^{Mn}} \qquad (1)$$

where the radiative and non−radiative recombination rate constants of exciton were expressed as $k_r^{Exciton}$ and $k_{nr}^{Exciton}$ whereas those of Mn^{2+} ions as k_r^{Mn} and k_{nr}^{Mn}, respectively.

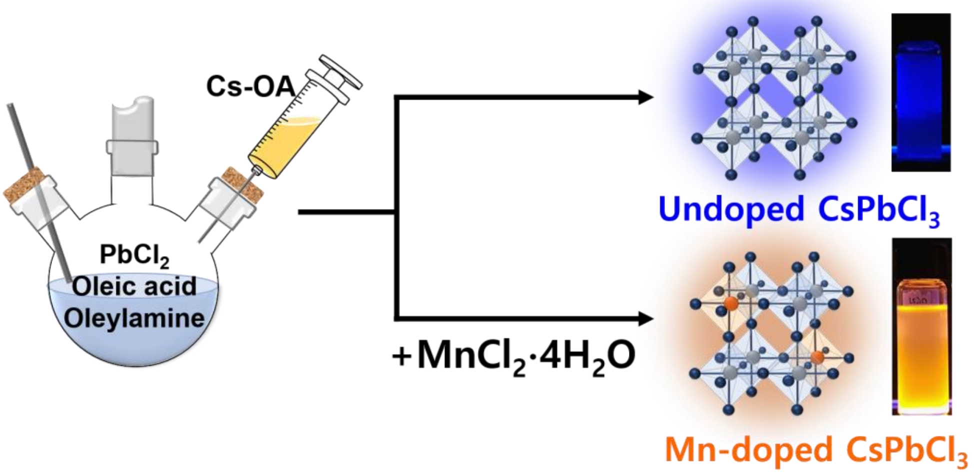

Figure II.1. Schematic illustration of synthesis for undoped vs Mn−doped $CsPbCl_3$ nanocrystals.

II.2 RESULTS AND DISCUSSION

Mn−concentration−dependent Energy transfer in Mn−doped $CsPbCl_3$ nanocrystals

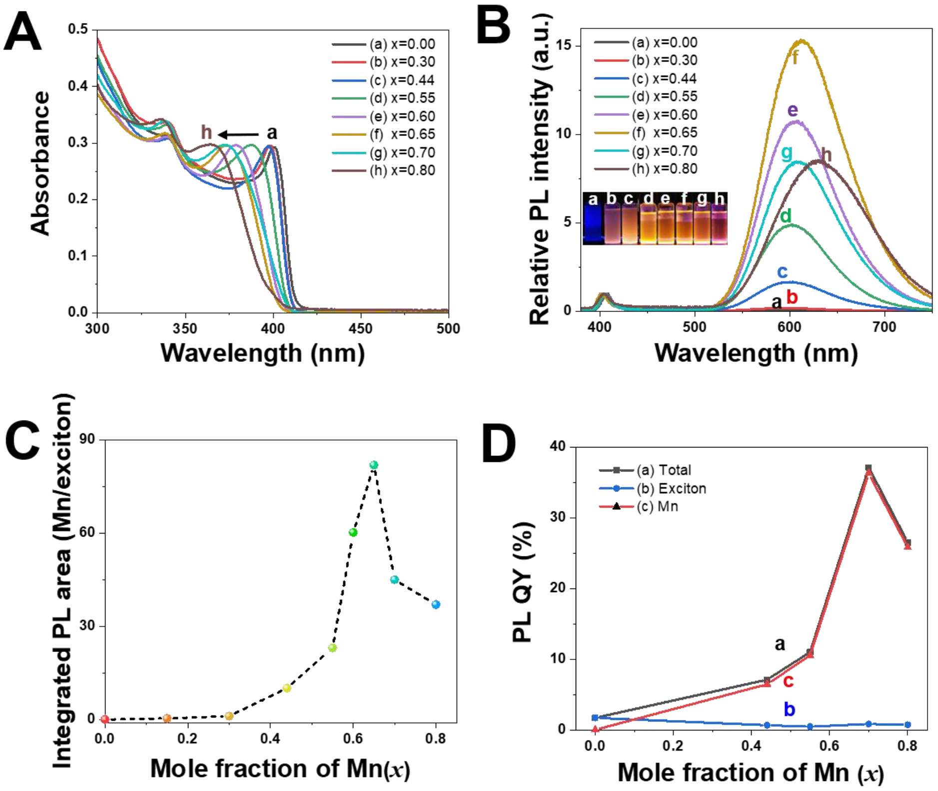

Figure II.2. (A) UV−vis absorption and (B) photoluminescence (PL) emission spectra recorded for undoped and Mn−doped $CsPbCl_3$ with various Mn mole fraction (x) in the precursor solution from x = 0−0.80. (C) Corresponding integrated PL area emission intensity of Mn/exciton by integrating PL emission arising from Mn versus exciton observed in the panel B of PL spectrum. (D) PL quantum yield (QY) measurements for undoped and Mn−doped $CsPbCl_3$ with varying the Mn concentration from x = 0−0.80. Inset to panel B represents the digital photograph taken under the 365 nm UV lamp excitation with different Mn fraction (x).

Mn−doped $CsPbCl_3$ nanocrystals are stabilized by tuning the feeding mole fraction of Mn since the excessive Mn relative to Pb in the precursor solution act as thermodynamic driving forces to overcome the barrier for the doping process, arising from ionic size mismatch between dopant Mn^{2+} ions (97 pm) and host lattice Pb^{2+} ions (133 pm).[87,91] **Figures II.2A** exhibits the UV−vis absorption spectra for the Mn−doped $CsPbCl_3$ nanocrystals as a function of adjusting the Mn mole fraction (x = 0−0.80). The undoped $CsPbCl_3$ nanocrystals (x = 0) as a reference exhibit the excitonic band−edge absorption peak at 400 nm. With increasing the concentration of Mn in the feedstock solution, the band−edge absorption apparently blue−shifted from 400 nm (x = 0) to 370 nm (x = 0.80) owing to alloying with Mn **(Figure II.2A)**. As the dopant concentration of Mn incorporated into $CsPbCl_3$ nanocrystals was well−reported by previous literature precedence, there is a linear correlation of blue−shifting in the excitonic peak as a function of concentration of Mn determined by inductively coupled plasma atomic emission spectroscopy (ICP−AES).[75,87,92] More manganese ions are doped in the nanocrystals, the excitonic peaks of $CsPbCl_3$ nanocrystals with band−edge absorption of 400 nm are shifted to the shorter wavelength due to lattice contraction that is resulted from the alloying of Pb with smaller Mn.[93,94] It is also worth noting that above x = 0.60 a significant blue−shifting of excitonic band−edge absorption is mainly due to band gap change through alloying Pb/Mn. It has been reported that $CsMnCl_3$ has a direct band gap of 4.08 eV and through alloying Mn and Pb the bandgap can be tuned in the range of 4.08−2.19 eV.[95] Increasing the Mn fraction (x) can somewhat improve the final doping concentration of Mn in the host lattices while it is not very effective above the certain limit of dopant concentration ($>x = 0.65$) since PL emission from Mn is saturated (**Figure II.2B**). Both slow cationic kinetic diffusion rate and high activation energy for cation vacancy formation hinder the doping of cation in halide perovskite lattices as compared to relative facile halide ion exchange.[96,97]

Figure II.2B shows the corresponding relative PL emission spectra at different concentration of Mn; **Figure A.1** of Supplementary Figures plots unnormalized PL spectra for further details. For comparison between exciton and Mn emission intensity, excitonic peak at 405 nm in PL spectra is set to 1. The inset of panel 1B shows a digital photograph taken under 365 nm excitation. Important to note that above the certain Mn fraction ($x > 0.30$), distinctive orange emission centered at 600 nm as a result of Mn d−d transition ($^4T_1$ − $^6A_1$) evolved, suggesting the efficient energy transfer from host $CsPbCl_3$ crystals to dopant Mn ions that is also highly Mn−concentration dependent.[46,98] The changes in coloration as a function of Mn concentration reflect that increasing Mn concentration leads to darker orange emission. At the higher Mn dopant concentration (e.g. $x = 0.8$), the Mn emission peak shifted to even longer wavelength of 630 nm whereas the excitonic emission remain in similar emission wavelength of 405 nm regardless of the dopant Mn concentration (**Figure A.1B** of Supplementary Figures). The red-shift of Mn emission can be ascribed to increased Mn-Mn interaction as a result of reducing the interatomic distance of Mn within the host lattices with the same size. These phenomena have been observed in bulk samples before when Mn dopant concentration was very high.[99] The Mn-Mn emission with a lower efficiency is somewhat different from the single Mn emission from the $^4T_1$ to $^6A_1$ transition that has a lower energy transition probability.[100,101]

To understand the power-dependent Mn emission intensity as a result of energy transfer, we have measured the PL for slightly Mn-doped $CsPbCl_3$ with $x = 0.44$ as a representative example. (**Figures A.2A,B** of Supporting Information). Since the emission features from band-edge $CsPbCl_3$ and dopant Mn emission are spectrally well-resolved and deconvoluted, the integrated PL emission of Mn/exciton can be further calculated by integrating the spectral ranges corresponding to exciton (380-450 nm) and Mn emission (500-750 nm). Important to note that the relative PL intensity between Mn and exciton is variable with laser excitation power (1.3-19.6 mW/cm^2) in consistent with earlier reports.[102] Weaker excitation influence with a decreased charge carrier concentration in the unit volume of nanocrystals is more efficient for energy transfer to Mn (**Figures S2C,D** of Supplementary Figures). The increased charge carrier concentration in nanocrystals leads to another unwanted decay pathway mediated through multiple excitons like Auger recombination. This process can suppress relative Mn emission compared to exciton emission.[73] To minimize the excitation power dependence on the ET efficiency, we have used the excitation power at 1.3 mW/cm^2 for further study.

Figure II.2C plots the Mn concentration effect on the integrated PL emission of Mn/exciton. Up to $x = 0.65$, increased feeding Mn fraction resulted in increased dopant concentration within $CsPbCl_3$ nanocrystals as depicted with excitonic peak shift in **Figure A.1B**. The increased dopant concentration of Mn indeed leads to the increased Mn emission while the integrated PL emission intensity decreased above $x > 0.65$. We have further recorded the corresponding PL QY of the undoped and Mn-doped $CsPbCl_3$ nanocrystals with $x = 0$, 0.44, 0.55, 0.70, and 0.80, respectively. **Figure II.2D** depicts the change in PL QY of the total, exciton, and Mn, respectively, *versus* the Mn mole fractions. Each PL QY for exciton and Mn can be further obtained through following the previous report.[102] Overall, the total PL QY was improved upon raising the dopant Mn fraction up to around $x = 0.70$ but decreased above $x = 0.70$. Also, the majority of PL QY arises from the Mn emission rather than exciton emission due to efficient exciton-to-Mn energy transfer with $x > 0.44$. This trend is consistent with the integrated PL emission intensity as depicted in **Figure**

II.2C. It has been reported that the radiative recombination process in dopant Mn was promoted once the forbidden d–d electronic transition was activated through efficient exciton–to–dopant energy transfer.[63,103] However, the total and Mn PL QY declined abruptly above $x > 0.70$ as a result of more enhanced Mn–Mn antiferromagnetic interactions at the elevated Mn concentration as reported earlier.[101] Stronger interaction of interatomic Mn ions with shorter dopant distance can indeed facilitate the nonradiative relaxation of Mn (PL decay study will be discussed later in **Figure II.3**).

To evaluate any change in size and crystal structure during the doping processes, we have taken the transmission electron microscopy (TEM) images by comparing the undoped ($x = 0$) and doped samples ($x = 0.44$ and 0.80). **Figures A.3A–C** (Supplementary Figures) show the low–magnification TEM images corresponding to undoped and Mn–doped $CsPbCl_3$ nanocrystals, respectively. Both undoped and doped $CsPbCl_3$ ($x = 0.44$) samples show similar cubic–shaped nanocrystals with similar sizes of 9 nm albeit with somewhat the electron beam–induced concurrent Pb^0 dot formation marked as a black dot adjacent to the corner of nanocubes.[104,105] At the elevated Mn fraction ($x = 0.80$), the nanocrystal maintained nanocubes with a truncated shape. High–magnification HR–TEM images are further collected for all samples (**Figures A.3D–F of** Supplementary Figures), revealing that the undoped and doped ($x = 0.44$)

$CsPbCl_3$ exhibits similar d−spacing parameters of 0.40 nm along with (101) crystallographic planes that are matched well with orthorhombic $CsPbCl_3$. At the higher fraction of Mn (x = 0.80), the d−spacing value along the same (101) crystallographic planes was determined as 0.395nm, smaller than the value of 0.40 nm with undoped $CsPbCl_3$ nanocrystals, confirming that the more inclusion of Mn leads to the contraction of lattice constant of doped $CsPbCl_3$ nanocrystals (smaller ionic radii of Mn^{2+} as compared to that of Pb^{2+}). It seems like the lattice contraction of Mn with more inclusion of dopants leads to stabilizing of $CsMnCl_3$ nanocrystals.[106]

Roles of Mn concentrations in Energy Transfers

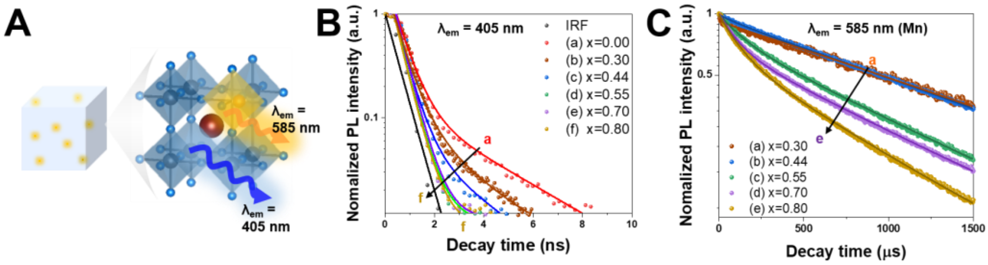

Figure II.3. (A) Schematic illustration of radiative recombination observed in Mn−doped $CsPbCl_3$ nanocrystals. (B,C) PL decay traces and corresponding kinetic fitting using multiexponential fits monitoring the exciton emission at 405 nm (B) and Mn emission at 585 nm (C). Biexponential fits were used for kinetic fitting and detailed fitting parameters are presented in **Table A.1** of Supporting Information.

Figure II.3A depicts the schematic illustration of dual emission from the Mn^{2+}−doped $CsPbCl_3$ perovskite nanocrystals owing exciton−to−dopant energy transfer. We have further recorded the time−correlated single−photon counting (TCSPC) of Mn^{2+} doped $CsPbCl_3$ nanocrystals to understand the complex charge carrier and energy transfer dynamics between exciton and Mn states including radiative, non−radiative, and energy transfer processes. **Figures II.3B,C** plot the PL decay traces for exciton observed at 405 nm (Figure II.B) and for Mn emission at 585 nm (Figure II.3C), respectively, with various Mn mole fractions of $x = 0-0.80$. The PL decay curves can be fitted using a bi−exponential function with a faster component (τ_1) and a slower component (τ_2) and their corresponding amplitudes (A_1 and A_2) as shown in equation (3).

$$I = I_0 + A_1 exp\left(-\frac{t}{\tau_1}\right) + A_2 exp\left(-\frac{t}{\tau_2}\right) \qquad (3)$$

Each component calculated from the PL decay kinetic fittings is listed in **Table A.1**. The average lifetime (τ_{avg}) can be further calculated using the following equation (4).

$$\tau_{avg} = \frac{A_1\tau_1^2 + A_2\tau_2^2}{A_1\tau_1 + A_2\tau_2} \qquad (4)$$

With increasing x from 0−0.80, the average lifetime of exciton was decreased from 1.34 ns (x = 0) to 0.44 ns (x =0.80) **(Figure II.3B** and **Table A.1)**, which is consistent with previously reported experimental results.[75,107] The difference in average lifetime between undoped and Mn−doped samples mainly arises from the additional decay path of enerty transfer. Specifically, the portion of faster component (A_1) corresponding to radiative decay of exciton becomes smaller from 0.93 (x = 0) to 0.79 (x = 0.80) as a function of increasing x, reflecting that Mn^{2+} doping creates a new energy transfer channel from exciton to Mn^{2+} ions that is distinct from the existing two channels (radiative and non-radiative recombinations). On the other hand, the portion of slower component (A_2) increases from 0.07 (x = 0.00) to 0.21 (x = 0.80). Upon doping, the formation of additional energy acceptor states opens up an energy transfer pathway for exciton occurring in the nanosecond timescale (~ns), leading to reduced radiative decay and enhanced non-radiative decay simultaneously.[108,109]

It has been reported that the dynamic energy transfer (ET) and corresponding ET efficiency are strongly influenced by electronic coupling between energy donor and acceptor that is also dependent on the spatial location and concentration of dopant across the host lattice of nanocrystals.[92,110,111] When the excitons of the nanocrystals serve as energy donor and the energy state of Mn act as energy acceptor, the relative radial distance and number of acceptor per unit volumes of the nanocrystals affects the exciton dynamics and energy transfer kinetics.[63,92]

The energy transfer efficiency (Φ_{ET}) is, thus, computed using the average PL lifetime (τ_{avg}) of exciton either in the presence or absence of Mn dopants using the equation (5)

$$\Phi_{ET} = 1 - \frac{\tau_{avg} Exciton\ with\ Mn}{\tau_{avg} Exciton} \qquad (5)$$

where $\tau_{avg}^{\mathrm{Exciton\ with\ Mn}}$ and $\tau_{avg}^{\mathrm{Exciton}}$ are the exciton lifetime of Mn^{2+}−doped and undoped $CsPbCl_3$ nanocrystals, respectively (**Table A.1 and A.2** of Supporting Information).

As seen in PL QY and PL emission spectra with Mn fraction from $x = 0$−0.80 (**Figure II.2**), the energy transfer efficiency generally increased with the increased dopant Mn concentration up to $x = 0.65$. As the number of energy acceptors of atomic Mn doped in host lattices increased, energy transfer to Mn is more promoted owing to the increased number of acceptors relative to the fixed number of energy donors corresponding to the excitons in the $CsPbCl_3$ nanocrystal.[92,112] If there is any change in the average lifetime of nanocrystals upon doping, the changes in lifetime are mainly ascribed to the energy transfer process from exciton to dopant. The value of Φ_{ET} increased from 36.3% (for $x = 0.44$) to 66.7% (for $x = 0.80$), suggesting that increased dopant concentrations allow for efficient ET (**Table A.2** of Supporting Information).

Using the Φ_{ET} determined from equation 5, the energy transfer rate constant (k_{ET}) can be further computed as per the following equation (6)

$$\Phi_{\mathrm{ET}} = \mathrm{k_{ET}}/(\ \mathrm{k_r}^{\mathrm{Exciton}} + \mathrm{k_{nr}}^{\mathrm{Exciton}} + \mathrm{k_{ET}}) \qquad (6)$$

where $k_r^{Exciton}$ and $k_{nr}^{Exciton}$ represent the radiative and nonradiative recombination rate constant of excitons, respectively, which were already determined from the PL QY (equation 1).

The corresponding energy transfer rate constant (k_{ET}) increases from 0.67 ns^{-1} (for x = 0.44) to 4.52 ns^{-1} (for x = 0.80), indicating that increased dopant concentration induces faster energy transfer rate, which is in good agreement with the accelerated decay processes as a result of exciton−to−Mn energy transfer.

This trend can be also observed when monitoring the decay of Mn emission at 585 nm with different Mn^{2+} concentrations (**Figure II.3C)**. Considering that the energy transfer timescale occurs in the nanosecond timescale (~ns) that is much shorter than the Mn emission with the millisecond timescale (~ms), the Mn emission decay corresponds to d−d transition of Mn^{2+} state that is activated by exciton−to−dopant energy transfer process.[111] The average lifetime of Mn emission decreases from 1574 μs to 758 μs as dopant concentration increases from x = 0.44−0.80 (**Table A.1** of Supplementary Figures). At x = 0.44, Mn PL decay curves seem like a monoexponential decay with a majority of longer component (A_2: 96%). However, at the elevated Mn concentration, the portion of the shorter component of (A_1) was amplified which is closely related to promoted non−radiative recombination. Again, the increased Mn−Mn interatomic antiferromagnetic interaction ascribed to ferromagnetic characters of Mn^{2+} ions leads to favorable nonradiative recombination owing to the shorter distance between Mn components. As a result of increased interatomic interactions, Mn emission intensity decreases (**Figure II.2B**), leading to faster Mn emission decay at the heavily-doped Mn regime (**Figure II.3C**). These Mn-concentration dependent behaviors have been also observed previously in Mn^{2+} doped II-VI nanocrystals and dopant-activated phosphors.[113]

Role of Halide Composition in Energy Transfers

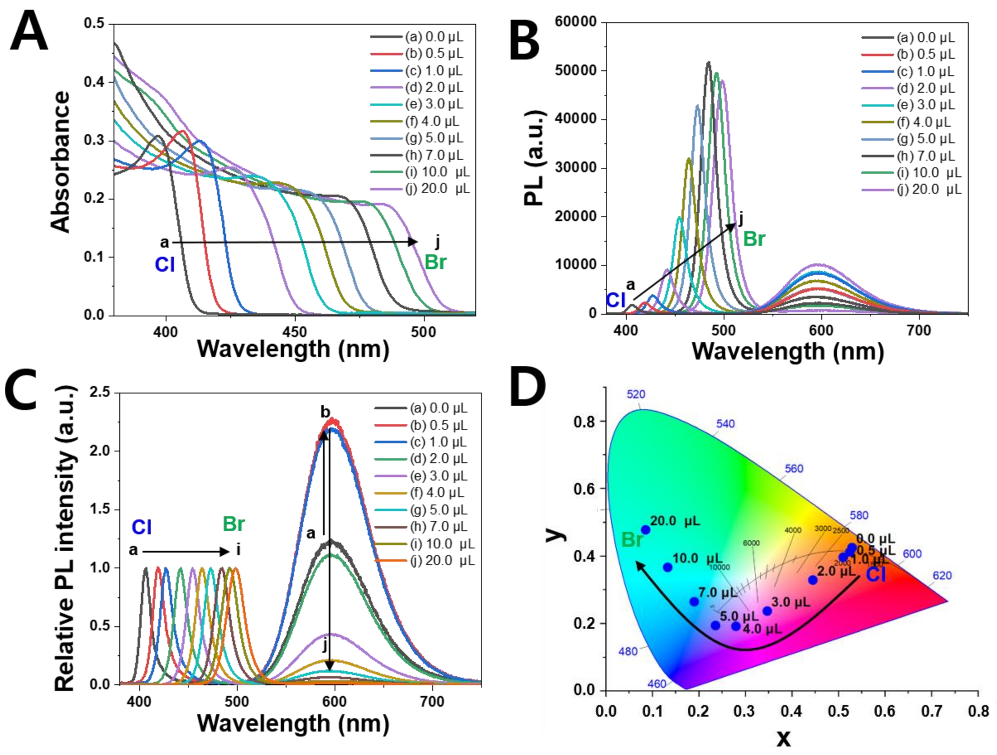

Figure II.4. (A) UV–vis absorption and (B) PL emission changes occurred during halide exchange reaction with accumulative addition of $PbBr_2$ solution (0.05 M) from 0–10 μL into 66 nM of Mn–doped $CsPbCl_3$ with x =0.44. (C) Relative PL spectra by normalizing the excitonic peak as set to be 1 shown in panel B. (D) Corresponding CIE color diagram changes when adding $PbBr_2$ solution as shown in panel B

To understand the halide composition effects on the ET efficiency, we have precisely modulated the halide ion composition (Cl/Br) through a bromide exchange reaction for Mn–doped $CsPbCl_3$ to form mixed halides of Cl/Br. First, we have performed a bromide ion exchange reaction using undoped $CsPbCl_3$ as illustrated in **Figures A.4A–C** of Supplementary Figures. As more Br sources were added to the fixed concentration of

$CsPbCl_3$ nanocrystals, the band−edge absorption gradually shifted from 398 nm to 490 nm, and corresponding PL emission was also changed from 405 nm to 503 nm. The bandgap (eV) and exact composition of mixed halide $CsPb(Cl_{1-y}Br_y)_3$ was further determined using the Tauc plots and Vegard laws as illustrated in **Figures A.5A,B.**[114,115] Based on the observation from TEM images and similar nanocrystal size for doped and undoped nanocrystals, the red−shifting in band−edge absorption and change in bandgap are mainly resulted from halide ion exchange from Cl to Br by adding Br sources. Halide exchanges were repeated for other Mn−doped $CsPbCl_3$ nanocrystals with the identical method.

Figure II.4A shows the modulation of band−edge absorption as a function of varying the halide composition (Cl → Br) for Mn−doped nanocrystals with $x = 0.44$. UV−vis absorption, PL emission, and relative PL spectra for other Mn fractions (for $x = 0.30, 0.55, 0.60, 0.70$, and 0.80) are also plotted in Supporting Information of **Figures A.6−10**. As more Br ions are provided to replace the Cl, the band−edge absorption continuously red−shifted from 396 nm to 487 nm for $x = 0.44$. Corresponding PL emission spectra were also taken as depicted in **Figure II.4B**. To compare the relative PL intensity arising from exciton and Mn emission, the PL emission spectra were adjusted by normalizing the spectrum to exciton peak as set to be 1. The exciton PL peak shifted from 406−500 nm after treating 20 μL of $PbBr_2$ (0.05 M). The Mn emission peak initially rises but falls after the addition of 2 μL of PbBr solution corresponding to Mn−doped

$CsPb(Cl_{1-y}Br_y)_3$ with y = 0.13 at the excitonic peak of 406 nm (corresponding bandgap of 2.95 eV) determined from Tauc plots (**Figure A.5**). The relative PL emission spectra more apparently depict such trends that Mn emission initially increased up to the addition of Br 0.5 μL and decreased afterward (**Figure II.4C**). These phenomena can be explained by the decreased exciton decay rate with Br substitution. After a small portion of Cl was substituted with Br around 0.2 min, the integrated PL intensity showed the strongest Mn/exciton emission

This observation is also monitored in-situ after the initial dumping of 20 μL of $PbBr_2$ (0.05 M) into the same concentration of Mn-doped $CsPbCl_3$ with x = 0.44 over the period of time for 10 min (**Figures A.11A-C**). Reaction time-dependent changes in the absorption and PL illustrates that a reduced exciton binding energy with Br substitution (exciton binding energy of $CsPbBr_3$ with 40-60 meV vs $CsPbCl_3$ with 75 meV)[116,117] leads to longer-lived exciton as compared to that of Cl, allowing for facilitating the competent exciton-to-Mn energy transfer (**Figures A.11A-C**).[52,112] As calculated above, the energy transfer occurs in sub-nanosecond timescale (~ns) which is much slower than II-VI semiconductor nanocrystals in sub-picosecond timescale (~ps).[75,76] Weaker coupling interaction between exciton and Mn observed in the ionic halide perovskite nanocrystal as compared to more covalent nanocrystals brings about 2-3 orders of magnitude longer energy transfer time (~ns).[77] However, at the elevated Br composition, the Mn/exciton PL emission intensity declined rapidly. This can be understood with competent forward and backward energy transfer between exciton and Mn states. Upon reducing bandgap from Cl to Br, Mn-to-exciton backward energy transfer is more facilitated in Br-rich perovskites since the energy barrier corresponding to the energy difference between band-edge and Mn energy states is reduced upon Br exchanges.[87] As the lifetime of Mn emission is in the millisecond timescale (~ms) due to spin- and parity-forbidden transition, the reduced bandgap upon exchanging with Br ions can effectively allow for back-transfer to excitonic state, which leads to the reduction of Mn emission. The backward Mn-to-exciton energy transfer is a thermally-activated process with an energy barrier corresponding to the energy separation between the Mn state ($^4T_1$) and the conduction band-edge of exciton.[87,110,118]

Based on dual emissive features of Mn-doped mixed halide nanocrystals with $x = 0.44$, white light emission can be generated by precisely adjusting the exciton (Cl/Br) and Mn emission ratios. The corresponding color coordination and temperature in CIE diagram can be tracked and plotted in **Figure II.4D**. Upon substituting to Br-rich perovskites, the corresponding color point (x, y) shifted from (0.54, 0.42) for 0 μL (Cl perovskites) to (0.09, 0.48) for 20 μL (Br perovskites). At the addition of 3-4 μL of Br sources with exciton peak around 460 nm, reddish- or bluish-white emission features corresponding to (0.37, 0.25)–(0.30, 0.20) can be realized depending upon the dual emissive features of exciton vs Mn

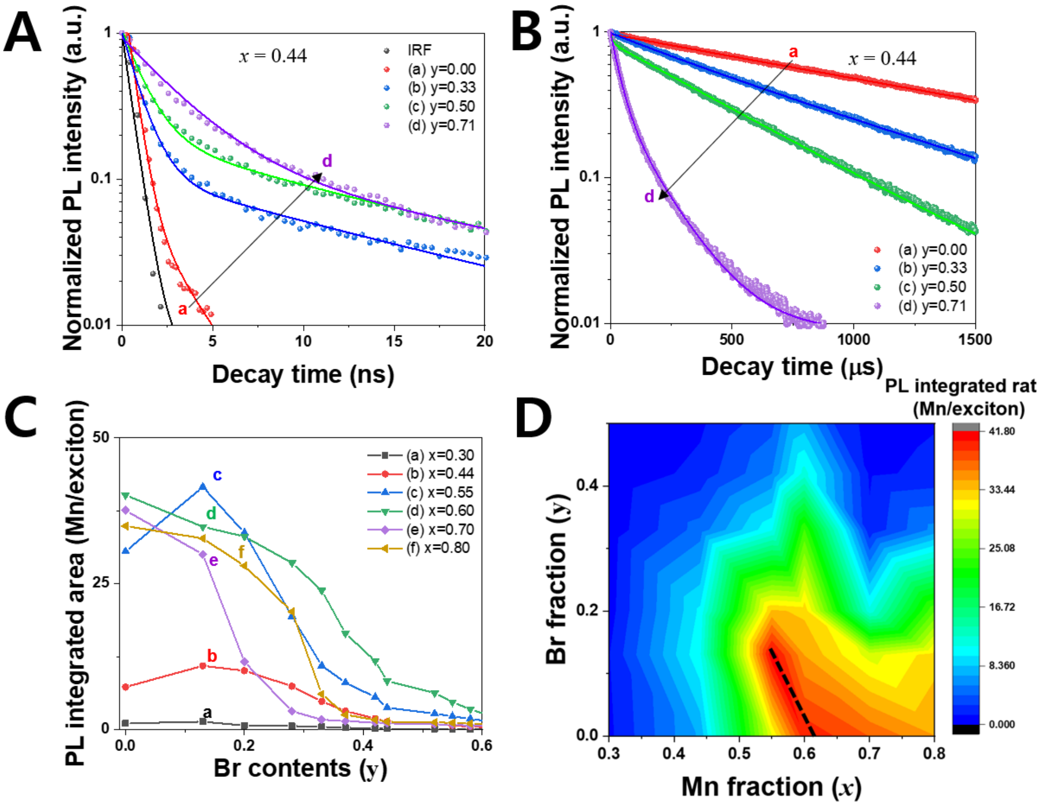

Figure II.5. (A,B) PL decay traces and corresponding kinetic fitting using biexponential fits monitoring the exciton emission (A) at 405 (a), 450 (b), 470 (c), and 490 nm (d), respectively, and Mn emission at 585 nm (B) using Mn−doped $CsPb(Cl_{1-y}Br_y)_3$ with $x = 0.44$. (C) Integrated PL emission intensity of Mn/exciton with different Mn fraction of $x = 0-0.80$ along with different Br of $y = 0-0.6$ when adding lead bromide (0.05 M) solution into Mn−doped $CsPbCl_3$ nanocrystals. (D) 2D Mapping for Mn/exciton PL emission intensity as a function of varying the dopant Mn fraction (x) and Br (y) in Mn−doped $CsPb(Cl_{1-y}Br_y)_3$ nanocrystals. Biexponential fits were used for kinetic fitting and detailed fitting parameters are presented in **Table S3** of Supporting Information.

emissions.

Figures II.5A,B show the PL decay traces for exciton (Figure II.5A) and Mn emission (Figure II.5B) with various Br contents with x = 0.44, respectively. Kinetic fitting parameters are summarized in **Table A.3** of Supplementary Figures. As a control experiment, we have also performed halide ion exchange using the undoped (x = 0.00) samples and analyzed the PL decay dynamics (**Figure A.12** and **Table A.4** of Supplementary Figures). As Br fraction increases in the host nanocrystals, the average lifetime of band-edge exciton increased from 0.85 ns (y = 0) to 9.54 ns (y = 0.71). A similar trend was observed in a previous study.[112,119] As reported from the previous study that the density of trap states within the bandgap and exciton binding energy decreases significantly in narrower bandgap perovskite, the non-radiative recombination through trap states is, thus, significantly suppressed in the mixed $CsPb(Cl_{1-y}Br_y)_3$ nanocrystal with higher Br content, extending exciton lifetime.[120] On the contrary, the Mn emission lifetime apparently decreased from 1574 μs (y = 0) to 114 μs (y = 0.71) even with the same Mn concentration (x = 0.44). Interestingly, the shorter lifetime component (A_1) becomes one of the major decay paths seen in Mn emission with increasing Br content from y = 0 – 0.70. The significantly reduced lifetime seen in Mn emission reflects the faster relaxation process occurring within Mn^{2+} state including the increased portion of backward energy transfer (BET) from Mn to exciton occurring in a faster timescale (~ns) than a forbidden transition in Mn states (~ms). This is also evidenced when calculating the energy transfer efficiency (Φ_{ET}) for these halide-exchanged samples. The value of Φ_{ET} gradually decreased from 0.53 (for $y = 0$) to 0.06 (for $y = 0.33$), to 0.04 (for $y = 0.50$), and to 0.01 (for $y = 0.71$). This strongly suggests that the forward energy transfer (or backward energy transfer) become negligible (more dominant) upon reducing the bandgap of the mixed $CsPb(Cl_{1-y}Br_y)_3$ nanocrystal by increasing the portion of bromide.

Figure II.5C summarizes the integrated PL emission ratio Mn/exciton as a proxy to illustrate the resulting competition between the two recombination processes (exciton and Mn) including the forward (exciton-to-Mn) and backward (Mn-to-exciton) energy transfers as a function of varying different x (Mn content) and y (Br content) simultaneously. With a lightly-doped Mn regime with smaller $x = 0.44$–0.55, the strongest Mn/exciton emission was observed with a little Br substituted in the $CsPbCl_3$ nanocrystals (around $y = 0.13$–0.20). In stark contrast, at the elevated Mn-doped regime, the strongest Mn/exciton emission was detected at the $CsPbCl_3$ nanocrystals with $y = 0$, the highest Cl concentration. These suggest that the number of energy acceptors (Mn) can alter the excited state dynamics between exciton and Mn. **Figures II.5D and A.13** (Supplementary Figures) further depict the 2D color mapping for the integrated PL emission of Mn/exciton; the hotter spot indicates the efficient exciton-to-Mn energy transfer regimes whereas the colder spot designates less efficient energy transfer. As discussed above, the overall results arising from the complex concentration- and halide composition−dependent exciton−to−Mn energy transfer (and reverse) can be vividly captured. First off, when Br content (*y*) is larger than y = 0.4 in Mn−doped $CsPb(Cl_{1-y}Br_y)_3$ nanocrystals, Mn emission intensities significantly quenched regardless of the dopant concentration as a result of more favorable backward energy transfer with a reduced bandgap (**Figure A.11**). Albeit with the retarded exciton recombination and longer−lived exciton upon Br exchange relative to Cl−based perovskites that can promote the forward energy transfer to Mn, thermally−activated backward Mn−to−exciton transfer upon reducing the bandgap become also dominant excited state decay pathway (~ns), making exciton recombination more efficient, consistent with the observation of halide−composition−dependent PL decays shown in **Figure II.5B**.[87,110,118] When Br content is smaller than $y = 0.4$, there are two distinctive Mn concentration (lightly− vs heavily−doped) regimes (**Figure II.5D**). In the first lightly−doped regime with Mn mole fraction lower < $x = 0.55$, the mixed halide composition Cl/Br with $y = 0.13$ shows the strongest Mn emission due to efficient energy transfer. In this concentration regime, the halide composition plays a major role in dictating the energy transfer efficiency. Change in exciton binding energy, exciton recombination kinetics, and electronic overlap between band structure of exciton and Mn states as a function of halide composition directly governs the competing forward and backward energy transfer kinetics (**Figure II.6A**). Apparently, the hottest spot illustrating the strongest Mn emission in 2D color maps shifted to lower Br content (y) upon further increasing Mn fraction (x). There is a clear linear correlation between the Mn content and Br content as denoted with a dotted line in **Figure II.5D**. Clearly different behavior as a function of varying Mn concentration (or acceptor density and distribution across the host lattices) and simultaneously control over the halide host compositions indeed determines competing exciton recombination, forward exciton–to–dopant energy transfer, and backward dopant–to–exciton energy transfer rates.

In the second heavily–doped Mn regimes ($x > 0.65$), the forward exciton–to–Mn energy transfer efficiently occurs at the higher Cl composition due

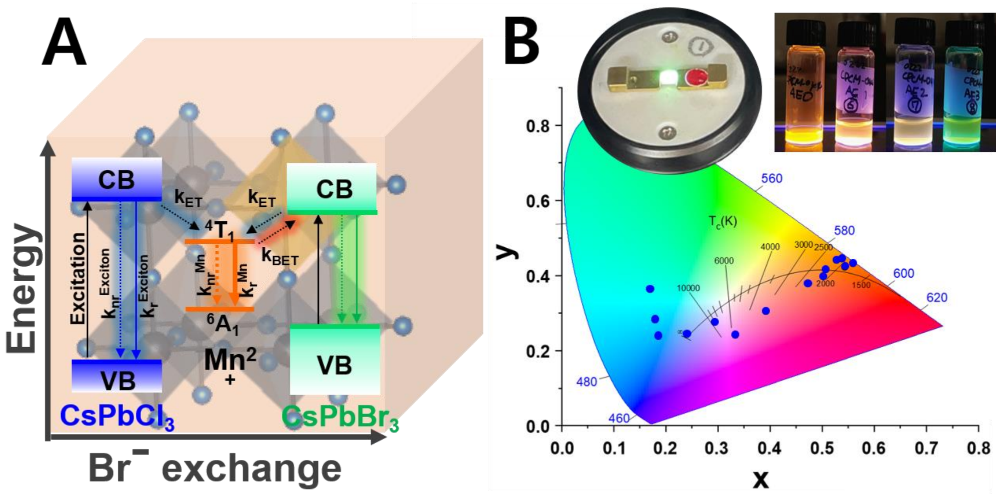

Figure II.6. (A) Schematic illustration demarcating the competing excited state dynamics and energy transfer shown in Mn–doped mixed halide perovskite nanocrystals. (B) Application toward white light emitting diodes and corresponding CIE color diagram. Insets to panel B show the proto–type UV–LEDs modules and solution emission under 365 nm excitation.

to the increased acceptor density of Mn dopants albeit with the shorter exciton lifetime in the Cl-based perovskites. While the ET is not very efficient in the lightly-doped regime for $CsPbCl_3$ (100% Cl) as compared to slightly mixed halides due to a large energy barrier, increased concentration of Mn in the heavily-doped regimes can indeed promote the efficient ET at the pure Cl-based perovskites. Strikingly differently, in this heavily-doped concentration regimes, the backward energy transfer upon exchanging with Br becomes a major decay pathway. Therefore, Cl-based perovskite with a high energy barrier shows the strongest Mn/exciton emission since the backward Mn-to-exciton transfer is more activated upon Br substitution. The decrease in exciton binding energy, retarded exciton recombination rate, and increased electronic overlap upon Br substitution can allow for efficient backward transfer (~ns) that rapidly quench the Mn emission (~ms) at the elevated Br contents in the heavily-doped regime. In other words, the backward energy transfer becomes dominant excited state decay pathway of Mn emission even though the competing forward energy transfer happens rapidly from exciton to Mn states at the heavily-doped Mn concentration with a noticeably decreased Mn lifetime.

Figure II.6B illustrates the CIE diagram and proto-type of UV-LEDs activated by depositing the Mn-doped $CsPb(Cl_{1-y}Br_y)_3$ nanocrystals. By changing either Mn concentrations or halide compositions, we can finely tune the color points and temperatures. The insets to **Figure II.6B** show digital photographs taken under the operation of a UV−LEDs chip and Mn−doped $CsPb(Cl_{1-y}Br_y)_3$ with x = 0.44−0.70 and different halide composition of y = 0−0.70, respectively. The color points of Mn−doped mixed halide perovskites suggest that the color temperatures can be controlled by modulating the dual emissive features of exciton and Mn. However, intrinsic dual emission does not allow for perfect white light emission with (0.33, 0.33) due to a lack of combination of three different colors properly mixing blue, green, and red within this emitter at the same time.

CHAPTER III

Machine Learning–Directed Predictive Models: Deciphering Complex Energy Transfer in Mn–Doped CsPb$(Cl_{1-y}Br_y)_3$ Perovskite Nanocrystals[*]

III.1 EXPERIMENTAL

Materials.

Cesium carbonate (Cs_2CO_3, 99.9%, Alfa Aesar), lead chloride ($PbCl_2$, 99%, Alfa Aesar), lead bromide ($PbBr_2$, 98.5%, Alfa Aesar), manganese (II) chloride tetrahydrate ($MnCl_2 \cdot 4H_2O$, 98+%, Sigma–Aldrich), oleic acid (OA, 90%, Sigma–Aldrich), oleylamine (OLAm, 70%, Sigma–Aldrich), 1–octadecene (1–ODE, 90%, Sigma–Aldrich), hexanes (Samchun Chemicals, 96%). After receiving from the manufacturer, all chemicals were used without purification.

Preparation of Cesium oleate (Cs–OA).

Cs–OA is prepared according to previously reported literature.[87,121] In a 20 mL vial, Cs_2CO_3 (0.4 g), OA (1.25 mL), and ODE (15 mL) were mixed

---

[*] [*] Reprinted with permission from "Machine Learning–Directed Predictive Models: Deciphering Complex Energy Transfer in Mn–Doped CsPb$(Cl_{1-y}Br_y)_3$ Perovskite Nanocrystals" by H.Choe, H.Jin, S.J.Lee, J.Cho., *Chem. Mater.* 2023, 35, 14, 5401–5411. ©2023 American Chemical Society. All rights reserved.

and heated at 150 ℃ for 1 hr until the solids in vial are fully dissolved. Before usage of the Cs−OA, it had been gently heated again to make transparent solution.

Synthesis of undoped and Mn−doped $CsPbCl_3$ nanocrystals.

For information, the synthetic procedure of undoped and Mn−doped $CsPbCl_3$ nanocrystals are identical except the initial metal precursors used. First, for the synthesis of undoped $CsPbCl_3$ nanocrystals, a $PbCl_2$ (0.2 mmol; 0.0556g), OA (0.5 mL), OLAm (0.5 mL), and ODE (5 mL) were loaded a 50 mL 3−neck round bottom flask and heated to 105 ℃ under vigorous stirring. The mixture solution was degassed at the temperature for 30 minutes and further heated to 185 ℃ under the flow of N_2. Cs−OA (0.45 mL) solution was swiftly injected into the flask when the temperature reached at 185 ℃. After 10 seconds, the reaction flask was taken and put in the ice bath. For the synthesis of Mn−doped $CsPbCl_3$ with different Mn concentrations, initial Mn fraction (x = Mn/(Mn+Pb)) in the feed stock of precursor solutions was varied in the range of x = 0−0.8. Actually, doped Mn concentration in host lattices was determined using inductively coupled plasma atomic emission spectroscopy (ICP−AES). For example, synthesizing a sample with x = 0.6, a $PbCl_2$ (0.08 mmol; 0.022 g), $MnCl_2 \cdot 4H_2O$ (0.12 mmol; 0.024 g), OA (0.5 mL), OLAm (0.5 mL) and ODE (5 mL) were used. Other remaining steps for the synthesis of doped samples are the same with those of undoped $CsPbCl_3$ nanocrystals. After synthesis, the reaction solution was spun down for 10 min at 4000 rpm to purify the nanocrystals. The supernatant was discarded, precipitates were taken, and re-dispersed in 3 mL of hexanes for further characterizations.

Anion exchange reaction for Mn-doped $CsPb(Cl_{1-y}Br_y)_3$.

A 0.05 M $PbBr_2$ stock solution for the halide exchange reaction was prepared in a 20 mL vial by dissolving 0.4 mmol of $PbBr_2$ (0.4 mmol; 0.147 g) in a mixture of OA (0.5 mL), OLAm (0.5 mL) and ODE (7 mL). The mixtures were heated at 150 ℃ until they become transparent in solution. The anion exchange reaction was performed using Mn-doped $CsPbCl_3$ nanocrystals by adding 0.05M $PbBr_2$ stock solution at room temperature under vigorous stirring. When the reaction had been completed, the nanocrystals were separated by centrifugation at 4000 rpm and the precipitates were taken and redispersed in hexane for further characterizations. The halide composition of Cl/Br in the $CsPb(Cl_{1-y}Br_y)_3$ nanocrystals was determined using Vegard’s law (See section 2.6).

In-situ Anion exchange reaction for 2D PL.

For in-situ 2D PL measurement throughout bromide exchange reaction, Mn-doped $CsPbCl_3$ nanocrystals dispersed in 3 mL of hexanes were used with absorption 0.1 (22nM). A 5 μL of 0.05M $PbBr_2$ stock solution was added and in-situ anion exchange reaction were performed. During the anion exchange, in-situ 2D PL measurements were recorded at a scan speed of 20000 nm/min with 8 seconds time interval for 1500 seconds.

Determine the Br composition (*y*) in $CsPb(Cl_{1-y}Br_y)_3$.

To determine the Br composition (*y*) in mixed $CsPb(Cl_{1-y}Br_y)_3$ nanocrystals, Tauc plot and Vegard's law were used.[122–124] Undoped $CsPbCl_3$ nanocrystals is initially used as a reference for determination of content of bromide in the mixed halide upon bromide exchange reaction. The calculated bandgap and Br composition (*y*) of mixed halide perovskites upon the addition volumetric amount of $PbBr_2$ (0.05 M) stock solution are shown in **Figure A.16**.

Characterizations.

The transmission electron microscopy (TEM) images were taken using a JEM-2100F (HR) (JEOL LTD) at an operating voltage at 200kV. ICP-AES measurements were conducted using Shimadzu ICPE-9000 inductively coupled plasma-atomic emission spectrometer. For sample preparation for ICP-AES, Mn-doped nanocrystals were digested using a 1% HNO_3 solution. Mn concentration in nanocrystals was determined by the atomic ratio of Mn versus total divalent metals of (Pb+Mn). UV-vis absorption spectra were taken with a Cary 60 UV-vis spectrophotometer system (Agilent Technology) in the spectral range of 300-800nm with a scan speed of 4800 nm/min. The Photoluminescence (PL) emission spectra were recorded using an Ocean Optics Spectrometer with 365 nm excitation diode along with an Ocean HDX (FM-OH100) photodetector. Time-resolved PL decays were collected using a time correlated single photon counting (TCSPC) system made by Horiba Jobin Yvon. A nanoLED laser with 375 nm was used as excitation source whereas IBH DataStation Hub was used for detecting timing. Instrument response function (or IRF) was measured with hexanes itself for solution measurements. PL decay traces were fitted using bi-exponential functions (equation 1) to calculate the average carrier lifetime (equation 2).

$$I = I_0 + A_1 exp\left(-\frac{t}{\tau_1}\right) + A_2 exp\left(-\frac{t}{\tau_2}\right) \quad (1)$$

$$\tau_{avg} = \frac{A_1\tau_1^2 + A_2\tau_2^2}{A_1\tau_1 + A_2\tau_2} \quad (2)$$

Machine learning modeling.

Scikit learn software package was used in Python for construction of regression models. Six different regression models were built and examined. The initial dataset of 86 samples was used for contructing machine learning models. Before beginning the modeling, initial dataset was split into train data (80 %) and test data (20 %). Grid search with cross−validations was carried out to find optimal hyperparameters of each model until the subset of the hyperparameters of the algorithm is exhaustively examined to figure out the best hyperparameters. In particular, five−fold cross−validations were employed wherein train dataset was divided into five different number of groups that were used for learning and validating each fold set repeatedly up to five times. Such k−fold cross validation (dataset is split into k number of folds) can prevent the overfitting, allowing for optimization through tuning hyperparameters based on evaluation results of dataset. A regression that is commonly used in statistical modeling to estimate the correlation between independent variable (input) and dependent variable (output) was performed. A linear regression and non−linear regression were examined: linear algorithm and five different non−linear machine learning algorithms including support vector (SVR), k−nearest neighbor (KNN), random forest (RFR), gradient boosting (GBR), and extra tree regressors (ETR). The optimal hyperparameters for each predictive model were found through grid search with five−fold cross validations. To create the best performing models, grid search enables to finds the the best values through exhaustively testing all possible combinations of hyperparameters values for given values. The models are validated using the same train dataset when performing grid search. Once the optimal hyperparameters are obtained, the performance of machine learning models is evaluated using the following evaluation metircs: mean absolute error (MAE), mean squared error (MSE), and the root-mean-square error (RMSE), standard deviation (SD), and the coefficient of determination (R^2) for linear fits. Root-mean-square error (RMSE) was used as an representative evaluation criterion.

Kinetic Modeling of Carrier Dynamics.

We quantify the populations of exciton state in perovskite nanocrystals and Mn-ion states in terms of average per-nanocrystal occupancies.[125,126] The evolution of n_X (band-edge exciton) and n_Mn (excited Mn state) in the low pump level regime can be described by the following rate equations (3-4)[102]

$$\frac{dn_\mathrm{X}}{dt} = -k_\mathrm{X}n_\mathrm{X} - k_\mathrm{ET}n_\mathrm{X} + k_\mathrm{BT}n_\mathrm{Mn} \qquad (3)$$

$$\frac{dn_\mathrm{Mn}}{dt} = -k_\mathrm{Mn}n_\mathrm{Mn} - k_\mathrm{BT}n_\mathrm{Mn} + k_\mathrm{ET}n_\mathrm{X} \qquad (4)$$

where k_X, k_Mn, k_ET and k_BT are the decay rate constant of exciton, Mn, forward energy transfer from exciton to Mn, and backward energy transfer from Mn to exciton, respectively. By solving these equations, each population can be derived using biexponential decay with the two different rate constants k_s (slow) and k_f (fast) expressed as follows (equations 5−6).

$$n_x = A_s \exp(-k_s t) + A_f \exp(-k_f t) \qquad (5)$$

$$n_{Mn} = B_s \exp(-k_s t) + B_f \exp(-k_f t) \qquad (6)$$

where the two rate constants can be further expressed as follows.

$$k_{(f(+),s(-))} = \frac{1}{2}\left(k_x + k_{ET} + k_{Mn} + k_{BT} \pm \sqrt{(k_x + k_{ET} - k_{Mn} - k_{BT})^2 + 4k_{ET}k_{BT}}\right) \qquad (7)$$

Based on the assumption $k_{Mn} << k_x$ and $k_{BT} << k_{ET}$, the decay rate for the slow and the fast channels including k_s and k_f can be simply approximated using the following equations (8−9).

$$k_s \approx k_{Mn} + \left(1 - \frac{1}{1+k_x/k_{ET}}\right) k_{BT} \qquad (8)$$

$$k_f \approx k_x + k_{ET} \qquad (9)$$

Based on the initial condition at $t = 0$, $A_s + A_f = n_0$ (n_0 is the total number of originally injected excitations at the zero time) and $B_s + B_f = 0$, we can obtain $A_s \sim 0$ and $A_f \sim n_0$. By substituting equations (5−6) with equations (3−4), finally, the population of each state (n_x and n_{Mn}) as a function of time can be calculated (*vide infra*).

III.2 RESULTS AND DISCUSSION

Exploring Multidimensional Design Spaces in Mn–doped Perovskites.

Mn–doped $CsPbCl_3$ perovskites nanocrystals with varying Mn dopant concentration are stabilized through adjusting initial divalent metal stoichiometric ratio (mole fraction of Mn) in the precursor solution. Halide composition ($Cl_{1-y}Br_y$) of the Mn–doped perovskite nanocrystals is further tuned through the post–synthetic halide ion exchange reactions. Upon altering the nominal initial mole fraction of Mn (x) and bromide concentration (y) in halide composition enable to control the Mn concentration at the different host lattice of perovskite $CsPb(Cl_{1-y}Br_y)_3$ nanocrystals.

Figure III.1A represents the absorption spectra changes upon increasing the Mn fraction (x) from the range of x = 0–0.8. The increased Mn concentration (actually doped dopant concentration) bring about the blue–shifting of the band–edge absorption peak of $CsPbCl_3$ nanocrystals from 400–370 nm. Inductively coupled plasma atomic emission spectroscopy (ICP–AES) directly confirmed actually doped Mn concentration in the host crystals (**Figure A.14**). The concentration of Mn gradually increased from 0.0 atom% (for x = 0) to 27.5 atom% (for x = 0.80). Transmission

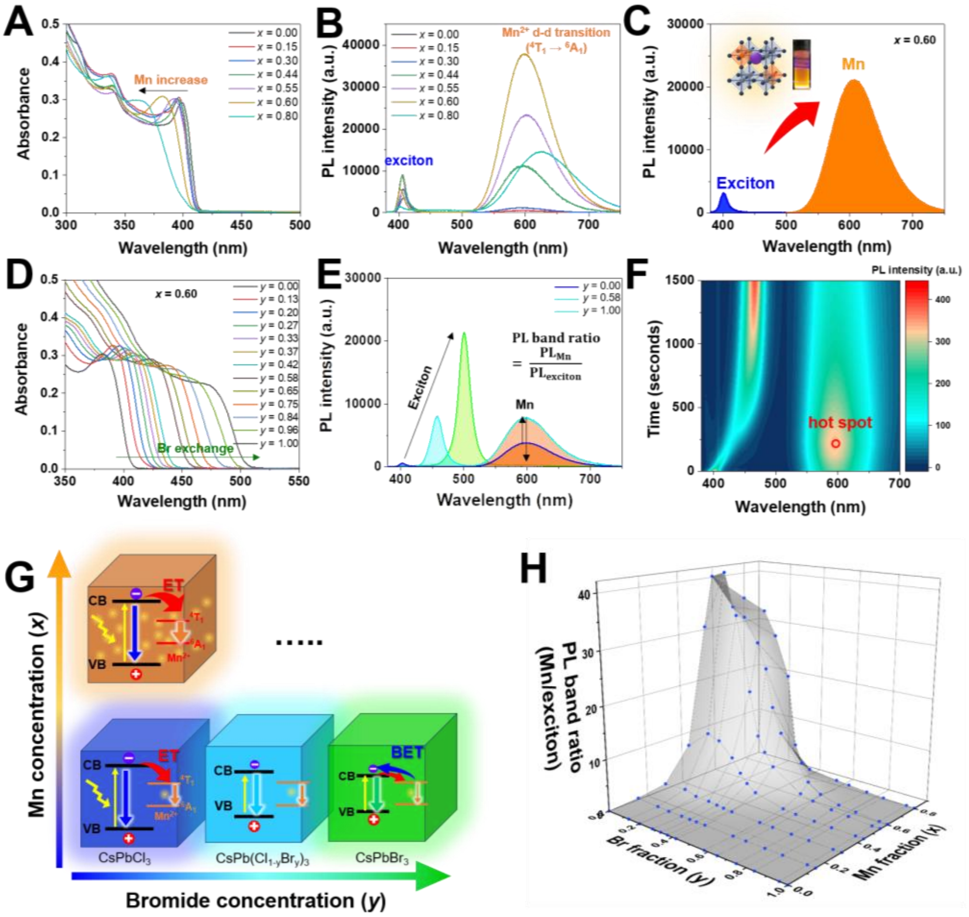

Figure III.1. (A) Absorption and (B) corresponding photoluminescence (PL) emission spectra recorded for Mn-doped $CsPbCl_3$ with different Mn fraction (x) ranging from $x = 0-0.80$. (C) a representative PL emission spectrum demarcating the energy transfer from exciton-to-Mn. (D) Absorption spectra for Mn-doped $CsPb(Cl_{1-y}Br_y)_3$ with $x = 0.60$. (E) PL emission spectra during anion exchanges to illustrate the energy transfer. (F) In-situ monitoring the 2D PL emission during the anion exchange using Mn-doped $CsPb(Cl_{1-y}Br_y)_3$ with $x = 0.60$ for 1500 sec. The wavelength of 365 nm was selected to record the PL emission spectra. Time-dependent 2D color PL mapping was recorded with step size of 8 sec. (G) Schematic illustration to tune reaction parameters including Mn concentration and bromide concentration in the Mn-doped mixed halide perovskites. (H) An initial scattering dataset derived from PL emission band ratio of Mn/exciton (z) for Mn-doped $CsPb(Cl_{1-y}Br_y)_3$ nanocrystals as a function of nominal Mn fraction (x) and bromide concentration (y)

Mn of $x = 0$, 0.44, and 0.80, indicating that there was no significant change in sizes throughout doping (**Figures A.15**). Corresponding photoluminescent (PL) emission spectra are further recorded as shown in **Figure III.1B**. Two different emission features (or dual emissions) can be seen, ascribed to exciton (~400 nm) and Mn emission peaks (~595 nm), respectively. With increasing x up to 0.60, the Mn emission intensity is enhanced owing to efficient exciton−to−dopant energy transfer (**Figure III.1C**). Interestingly, the sample with $x = 0.80$ exhibits more red−shifted Mn emission feature at ~620 nm due mainly to dimerized $Mn^{2+}-Mn^{2+}$ species with a reduced electronic transition energy, consistent with earlier report.[127] The relative PL emission band ratio of Mn/exciton, shown in following equation 3, is readily obtained by integrating exciton and Mn PL emission bands, respectively, that are further primarily utilized as a main probe to evaluate the degree of energy transfer (**Figure III.1C**).[63,102]

$$\text{PL band ratio} = \text{PL}_{\text{band (Mn)}}/\text{PL}_{\text{band (exciton)}}$$

Figures III.1D,E illustrates the changes of absorption and emission features for Mn−doped $CsPbCl_3$ with $x = 0.60$ upon replacing chloride with bromide throughout halide ion exchange. As a reference, we performed bromide exchange reaction using the undoped $CsPbCl_3$ nanocrystals as well (**Figure A.16A**). Converted Tauc plot analysis allows for determining the bandgap of the mixed halide perovskites (**Figures A.16B,C**). Corresponding bromide concentration (y) can be further deduced from the determined bandgap and summarized in **Figure A.16D,** following Vegard's law. The band-edge absorption corresponding to transition from valence band to conduction band shifted to longer wavelength from 400–480 nm, indicative of reduced bandgap for Br-substituted perovskites (**Figure III.1D**). The band-edge emission from $CsPb(Cl_{1-y}Br_y)_3$ appeared in the range of 400–510 nm whereas the Mn emission is constantly observed at ~600 nm (owing to fixed d-d transition of Mn^{2+}).[87,98,107,128] The absolute Mn emission intensity rises upon initial exchanges to bromide ($y = 0.58$) but decreased upon further exchanging fully to 100% of bromide at the end of reaction ($y = 1.00$) (**Figure III.1E**). To understand such complex energy transfer (forward versus backward) dictated by Mn concentration and halide compositions (and bandgap), we have mapped out 2D PL emission throughout in-situ bromide ion exchange by dumping 5 μL of 0.05M $PbBr_2$ into Mn-doped $CsPbCl_3$ nanocrystals with $x = 0.60$ (**Figure III.1F**). The 2D PL color map vividly captures the energy transfer process as a function of controlling the bandgap of the perovskites, directly affecting the electronic coupling between exciton and Mn energy states.

Here, we aim to explore multivariate design spaces in Mn-doped $CsPb(Cl_{1-y}Br_y)_3$ halide perovskite nanocrystals with varying reaction parameters of Mn fraction (x) (or actually doped Mn concentration determined by ICP-AES) and halide compositions in particular with bromide concentration (y) in mixed halide perovskites and understand how these two reaction parameters affect the degree as well as kinetics of exciton-to-dopant energy transfer (**Figure III.1G**). [129–131] These two different complex reaction parameters influence the competitive forward and backward energy transfer and resulting exciton and Mn relaxation dynamics.[63,92,121]

Figure III.1H shows the scattered initial dataset as a function of nominal Mn fraction (x) and bromide concentration (y) in Mn-doped CsPb($Cl_{1-y}Br_y$)$_3$ nanocrystals obtained through bromide exchange reaction as depicted in **Figures A.17A–E** and **Figure III.1D** (absorption) and **Figures A.18A–F** and **Figure A.19A–F** (emission). The PL emission band ratio of Mn/exciton (z) are mainly utilized as a proxy to evaluate the energy transfer efficiency. In each reaction space (x, y), the PL emission band ratios (z) are summarized in **Table A.5**. With aid of machine learning models, we can decipher the competing energy transfer (completive forward exciton-to-Mn and backward Mn-to-exciton) given this uncompleted dataset (86 samples).

Machine Learning–Directed Predictive Models

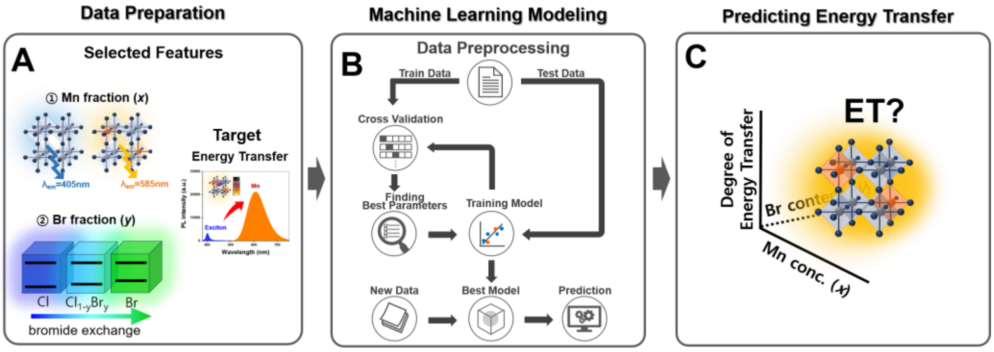

Figure III.2. (A–C) Schematic illustration of building the machine learning guided predictive models to understand and predict the energy transfer occurring Mn–doped $CsPb(Cl_{1-y}Br_y)_3$ nanocrystals: (A) data preparation with feature selection and target, (B) machine learning guided modeling procedure, and (C) understanding and predicting energy transfer occurring in Mn–doped $CsPb(Cl_{1-y}Br_y)_3$ nanocrystals

Figures III.2A–C demonstrate the detailed procedure for machine learning–guided models to predict the complex energy transfer seen in mixed Mn–doped $CsPb(Cl_{1-y}Br_y)_3$ nanocrystals. The initial dataset was input for creating the machine learning–guided models. The first important step in machine learning directed modeling is to select the appropriate features that can effectively describe the data (**Figure III.2A**).[132,133] Herein, we choose the Mn fraction (x) and bromide concentration (y) as selected feature descriptors, affecting the target energy transfer.[134]

Detailed procedure for machine learning–guided modeling has been demonstrated in **Figure III.2B**. **Figures A.20A–F** show the changes in RMSE using six different machine learning algorithm models over five–

fold iterations. Notably, most of algorithms except supporter vector machine (SVR) demonstrate there are not considerable changes in RMSE, meaning that there is no considerable overfitting after fifth iterations. Such machine learning−guided models were further trained again using the train dataset with the best hyperparameters found in grid search. This eventually evaluates the test dataset to find the best model. The best hyperparameters searched for each model are found in **Table A.6.**

After finding the best hyperparameters of each model, five−fold cross−validation with six different algorithms were performed using the train dataset of 68 samples (80% of total dataset of 86 samples). Corresponding cross−validation results including RMSE along with SD as representative performances are plotted in **Figure A.21**. In terms of evaluating the performance of each model, LR shows highest RMSE±SD value of 9.4±1.8 than others. This indicates that the ability of LR based model is not capable of giving an accurate prediction of the PL band ratio value (degree of energy transfer). In stark contrast, KNN and ETR models show much improved performances with decreased RMSE±SD of 4.0±2.3 and 3.6±2.1, suggesting that these two models allow for giving more accurate prediction abilities. Next, we have further repeated such five−fold cross−validations using much less dataset of 22 samples (80% of total dataset of 28 samples) by filtering out the PL band ratio smaller than 10 whether there is any significant improvement in performances of each model; this is because LR significantly overfitted below PL band ratio = 10 (**Figure III.3A**). **Figure**

A.21B summarizes the performances of RMSE±SD using the data with PL band ratio >10 that there are no significant differences between each model. This is probably due to limited number of given samples for training (22 samples) that is less than 50, thus not allowing for capturing and modeling the nonlinear trend.

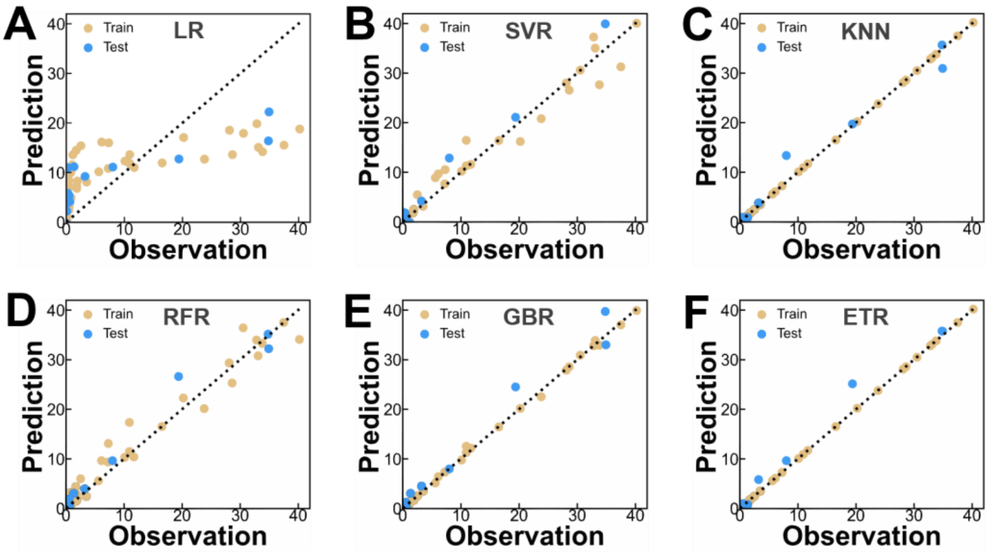

Figure III.3. (A–F) Regression results for comparison of predicted and observed energy transfer in Mn–doped $CsPb(Cl_{1-y}Br_y)_3$ nanocrystals using different regression models: (A) linear regression (R^2 = 0.556), (B) support vector regression (R^2 = 0.927), (C) k–nearest neighbor regression (R^2 = 0.980), (D) random forest regression (R^2 = 0.970), (E) gradient boosting regression (R^2 = 0.974), and (F) extra tree regression (R^2 = 0.980).

Figures III.3A–F depicts parity plots using six different regressor for comparing the observed value of PL band ratio value against predicted one. All performance metrics of trained and tested ML models are summarized in **Table A.7**. The LR model is not effective in its ability to predict the output target with the largest RMSE of 7.5 and lowest R^2 value of 0.556, suggesting that such model severely overestimates the output below PL band ratio = 10 whereas underestimates the output above PL band ratio = 10 (**Figure III.3A**). Classification−based two different algorithm such as SVR and KNN were examined next wherein data are treated based upon distances−based classification.[135,136] Such algorithms show significantly improved performances, more accurately predicting target with reduced RMSE of 3.0 (SVR) and 1.6 (KNN), respectively (**Figures III.3B,C**). Also, the R^2 value was determined to be 0.927 (for SVR) and 0.980 (for KNN), demonstrating that these models allow for predicting the energy transfer without significant under− or over−estimation in the entire range of PL band ratio = 0−40. Decision tree−based algorithms were further tested using RFR, GBR, and ETR algorithms, respectively. All three tree−based models performed better than LR with decreased RMSE in the range of 1.6−1.9. In particular, random forest regressions are known as one of the most accurate learning algorithms since a large number of trees give more robust model. Such algorithm use ensemble learning method for regression in which multiple machine learning algorithms are applied for prediction. However, in our study, RFR regressions exhibit the lower R^2 of 0.970 than other two since this model have inherent weakness owing to less interpretability and longer computing times (**Figure III.3D**).[137] **Figures III.3E,F** shows the results from GBR and ETR with improved R^2 value of 0.974 and 0.980, respectively, along with reasonable RMSE of 1.8 and 1.6, respectively. Both models work very well to give an accurate prediction of the output target. In particular, this is probably because GBR aggregate the result along the way of process, improving and overcoming the deficiency and error of the previously built trees during the process of creating decision tree additively (each decision tree is made at a time),.[138] Importantly, ETR works similar to RFR but the former builds multiple decision tress with random split nodes without bootstrap replicas.[139] Overall, KNN and ETR models outperform other tested regression models with highest R^2 values of 0.980. Even training and testing dataset with PL band ratio >10, KNN gives very accurate prediction of R^2 value with 0.984 (**Figure A.22A−F** and **Table A.8**), outperforming the others. To further examine the robustness of the built machine learning models, we additionally input five different new data (**Figure S10**) into each model to examine the performances. Corresponding performance metrics are summarized in **Table A.23**. As expected from the performance metrics, KNN most effectively predict the energy transfer with lowest RMSE of 0.4±0.2 and highest R^2 values of 0.978, indicating that KNN models are the most robust predictive model that is less disturbed by externally added new dataset.

Figures III.4A−F illustrates 3D contour color mapping created by using the machine learning predictive models to understand the energy transfer in Mn−doped $CsPb(Cl_{1-y}Br_y)_3$ nanocrystals. As learned from performance metrics, LR model is not capable of efficiently predicting the energy

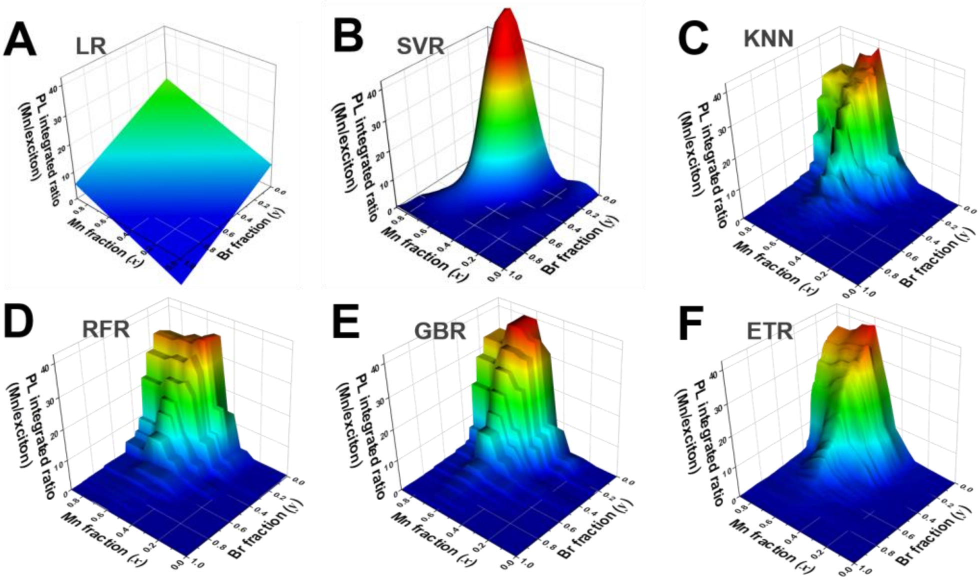

Figure 4. 3D contour color mapping for predicting the energy transfer seen in Mn−doped $CsPb(Cl_{1-y}Br_y)_3$ nanocrystals using six different regression models: (A) linear regression, (B) supporter vector regression, (C) k−nearest neighbor regression, (D) random forest regression, (E) gradient boosting regression, and (F) extra tree regression.

transfer as a function of variable x and y that are severely susceptible to under− and over−estimation. Other models can somewhat predict and find the correlations how Mn and bromide concentrations indeed influence the energy transfer. The reddish spots in the 3D plots depict the most efficient energy transfer zone while the bluish spots indicate that there is not efficient energy transfer from exciton to Mn. In general, all models except LR predicts that Mn−doped $CsPb(Cl_{1-y}Br_y)_3$ nanocrystals with around x = 0.6 and slightly bromide−exchanged y = 0.1 show the highest Mn emission with PL band ratio = 40 or larger. However, as seen from the cross−validation performance of each model such as SVR, RFR, and GBR, these models were not very effective for prediction of target output due to higher cross-validation RMSE larger than 5. In particular, SVR was more prone to overestimating at the hottest spot whereas RFR and GBR does not effectively capture the landscape of energy transfer with abrupt PL band ratio changes across data points. Both KNN and ETR models can rather describe accurate 3D landscape of the energy transfer more effectively.

Deciphering Competing Carrier Dynamics.

To further decipher the competing forward and backward energy transfer between exciton and dopant, we have recorded the time-correlated single photon counting (TCSPC) using two different Mn-doped samples (x = 0.30 and 0.60) upon bromide exchange. As determined from the ICP analysis (**Figure A.14**), Mn concentration was determined as around 5 atom% for x = 0.30 (referred to as lightly-doped regime) and 12.5 atom% for x = 0.60 (referred to as heavily-doped regime), respectively. Before recording PL lifetime of doped samples, we have collected PL lifetime for undoped samples as a control that is plotted in **Figures A.24.** The PL decay kinetic traces for undoped $CsPb(Cl_{1-y}Br_y)_3$ nanocrystals were further fitted using biexponential fits involving the faster component (t_1) and slower component (t_2) as described in equations 1-2. The details of the kinetic fittings can be found in **Table A.10**. The calculated average carrier lifetime was determined to be 0.58 ns (y = 0) for pure Cl but increased up to 6.24 ns (y = 1) for pure Br perovskites. The increased carrier lifetime reflects that charge carrier recombination is apparently suppressed with bromide substitution, consistent with earlier reports.[121] Upon increasing bromide concentration, the decreased exciton binding energy dependent on halide composition along with reduced bandgap for $CsPbBr_3$ nanocrystals favors the long-lived exciton in the excited states.[112,119]

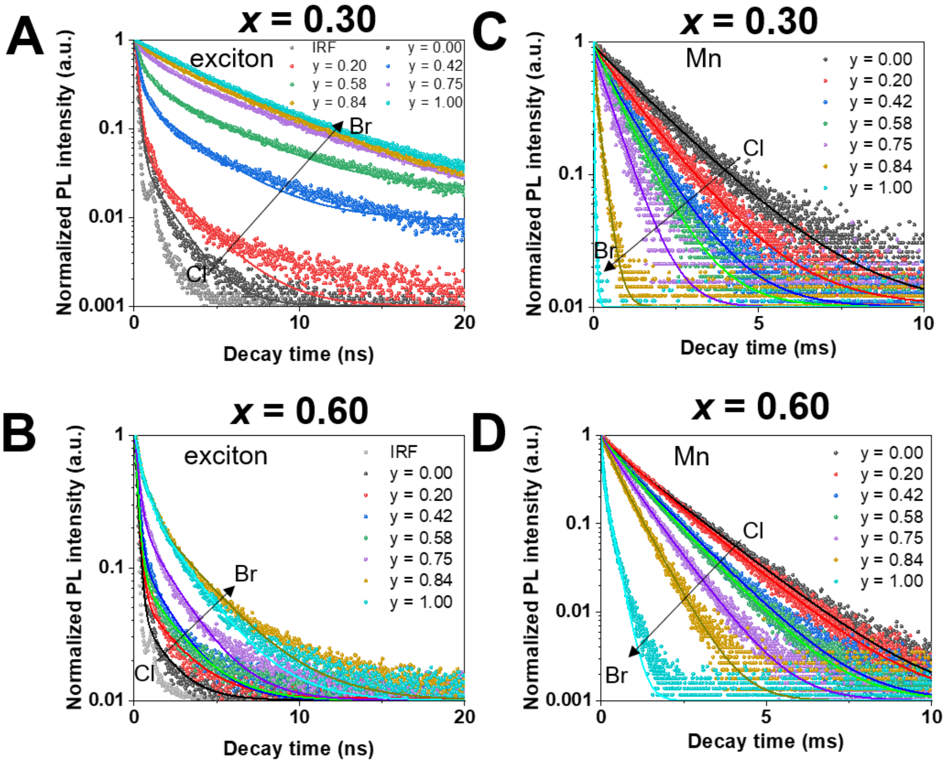

Figure III.5. (A−D) PL decay traces and kinetic fittings by monitoring the exciton peak (A,B) and Mn emission peak (C,D) using Mn−doped $CsPb(Cl_{1-y}Br_y)_3$ nanocrystals with x = 0.30 (A,C) and 0.60 (B,D), respectively. Kinetic fitting curves are fitted using biexponential functions and fitting parameter details are summarized in **Tables A.11, A.12** of Supporting Information.

Figures III.5A–D plot the PL decay traces and kinetic fittings by monitoring the excitonic peak (405–510 nm for 7A,B) versus Mn emission peak (~ 595 nm for 7C,D) for $x = 0.30$ and $x = 0.60$, respectively, during the course of bromide exchange reactions. We first closely investigated the change in exciton recombination dynamics by comparing the average carrier lifetime for $x = 0$, $x = 0.30$, and 0.60 samples (**Figures III.5A,B** and **Figure A.24**). The average carrier lifetime decreased upon increasing Mn content (x) from 0.58 ns ($x = 0$) to 0.51 ns ($x = 0.30$), and to 0.50 ns ($x = 0.60$). The introduction of dopant into the host lattices indeed created a new decay pathway, that is an energy transfer from exciton to dopant, occurring in the same nanosecond timescale, thus accelerating the exciton PL decay.[108,109] It is also important to note that increased dopant concentration across the host lattices at the certain Cl/Br composition promote the faster energy transfer. In consideration of energy transfer taking place as a result of donor (exciton) and acceptor (Mn) interaction, the forward energy transfer and competing back energy transfer rate occurring between exciton and Mn are heavily dependent on concentration and spatial distribution of Mn dopants and bandgap affecting the degree of electronic coupling between energy donor and acceptors as illustrated in **Figure III.1G.** The increased number of Mn atoms in a single nanocrystal results in increased Mn population near center of nanocrystals, which improves wavefunction overlap between exciton and Mn, giving rising to stronger electronic coupling and resulting faster energy transfer.[37,92,108] The energy transfer efficiency that can be expressed in terms of difference of exciton lifetime before and after addition of Mn reveals the degree or efficiency of energy transfer.

Interestingly, as more Br is replaced with Cl in the mixed halide perovskite $CsPb(Cl_{1-y}Br_y)_3$, the average carrier lifetime increased from 0.51 to 5.31 (for x =0.30) and from 0.50 to 1.75 ns (for x = 0.60). These mirror the observation from the results of x = 0 (**Figure A.24**). The average exciton lifetimes in the heavily-doped regime are much shorter than those in the lightly-doped regime mainly due to the more promoted forward energy transfer that is strongly dependent on Mn concentration.

More importantly, sensitization of the forbidden d-d transition and Mn recombination is not only affected by forward exciton-to-dopant energy transfer but also by competing backward dopant-to-exciton energy transfer, which leads to the thermal equilibrium between two excited states of exciton and Mn.[37,87,118] By analyzing the Mn decays as displayed in **Figures III.5C,D** at the different Mn concentration regimes (lightly-versus heavily-doped regime), we can find that Mn decays rapidly upon increasing Br concentration for both x = 0.30 (lightly-doped regime) and x = 0.60 (heavily-doped regime). The Mn lifetime decreased from 1757 to 31 μs (for x = 0.30) and from 1445 to 219 μs (for x = 0.60), respectively. Apparently, it seems like that Mn decay significantly gets more accelerated in the lightly-doped regime than in the heavily-doped regime even though replacing with the same bromide at the certain mixed Br/Cl composition (at the same y value). Consdiering the acceleated Mn decay arises from the backward energy transfer from Mn to exciton that is mainly depednent on energy gap difference between exciton and Mn energy state, in the lighly-doped regimes, smaller energy difference between two states (due to not significant impact as a result of Mn-alloying induced increased bandgap) indeed prmotes the rapid backward energy transfer.

To take account how the forward and backward energy transfers impact on the PL decay dyanmics and how two synthetic parameters (x and y) can govern the competing energy transfer kinetics, we created a kinetic model describing dynamics of the band edge excitons and the excited Mn state. We quantified the populations of exciton state in perovskite nanocrystals (n_{x}) and Mn ion states (n_{Mn}) in terms of average per-nanocrystal occupancies (see the detail in Experimental section). In our study, there is at least six orders of magnitude difference between the decay rate constant of the exciton (k_{x}) and Mn (k_{Mn}), and it turns out that the forward (k_{ET}) and backward energy transfer rate constant (k_{BT}) have three orders of magnitude difference. Based on the assumptions $k_{\mathrm{Mn}} << k_{\mathrm{x}}$[46,140] and $k_{\mathrm{BT}} << k_{\mathrm{ET}}$[87] and the initial conditions at $t = 0$, we can derive the population of each state as a function of time (equations 10-11)

$$n_{\mathrm{x}} = n_0 \exp(-(k_{\mathrm{x}} + k_{\mathrm{ET}})t) \qquad (10)$$

$$n_{Mn} = n_0/(1 + k_x/k_{ET})(\exp(-(k_{Mn} + (1 - 1/(1+k_x/k_{ET})k_{BT})t) - \exp(-(k_x + k_{ET})t)) \qquad (11)$$

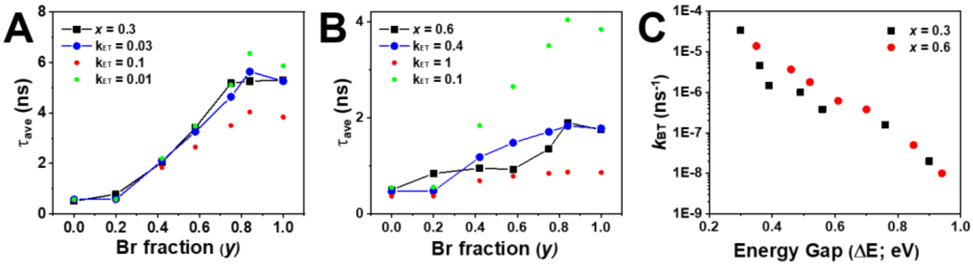

Figure III.6. (A,B) Comparison of the experimental and calculated average lifetime (τ_{ave}) of the exciton emissions from Mn−doped CsPb$(Cl_{1-y}Br_y)_3$ nanocrystals with (A) x = 0.3 and (B) x = 0.6 upon changing Br concentration from y = 0−1.00. (C) backward energy transfer rate (k_{BT}) of Mn−doped CsPb$(Cl_{1-y}Br_y)_3$ nanocrystals with x = 0.3 (black) and x = 0.6 (red) as a function of the energy gap (ΔE) between the exciton state and Mn−ion state

Here k_x and k_{Mn} can be experimentally determined from the excitonic PL decay of undoped CsPb$(Cl_{1-y}Br_y)_3$ nanocrystals upon changing Br concentration from y = 0−1.00 (**Figure A.24** and **Table A.10**) and from the Mn emission decay of Mn−doped CsPbCl$_3$ nanocrystals where the decay dynamics of Mn emission becomes close to the intrinsic k_{Mn} (**Tables A.11 and A.12**), respectively.

We used these equations to fit the PL decay data as plotted in **Figure III.6A**. First, we applied n_x to estimate k_{ET} from the exciton PL decay dynamics as shown in Figure 7A,B. For x = 0.3 sample with different Br concentration (y), we can obtain the best fitting as compared to the experimental data when applying k_{ET} = 0.03 ns^{-1} (**Figure III.6A**). Upper and lower boundary condition of k_{ET} = 0.1 and 0.01 ns^{-1}, respectively, are also plotted for comparison. However, the boundary condition with smaller or larger k_{ET} does not fully account for the experimental results. We have repeated for x = 0.6 sample upon varying the y values. It turns out that the best fit to the experimental result as shown in Figure 7B with k_{ET} = 0.4 ns^{-1} (**Figure III.6B**). This manifests that the energy transfer gets accelerated in the heavily-doped regime with one order of magnitude as compared to the slightly-doped regime with increased rate constant of k_{ET} = 0.4 ns^{-1} (x = 0.60) versus k_{ET} = 0.03 ns^{-1} (x = 0.30). The forward energy transfer rate constant (k_{ET}) is mainly dictated by Mn concentration (x) rather than Br concentration-dependent bandgap. The increased number of Mn atoms in a single nanocrystal results in increased Mn population (energy acceptor) near center of nanocrystals (energy donor), which in turn enhance wavefunction overlapping of exciton with Mn, giving rising to stronger electronic coupling with faster energy transfer to Mn. The bandgap controlled with bromide composition (y) does not play a crucial role in controlling k_{ET} in our experimental conditions.

Second, we applied n_{Mn} to estimate k_{BT} from the Mn emission decay dynamics as demonstrated in **Figure III.6C**. It turns out that k_{BT} strongly depends on the energy difference gap between exciton and Mn state (ΔE). For both x = 0.3 and x = 0.6, the rate constant of k_{BT} falls in the similar values as a function of modulating ΔE, dictating negligible effect of x values on k_{BT}.(**Figure III.6C**). Here ΔE can be experimentally determined from the Tauc plots of **Figure A.16** for x = 0.3 and **Figure III.1D** for x = 0.6, respectively, as a function of Br concentration (y). The blue shift in ΔE for x = 0.6 compared to that for x = 0.3 in every y value is due to the Mn incorporation induced alloying as we observed in **Figure III.1A**. Therefore, y is the main parameter which controls the ΔE and its corresponding k_{BT}. When decreasing ΔE (or substituting with bromide), it accelerated the backward energy transfer from Mn to exciton in halide perovskite due to reduced energy barrier. The backward energy transfer is an up-hill process that needs to overcome the energy barrier. The energy gain for the up-hill energy transfer comes from the thermal energy. Thermal population of the excited Mn state is getting more feasible, accelerating the backward transfer as decreasing ΔE at our measurement condition of room temperature (kT = 26 meV).

Elucidating Energy Transfer Mechanism.

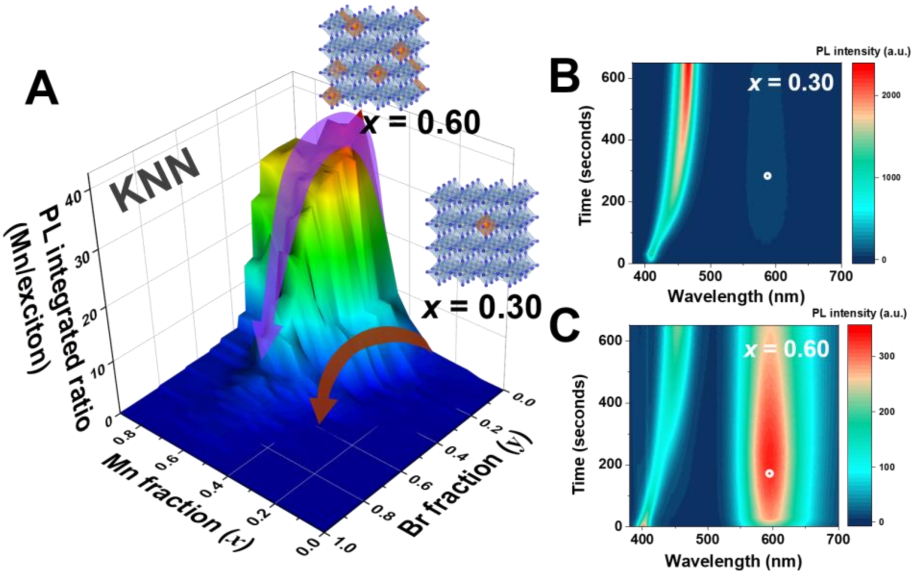

Figure III.7. (A) 3D visualization of the degree of energy transfer predicted by k-nearest neighbor regressor (kNN) model at the different Mn concentration and halide composition. (B,C) In-situ monitoring of the 2D PL emission during the anion exchange using Mn-doped $CsPb(Cl_{1-y}Br_y)_3$ with $x = 0.30$ (B) and $x = 0.60$ (C) for the first 650 sec.

In the lightly doped regime ($x = 0.30$), as seen from the PL emission intensity of Mn (**Figure III.7A** predicted using KNN), the maximum Mn intensity or hottest spot is found with slightly mixed halide perovskites with Br (at $y = 0.13$ or $CsPb(Cl_{0.87}Br_{0.13})_3$. This is directly ascribed to the increased energy transfer efficiency in the mixed halide perovskites owing to increased exciton lifetime and reduced bandgap upon bromide substitution. However, upon further increasing Br concentration, the competing process of backward Mn-to-exciton energy transfer is switched back on as a result of more reduced bandgap, activating the backward transfer from Mn to exciton owing to more decreased energy barrier.[37,87,118] In the PL decay lifetime measurement, the Mn lifetime rapidly declined upon bromide substitution above $y = 0.20$, facilitating the Mn emission quenching as a result of more pronounced backward transfer. In this lightly-doped regime, excitonic emission is majorly observed throughout halide exchange, resulting in lower PL band ratio < 5 as can be seen in the color map of **Figure III.7A**.

However, in the heavily-doped regime ($x = 0.60$), different behavior can be seen that the highest PL band ratio of Mn emission already reached the maximum intensity at $y = 0$ and maintained to some extent up to higher bromide concentration of $y = 0.40-0.50$. Despite the shorter exciton lifetime of pure Cl-based perovskites, the faster energy transfer rate to Mn occurs with increased order of magnitude energy transferee kinetic rate constant. Upon increasing the portion of Br concentration, a similar phenomenon is observed that reduced bandgap facilitates the backward energy transfer, reflecting the decreased Mn emission (**Figure III.7A**). However, considering the competing kinetics between forward exciton-to-Mn ($10^{-1}-10^{-2}$ ns^{-1}) and backward Mn-to-exciton energy transfer ($10^{-5}-10^{-8}$ ns^{-1}) as well as the number of energy donor and acceptor, the increased number of Mn atoms at $x = 0.60$, initially serving as energy acceptor (for forward energy transfer) yet later serving as energy donor (for backward transfer), overall favor carrier accumulation in Mn state at the equilibrium of the excited state. From our kinetic analysis, it was revealed that the improved electronic coupling as a result of increased Mn concentration within nanocrystals leads to the even faster forward energy transfer from 0.03 ns^{-1} (x = 0.3) to 0.4 ns^{-1} (x = 0.6) at given bromide concentration (y) while the backward energy transfer rate constants (k_{BT}) are not much affected by Mn concentration (x). In this scenario, the increased number of Mn populations serve as an efficient energy acceptor and increased difference between forward and backward energy transfer kinetic rate constants, result in accumulation of carrier in Mn state. The change in Mn lifetime recorded at the same bromide concentration (at the fixed y) throughout Br exchange further contrasts the Mn concentration effect.

By monitoring the in-situ PL for both evolution of exciton (400 nm) and Mn (~600 nm) emission peaks for x = 0.30 and x = 0.60 during the course of Br exchange reaction for the first 650 sec, we can double-confirm that two different Mn regimes behave differently that the Mn concentration affects the forward energy transfer kinetics and resulting Mn emission due to carrier accumulation in the Mn states (**Figures III.7B,C and Figures A.25A-D**). Increased Mn concentration for x =0.60, significant Mn emission is observed even with the 100% Cl-based perovskites and Mn emission is maintained throughout entire Br substitution even owing to the reduced energy different gap acting as an energy barrier for backward energy transfer (up to 650 sec). **(Figures A.25 and A.26).**

IV. Dissertation Summary and Conclusions

To summarize, we have explored the excited−state behavior in Mn−doped CsPb$(Cl_{1-y}Br_y)_3$ based on adjusting in Mn concentration and halide composition. These behaviors were examined by fine−tuning the Mn concentration through its feedstock fraction and changing the Br content through Br exchange. In addition, our research has enabled us to predict the exciton−to−energy transfer degree (z) using machine learning. The energy transfer efficiency is determined by the excited−state dynamics, which include exciton recombination and the competition between forward and backward energy transfer. These two energy transfer processes are influenced by the Mn concentrations and band gap. With low concentration of Mn, the slightly mixed halide nanocrystals CsPb$(Cl_{1-y}By)_3$ exhibit efficient exciton−to−Mn energy transfer. This is attributed to the delayed exciton recombination and accelerated energy transfer rate. On the other hand, with a higher concentration of Mn, the increased Mn acceptors promote efficient energy transfer. Meanwhile, as the substitution moves from Cl to Br in mixed halide perovskite nanocrystals, the reduced band gap with increased electronic overlapping stimulate the backward transfer from Mn to the exciton. And it is difficult to accurately predict the excited−state dynamics with such complex forward and backward energy transfer. Hence, we constructed machine learning models with 86 initial data to deeper understanding the energy transfer. Our model is based on a KNN algorithm combined with regression analysis to predict and understand energy transfer accurately. Through machine learning modeling, it is possible to predict and understand the complicated energy transfer process. Significantly, ML−guided experimental strategies have the potential to discover of materials with preferable characteristics. Additionally, it helps revealing the structure−function relationships underlying physical processes in a broad multi−dimensional reaction design. By adjusting the concentrations of Mn and halide composition, we can change the intensities of dual emission of Mn−doped samples. Through further adjustments to its intensities, we discovered the potential for white−light emission. **(Figure A.27).** As a result of this study, we gain a better understanding of how Mn concentration and halide composition influences energy transfer in Mn−doped perovskite nanocrystals.

APPENDIX A

SUPPLEMENTARY FIGURES AND TABLES

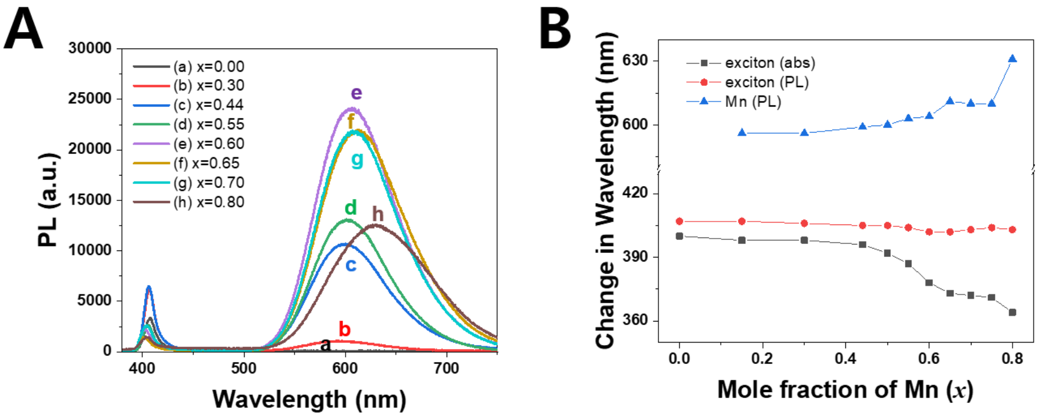

Figure A.1. (A) Unnormalized PL emission spectra recorded for Mn−doped $CsPbCl_3$ by altering mole fraction of Mn in the feed stock in the range of x = 0−0.80. (B) Change in wavelength of exciton (absorption and emission) and Mn (emission) with varying the Mn mole fraction from 0−0.80.

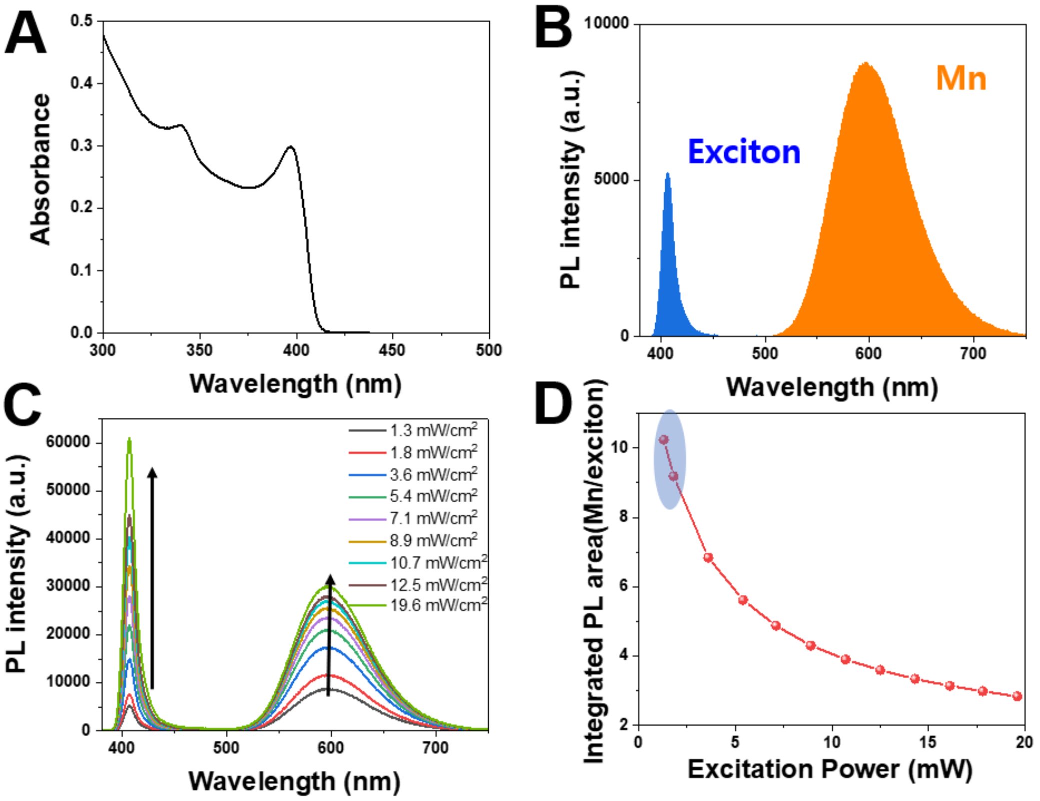

Figure A.2. (A) UV−vis absorption and (B) corresponding PL emission of Mn−doped CsPbCl$_3$ with $x = 0.44$ at the excitation power of 1.3 mW/cm^2. (C) Power−dependent PL emission spectra recorded as a function of changing the laser power from 1.3−19.6 mW/cm^2. (D) Corresponding integrated PL area emission intensity of Mn/exciton shown in panel C at different excitation power. In panel B, exciton emission (indicated as blue) *vs* Mn emission (indicated as orange) can be spectrally resolved and readily deconvoluted.

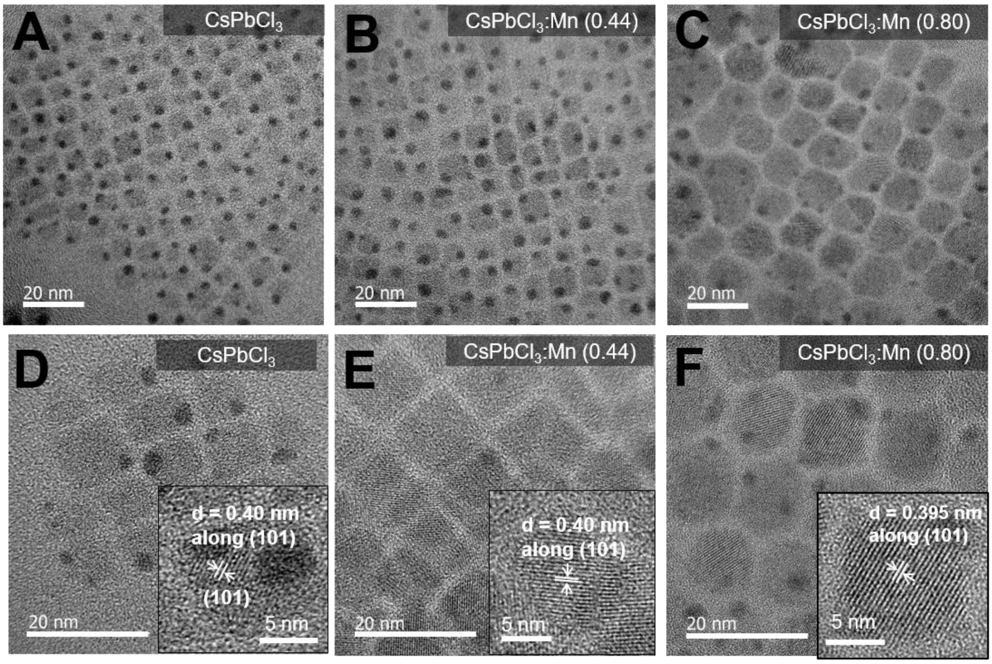

Figure A.3. Low−magnification (A−C) and high−magnification (D−F) transmission electron microscopy images acquired for undoped CsPbCl$_3$ (A,D), Mn−doped CsPbCl$_3$ with x = 0.44 (B,E), and Mn−doped CsPbCl$_3$ nanocrystals with x = 0.80 (C,F). Insets to D−F represent the magnified single nanocrystal with lattice fringes.

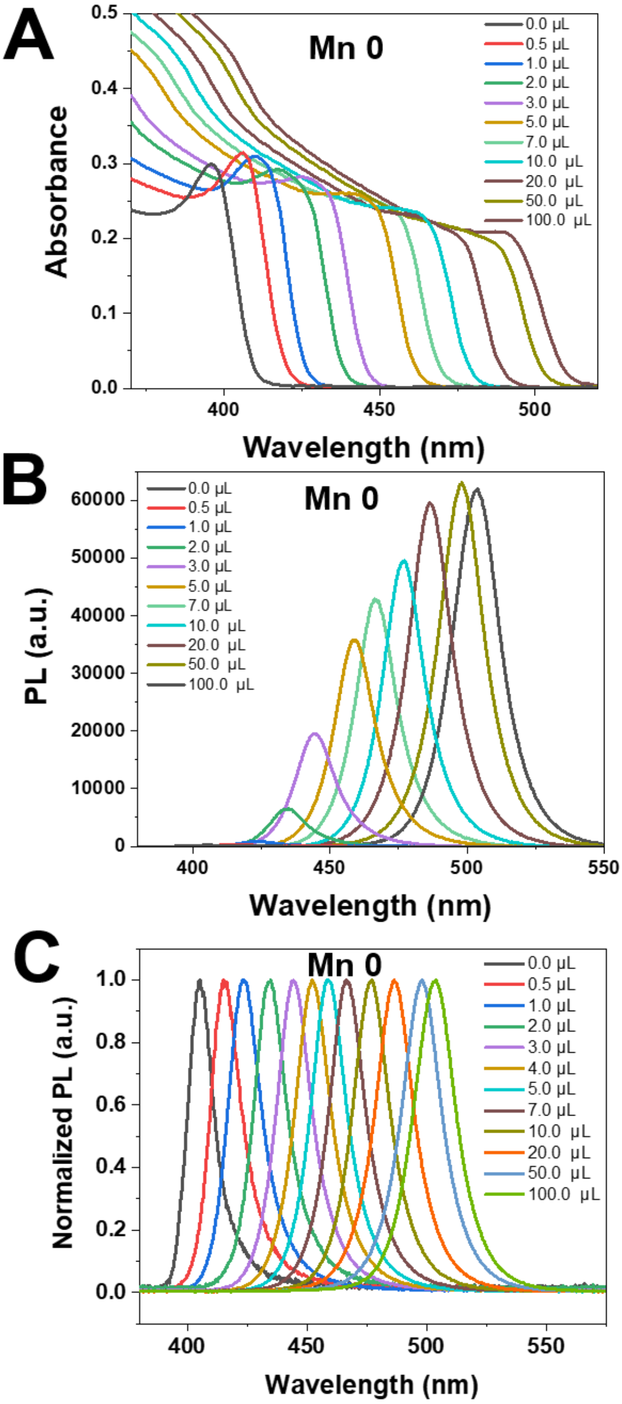

Figure A.4. (A) UV−vis absorption, (B) PL emission spectra, and (C) normalized PL emission spectra after addition of $PbBr_2$ solution (0.05 M) from 0−100 μL into undoped $CsPbCl_3$ nanocrystals

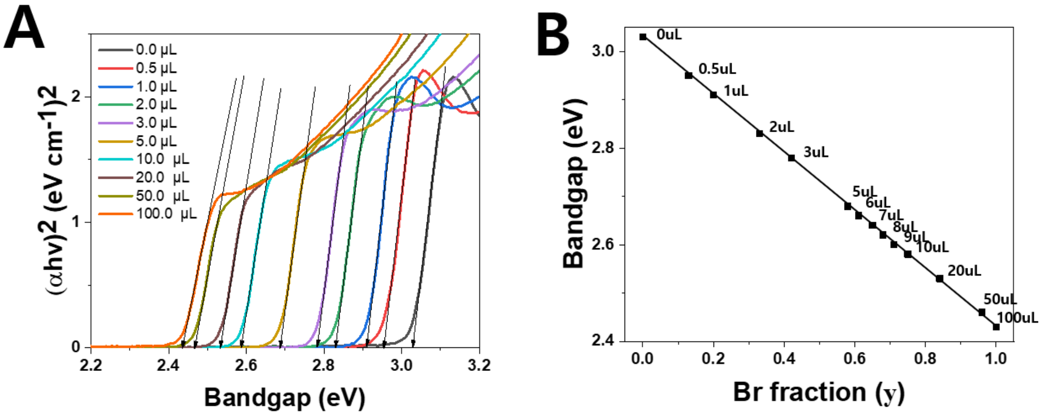

Figure A.5. (A) Tauc plot analysis of mixed halide perovskite nanocrystals stabilized by addition of variable volume of PbBr2 (0.05 M) solution from 0–100 μL into $CsPbCl_3$ nanocrystals. (B) Estimated bandgap of corresponding mixed halide $CsPb(Cl_{1-y}Br_y)_3$ perovskites nanocrystals as a function of varying the added amount of $PbBr_2$ solution (0.05 M). The bandgap was determined from the Tauc plots shown in panel A.

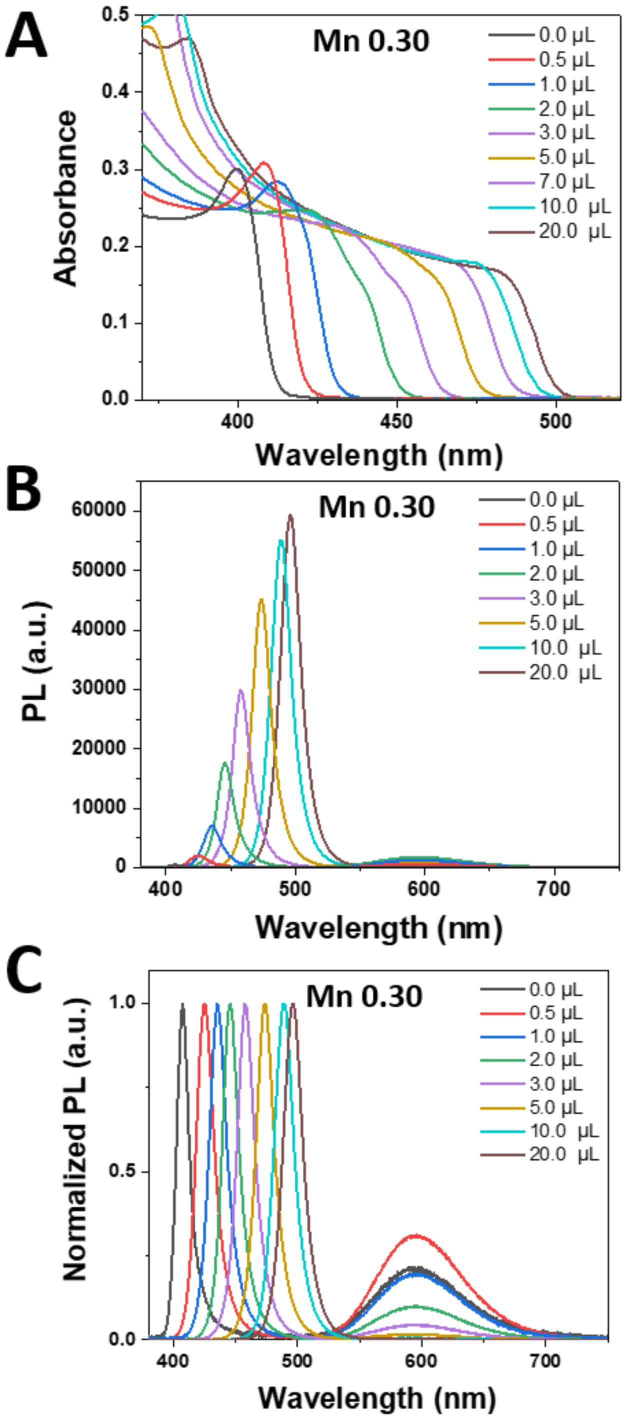

Figure A.6. (A) UV-vis absorption, (B) PL emission spectra, and (C) normalized PL emission spectra after addition of $PbBr_2$ solution (0.05 M) from 0–20 μL into Mn-doped $CsPbCl_3$ nanocrystals with x = 0.30.

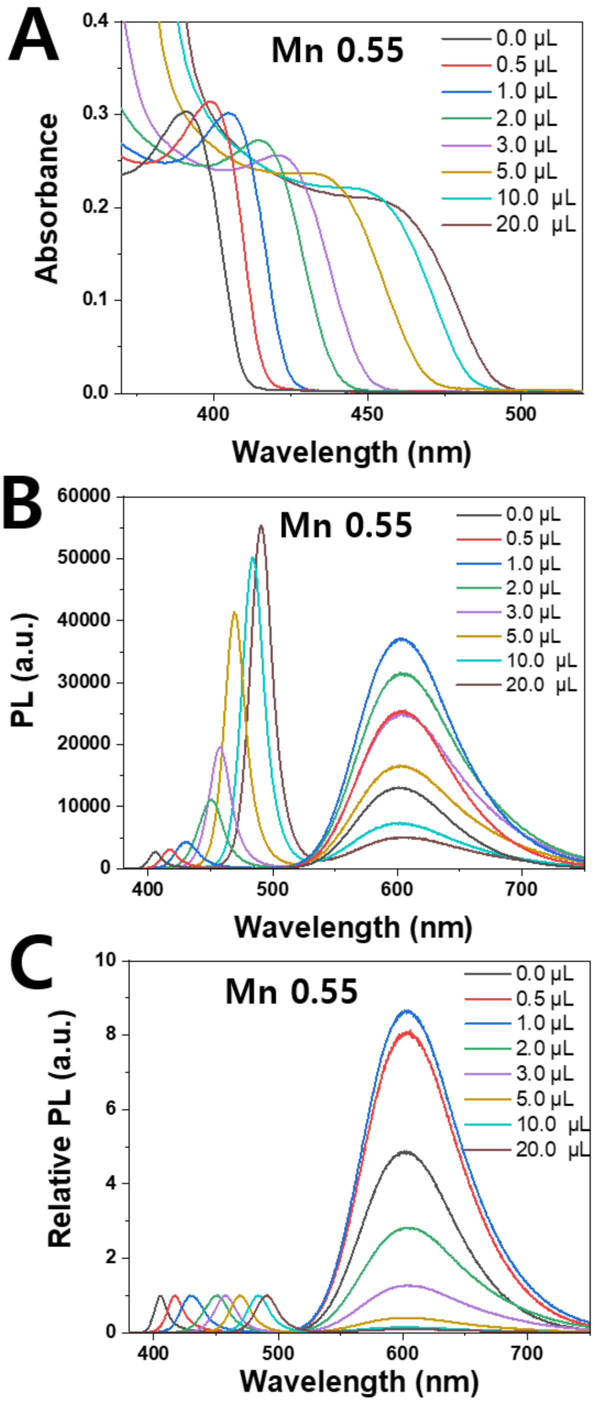

Figure A.7. (A) UV−vis absorption, (B) PL emission spectra, and (C) normalized PL emission spectra after addition of $PbBr_2$ solution (0.05 M) from 0−20 μL into Mn−doped $CsPbCl_3$ nanocrystals with x = 0.55.

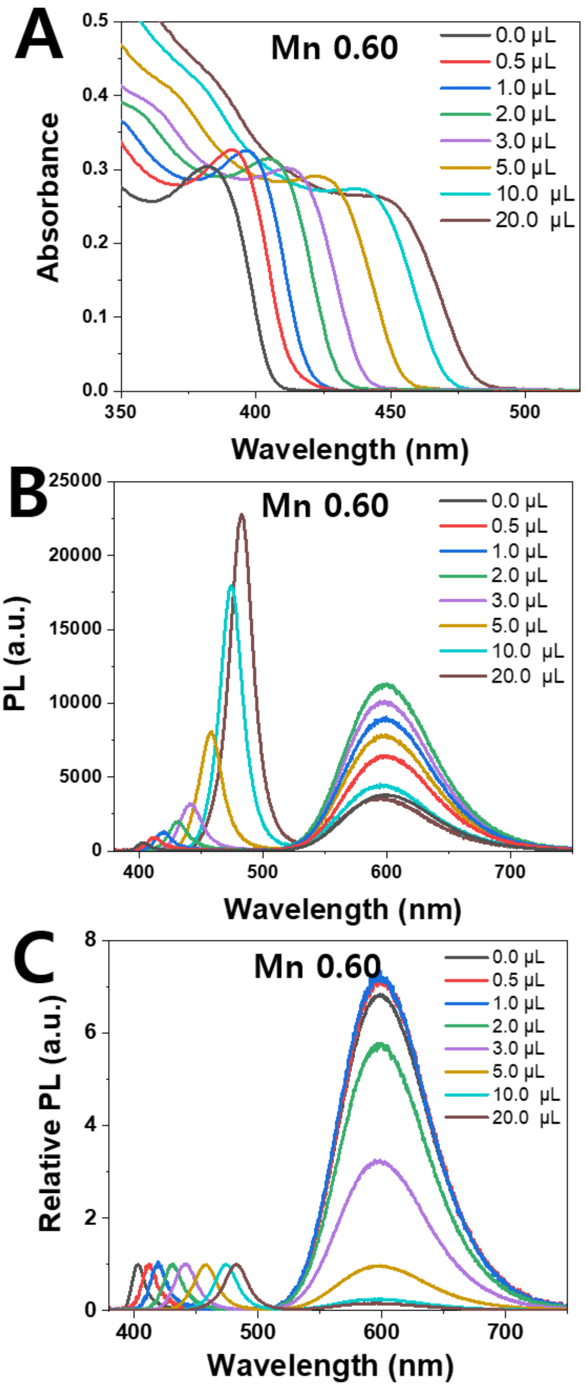

Figure A.8. (A) UV-vis absorption, (B) PL emission spectra, and (C) normalized PL emission spectra after addition of $PbBr_2$ solution (0.05 M) from 0-20 μL into Mn-doped $CsPbCl_3$ nanocrystals with x = 0.60.

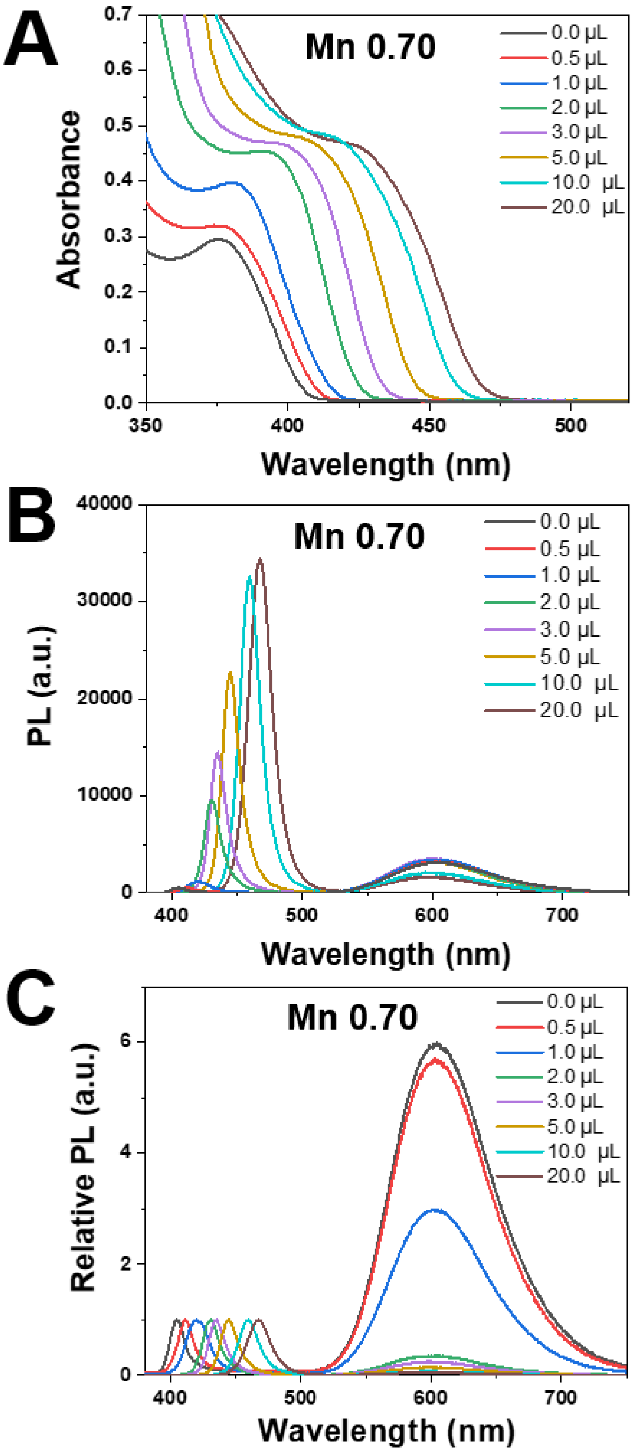

Figure A.9. (A) UV−vis absorption, (B) PL emission spectra, and (C) normalized PL emission spectra after addition of $PbBr_2$ solution (0.05 M) from 0−20 μL into Mn−doped $CsPbCl_3$ nanocrystals with x = 0.70.

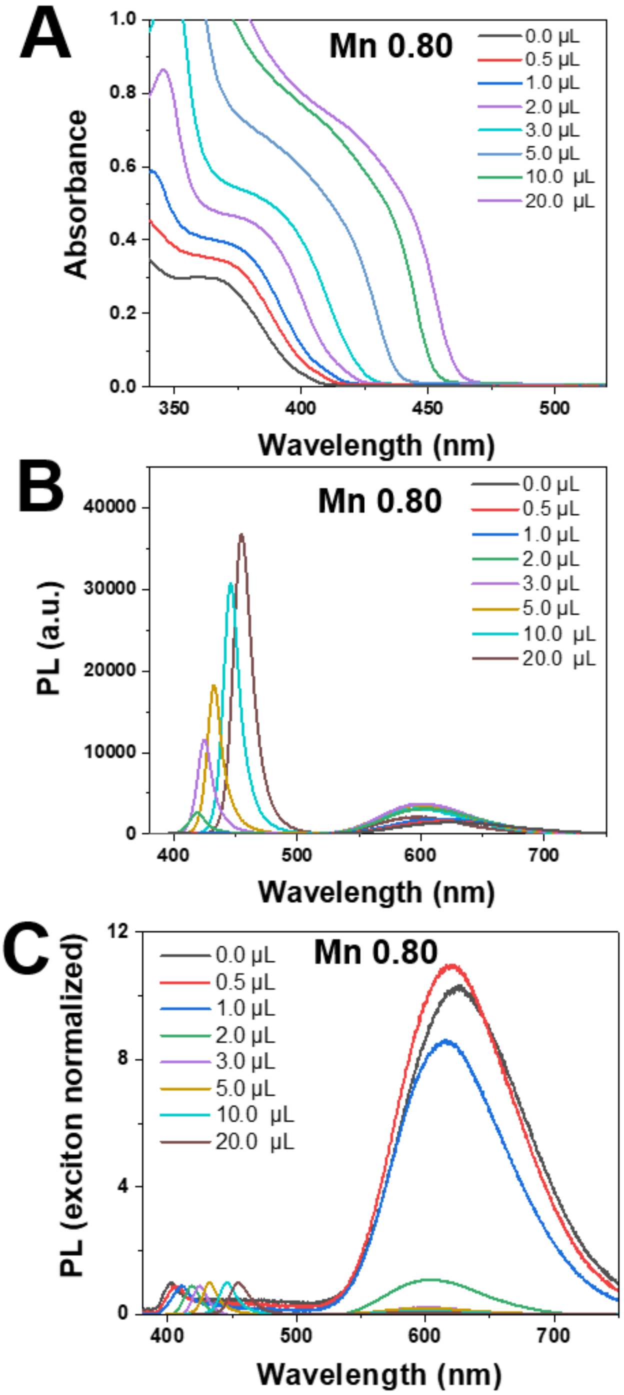

Figure A.10. (A) UV−vis absorption, (B) PL emission spectra, and (C) normalized PL emission spectra after addition of $PbBr_2$ solution (0.05 M) from 0−20 μL into Mn−doped $CsPbCl_3$ nanocrystals with x = 0.80.

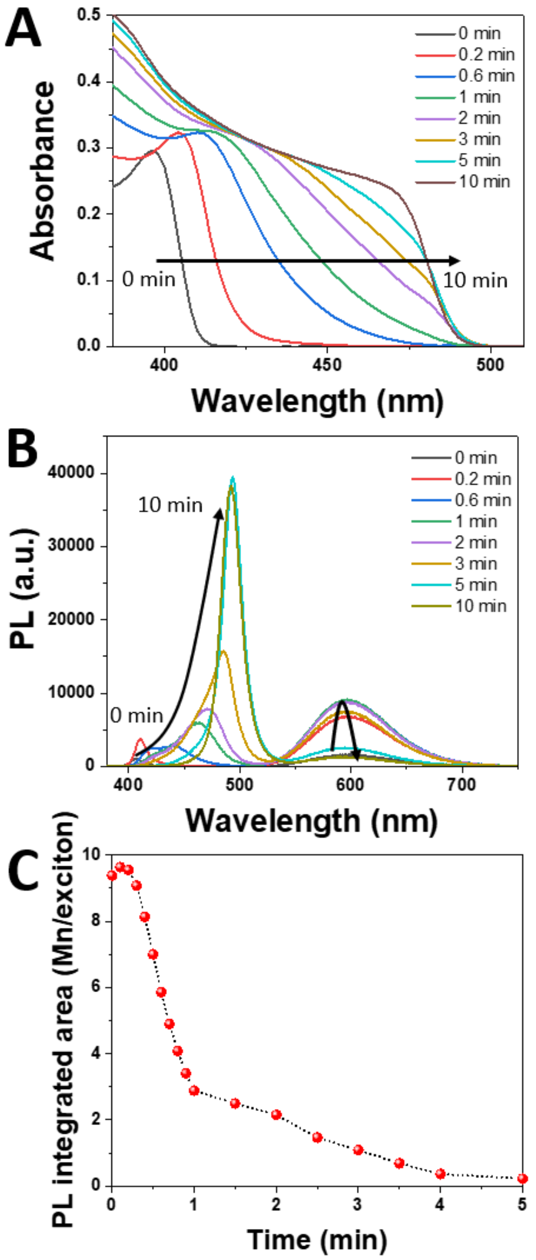

Figure A.11. (A,B) UV–vis absorption (A) and PL emission spectra (B) changes recorded after adding 20 μL of $PbBr_2$ (0.05 M) solution into Mn(x)–doped $CsPbCl_3$ nanocrystals with x = 0.44 over the course of reaction time 10 mins. (C) Corresponding integrated PL emission ratio between Mn/exciton shown in the panel B of PL spectra.

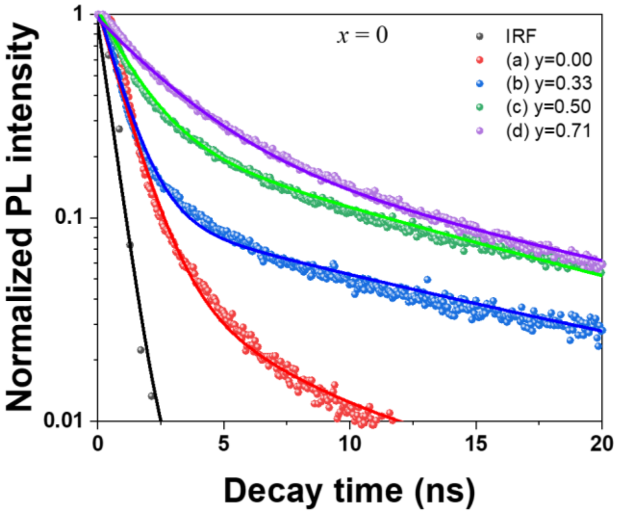

Figure A.12. PL decay traces and corresponding kinetic fitting using biexponential fits monitoring the undoped $CsPb(Cl_{1-y}Br_y)_3$ exciton emission (A) at 404 (a), 450 (b), 470 (c), and 490 nm (d), respectively.

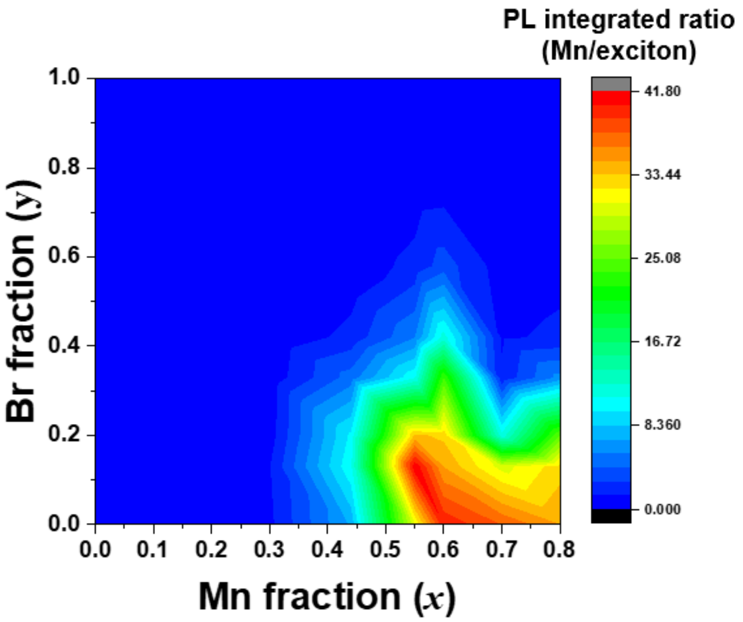

Figure A.13. 2D color mapping for the integrated Mn/exciton PL emission intensity as a function of varying the dopant Mn concentration (x) and Br (y) in Mn-doped $CsPb(Cl_{1-y}Br_y)_3$ nanocrystals.

Table A.1. Kinetic fitting parameters obtained using biexponential fitting with different Mn fraction x from 0–0.80 in Mn–doped $CsPbCl_3$ nanocrystals: average lifetimes (τ_{ave}), its individual lifetimes (τ_1 and τ_2), and the corresponding amplitudes (A_1 and A_2) of exciton and Mn emission, respectively.

Mn fraction (x)	**A_1**	**τ_1 (ns)**	**A_2**	**τ_2 (ns)**	**$\tau_{ave}^{Exciton}$(ns)**	**Exciton_ PL QY (%)**
0.00	0.93	0.53	0.07	3.16	1.34	1.7
0.30	0.92	0.49	0.08	1.99	0.87	0.45
0.44	0.91	0.49	0.09	1.82	0.85	0.65
0.55	0.89	0.41	0.10	0.68	0.45	0.46
0.70	0.80	0.39	0.20	0.58	0.44	0.82
0.80	0.79	0.38	0.21	0.59	0.44	0.70
Mn fraction (x)	**A_1**	**τ_1 (μs)**	**A_2**	**τ_2 (μs)**	**τ_{ave}^{Mn}(μs)**	**Mn_PL QY (%)**
0.30	0.03	35.9	0.97	1647	1643	0.45
0.44	0.04	141.3	0.96	1580	1574	6.5
0.55	0.23	146.1	0.77	1033	997	10.5
0.70	0.32	110.6	0.68	999	955	36.2
0.80	0.35	126.3	0.65	812	758	25.8

Table A.2. Calculated rate constants and energy transfer efficiency from **Table A. 1.**

Mn fraction (*x*)	$k_r^{Exciton}$	$k_{nr}^{Exciton}$	k_r^{Mn}	k_{nr}^{Mn}	k_{ET}	Φ_{ET}
0.00	1.27E+07	7.36E+08	-	-	-	-
0.30	3.37E+06	0.74E+09	0.29E+01	6.32E+02	1.15E+09	0.35
0.44	7.58E+06	1.17E+09	4.10E+01	5.94E+02	6.70E+08	0.36
0.55	1.02E+07	2.21E+09	1.06E+02	8.96E+02	4.35E+09	0.66
0.70	1.86E+07	2.23E+09	3.80E+02	6.67E+02	4.52E+09	0.67
0.80	1.57E+07	2.24E+09	3.40E+02	9.79E+02	4.52E+09	0.67

Table A.3. Kinetic fitting parameters obtained using biexponential fitting for Mn−doped $CsPb(Cl_{1-y}Br_y)_3$ nanocrystals with $x = 0.44$ upon changing Br content y from 0−0.71: average lifetimes (τ_{ave}), its individual lifetimes (τ_1 and τ_2), and the corresponding amplitudes (A_1 and A_2) of exciton and Mn emission, respectively.

Br fraction (*y*)	**A_1**	**τ_1 (ns)**	**A_2**	**τ_2 (ns)**	**$\tau_{ave}^{Exciton}$ (ns)**	**Exciton_ PL QY (%)**
0.00	0.91	0.49	0.09	1.82	0.85	0.6
0.33	0.90	0.90	0.10	12.54	8.09	5.2
0.50	0.82	1.12	0.18	11.50	8.29	8.3
0.71	0.85	2.84	0.16	16.03	9.54	16.1
Br fraction (*y*)	**A_1**	**τ_1 (µs)**	**A_2**	**τ_2 (µs)**	**τ_{ave}^{Mn} (µs)**	**Mn_PL QY (%)**
0.00	0.04	141.3	0.96	1580	1574	6.5
0.33	0.20	352.4	0.80	848	800	7.5
0.50	0.15	11.8	0.85	474	472	1.9
0.71	0.68	38.4	0.33	153	114	0.6

Table A.4. Kinetic fitting parameters obtained using biexponential fitting for undoped $CsPb(Cl_{1-y}Br_y)_3$ nanocrystals with x = 0.0 upon changing Br content y from 0−0.71: average lifetimes (τ_{ave}), its individual lifetimes (τ_1 and τ_2), and the corresponding amplitudes (A_1 and A_2) of exciton and Mn emission, respectively.

Br fraction (y)	**A_1**	**τ_1 (ns)**	**A_2**	**τ_2 (ns)**	**$\tau_{ave}^{Exciton}$ (ns)**	**Exciton_ PL QY (%)**
0.00	0.95	0.95	0.05	4.9	1.82	0.3
0.33	0.92	0.90	0.08	14.0	8.57	4.4
0.50	0.77	1.45	0.23	11.6	8.67	28.1
0.71	0.76	2.75	0.24	14.0	9.69	53.9

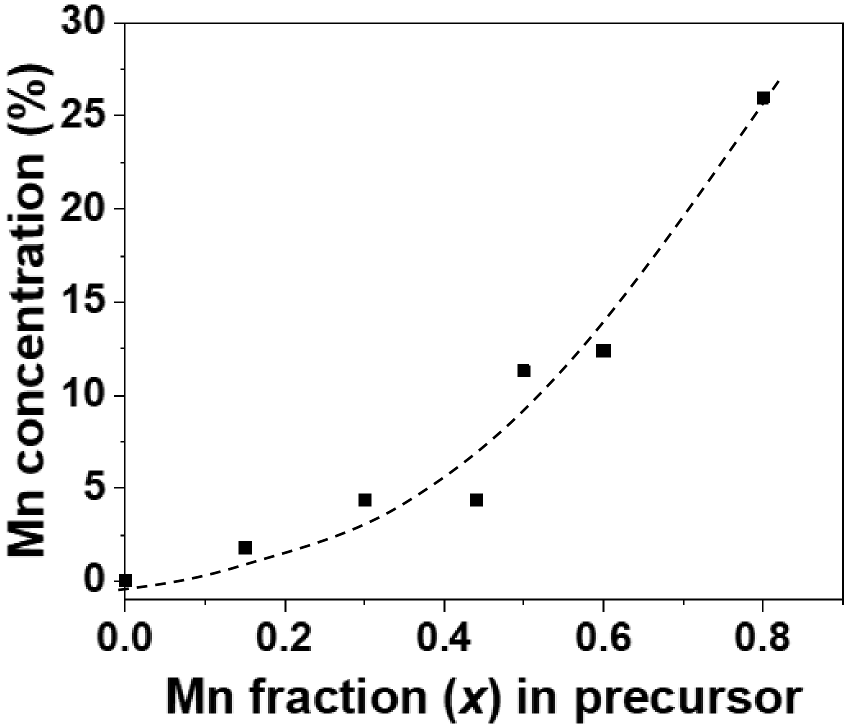

Figure A.14. Actually-doped Mn concentration (atom %) in lead halide perovskite nanocrystals determined by induced coupled plasma atomic emission spectra (ICP-AES) as a function of varying the Mn fraction (*x*) in the precursor solution. The dashed line is a guide line for the eyes.

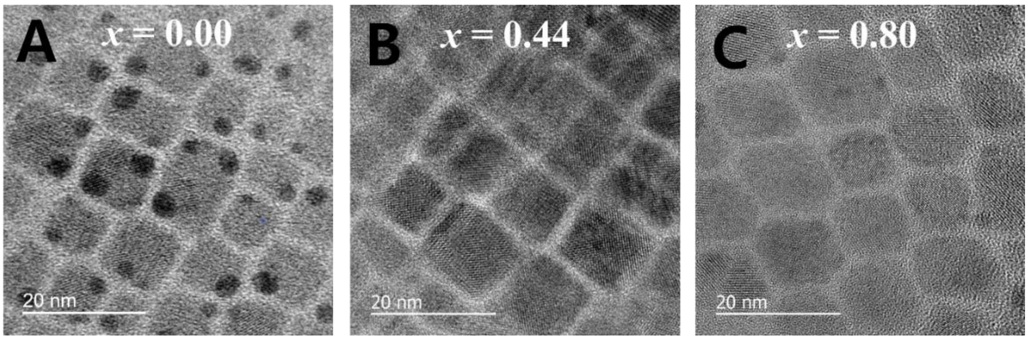

Figure A.15. Transmission electron microscope (TEM) images acquired for undoped (A) $CsPbCl_3$ and Mn−doped $CsPbCl_3$ nanocrystals with (B) x=0.44 and (C) x=0.80, respectively.

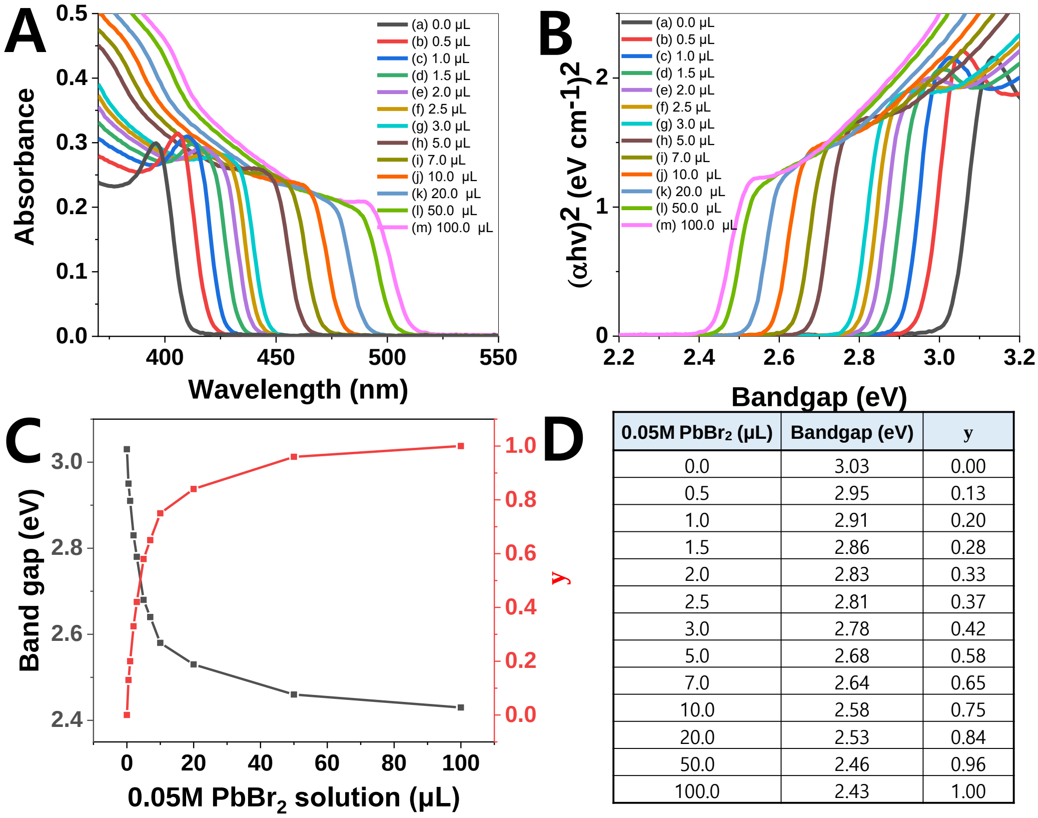

0.05M PbBr$_2$ (μL)	Bandgap (eV)	y
0.0	3.03	0.00
0.5	2.95	0.13
1.0	2.91	0.20
1.5	2.86	0.28
2.0	2.83	0.33
2.5	2.81	0.37
3.0	2.78	0.42
5.0	2.68	0.58
7.0	2.64	0.65
10.0	2.58	0.75
20.0	2.53	0.84
50.0	2.46	0.96
100.0	2.43	1.00

Figure A.16. (A,B) UV−vis absorption (A) and corresponding Tauc plots (B) for $CsPb(Cl_{1-y}Br_y)_3$ nanocrystals stabilized when $PbBr_2$ (0.05M) solution (0−100 μL) was added to parent $CsPbCl_3$ nanocrystals. (C) Estimated bandgap (eV) and y (y = 0−1) as a function of 0.05M $PbBr_2$ volume (μL) that is determined from Tauc plot shown in panel B. (D) A table summarizing the added $PbBr_2$ volume, bandgap, and y value, respectively.

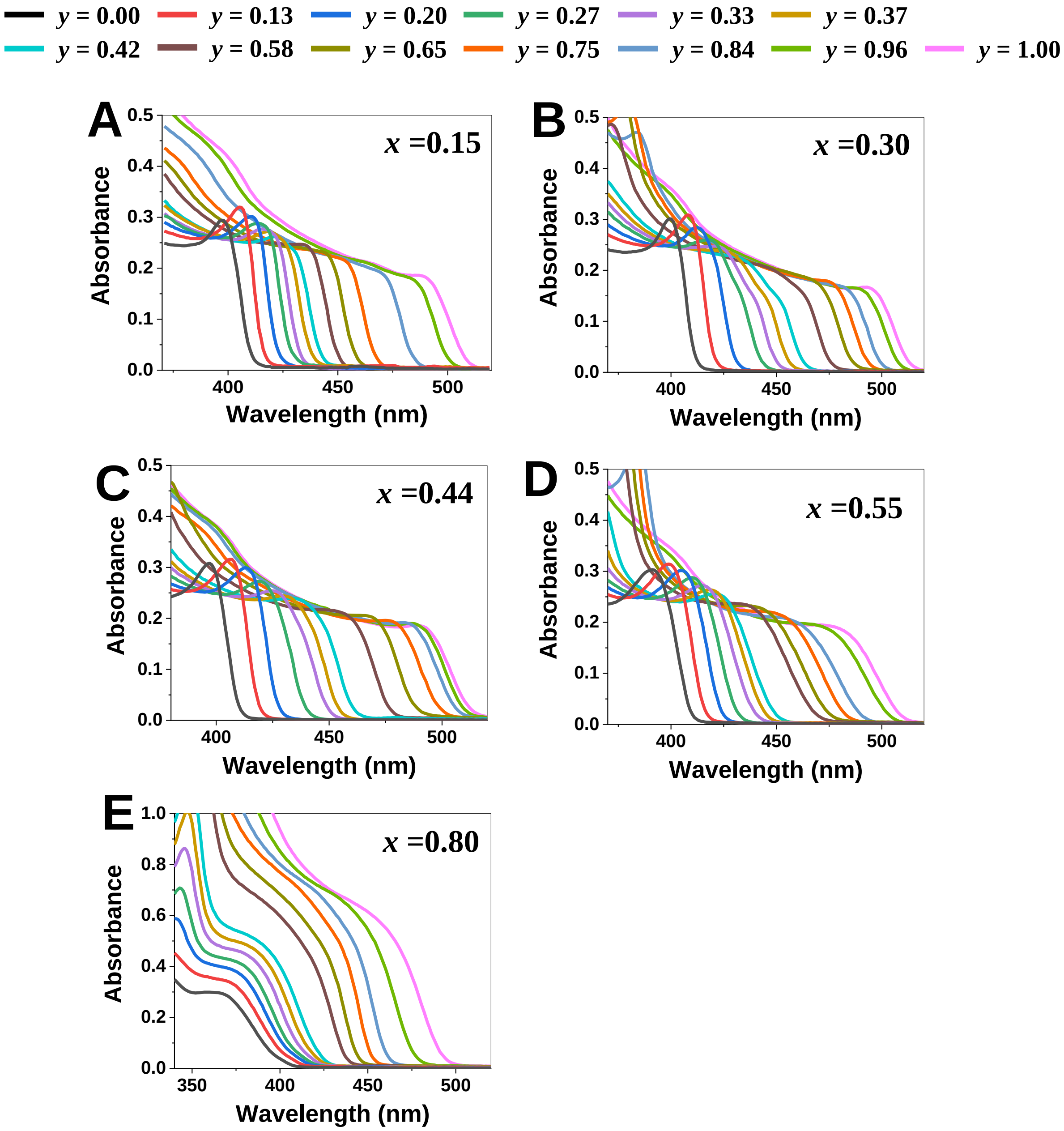

Figure A.17. (A–E) UV–vis absorption spectra evolution during the course of anion exchange by adding 0.05M $PbBr_2$ solution from 0–100 μL into Mn-doped $CsPbCl_3$ with different Mn concentration: (A) x = 0.15, (B) x = 0.30, (C) x = 0.44, (D) x = 0.55, and (E) x = 0.80, respectively. The y value was determined from the Tauc plot analysis as illustrated in Figure S3

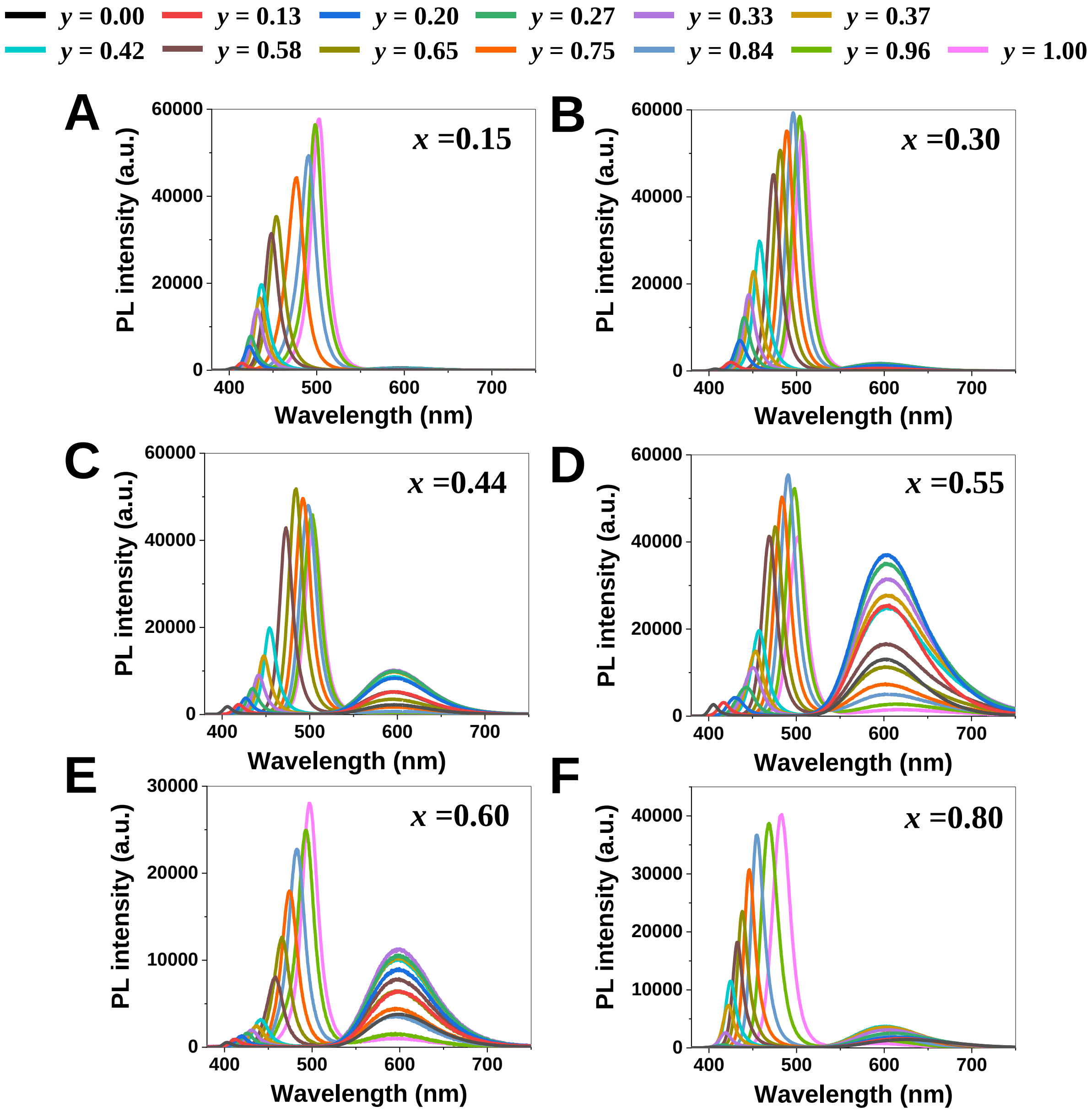

Figure A.18. (A−F) PL emission spectra evolution during the course of anion exchange by adding 0.05M PbBr$_2$ solution from 0−100 μL into Mn−doped CsPbCl$_3$ with different Mn concentration: (A) x = 0.15, (B) x = 0.30, (C) x = 0.44, (D) x = 0.55, (E) x = 0.60, and (F) x = 0.80, respectively. The y value was determined from the Tauc plot analysis as illustrated in Figure S3

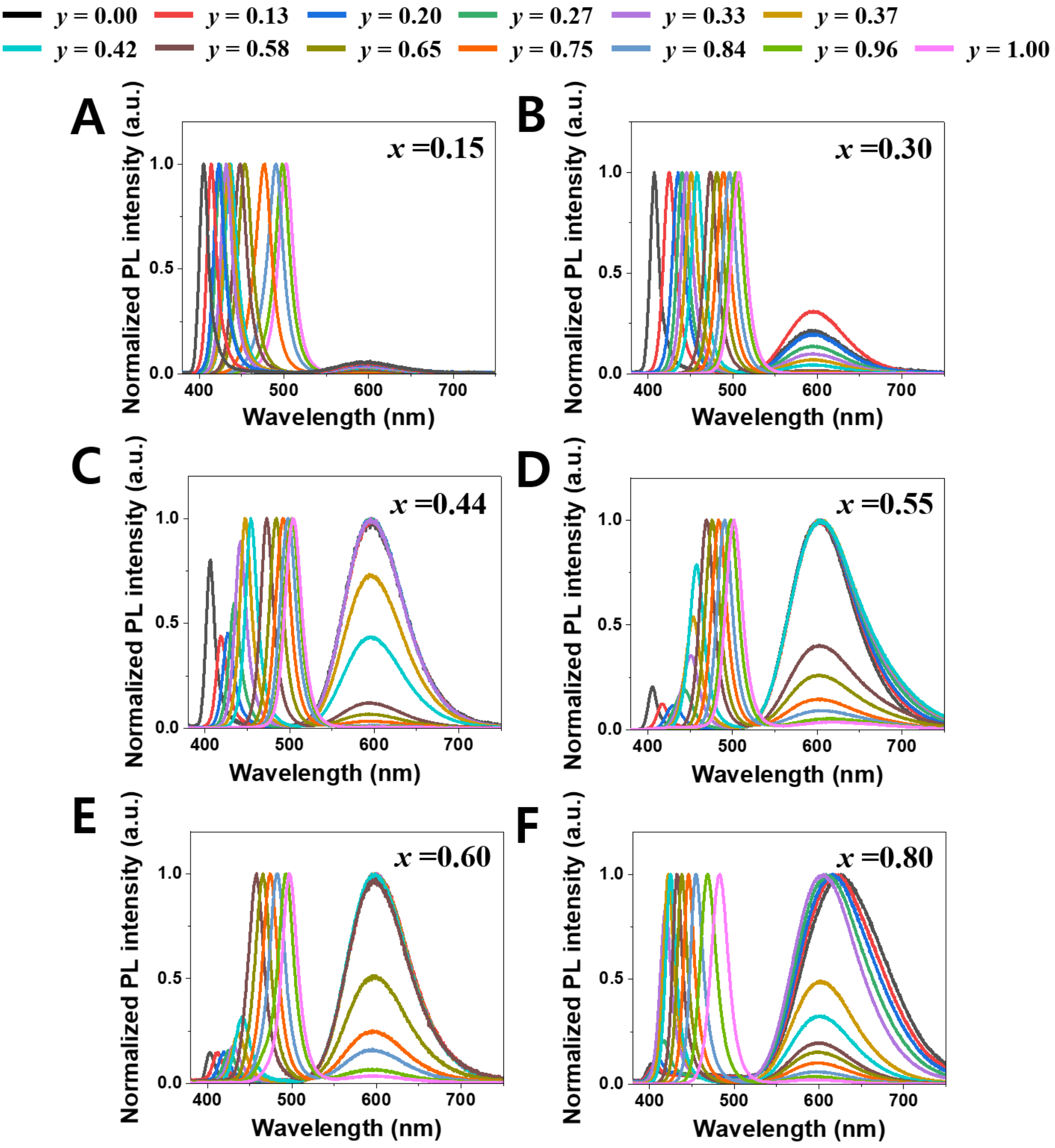

Figure A.19. (A–F) Normalized PL emission spectra evolution during the course of anion exchange by adding 0.05M $PbBr_2$ solution from 0–100 μL into Mn-doped $CsPbCl_3$ with different Mn concentration: (A) $x = 0.15$, (B) $x = 0.30$, (C) $x = 0.44$, (D) $x = 0.55$, (E) $x = 0.60$, and (F) $x = 0.80$, respectively. The y value was determined from the Tauc plot analysis as illustrated in Figure S3

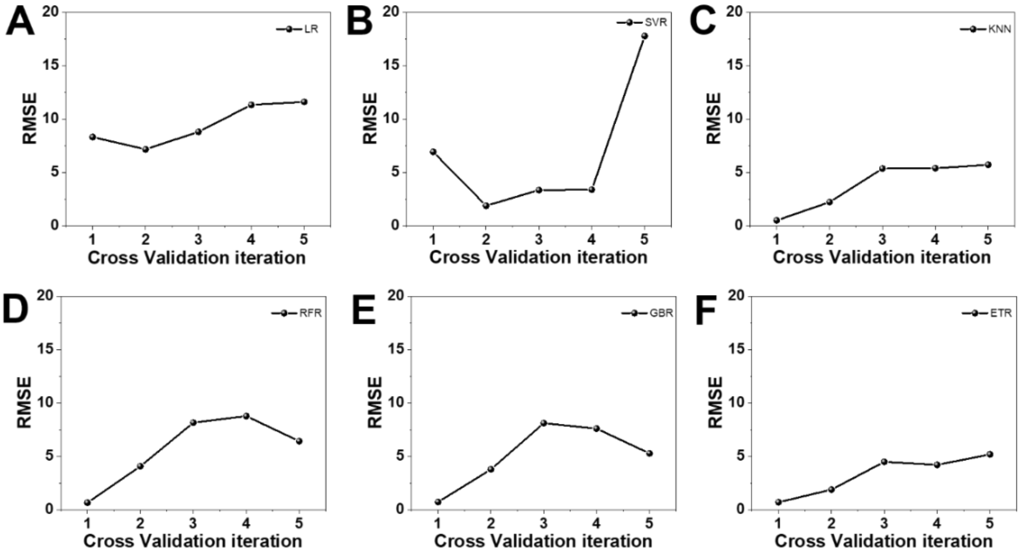

Figure A.20. (A–F) RMSE changes over five iterations during the process five-fold cross validation using different machine learning algorithms: (A) LR, (B) SVR, (C) KNN, (D) RFR, (E) GBR, and (F) ETR.

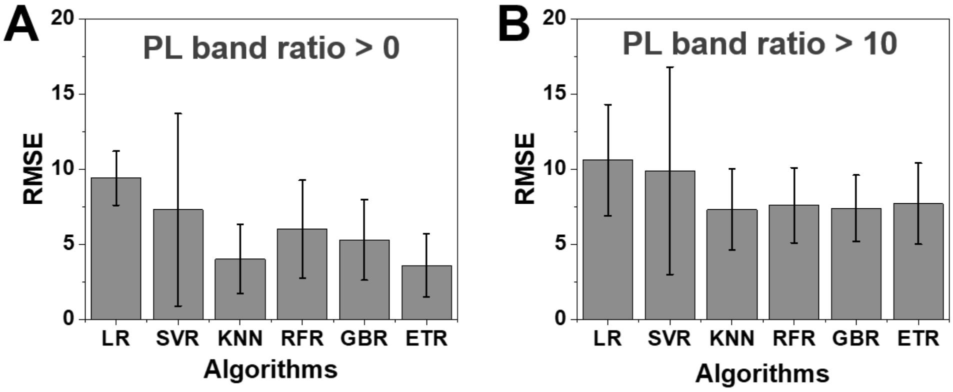

Figure A.21 (A,B) Five−fold cross−validation root mean square error (RMSE) of different machine learning algorithm models upon filtering off the energy transfer value larger than 0 (A) or 10 (B). Six different regression models were used for prediction of energy transfer.

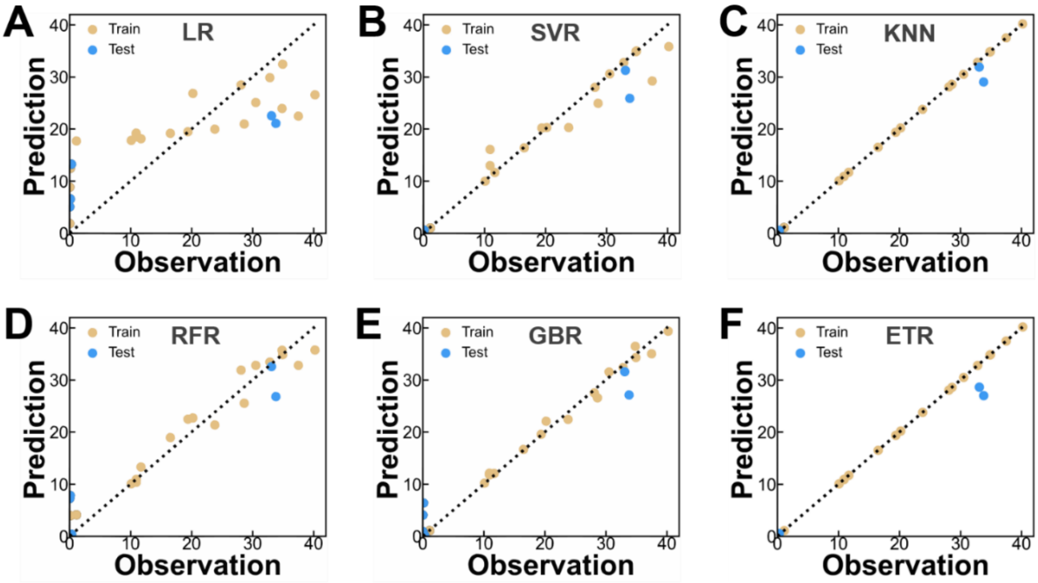

Figure A.22. (A−F) Regression results of predicted and observed energy transfer seen in Mn-doped CsPb(Cl$_{1-y}$Br$_y$)$_3$ nanocrystals using different regression models: (A) linear regression (R^2 = 0.653), (B) support vector regression (R^2 = 0.948), (C) k-nearest neighbor regression ((R^2 = 0.984), (D) random forest regression (R^2 = 0.891), (E) gradient boosting regression ((R^2 = 0.930), and (F) extra tree regression (R^2 = 0.955).

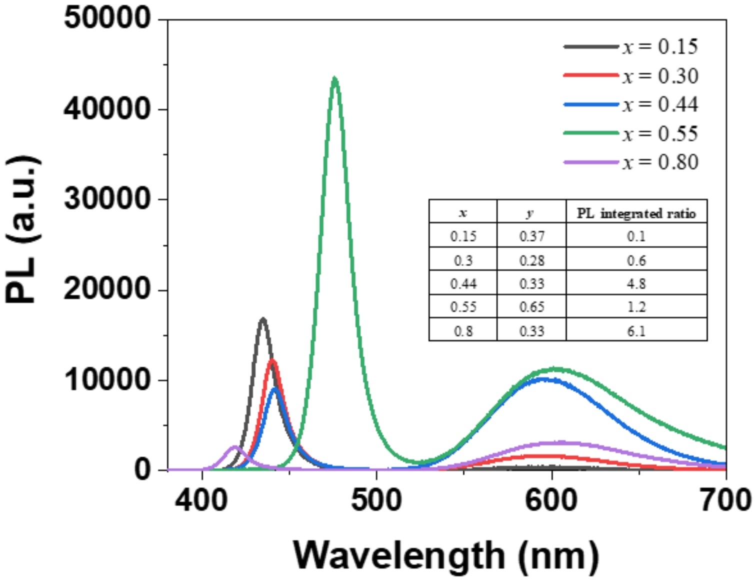

x	*y*	PL integrated ratio
0.15	0.37	0.1
0.3	0.28	0.6
0.44	0.33	4.8
0.55	0.65	1.2
0.8	0.33	6.1

Figure A.23. PL spectra for new 5 samples with different x and y that are randomly selected by algorithm.

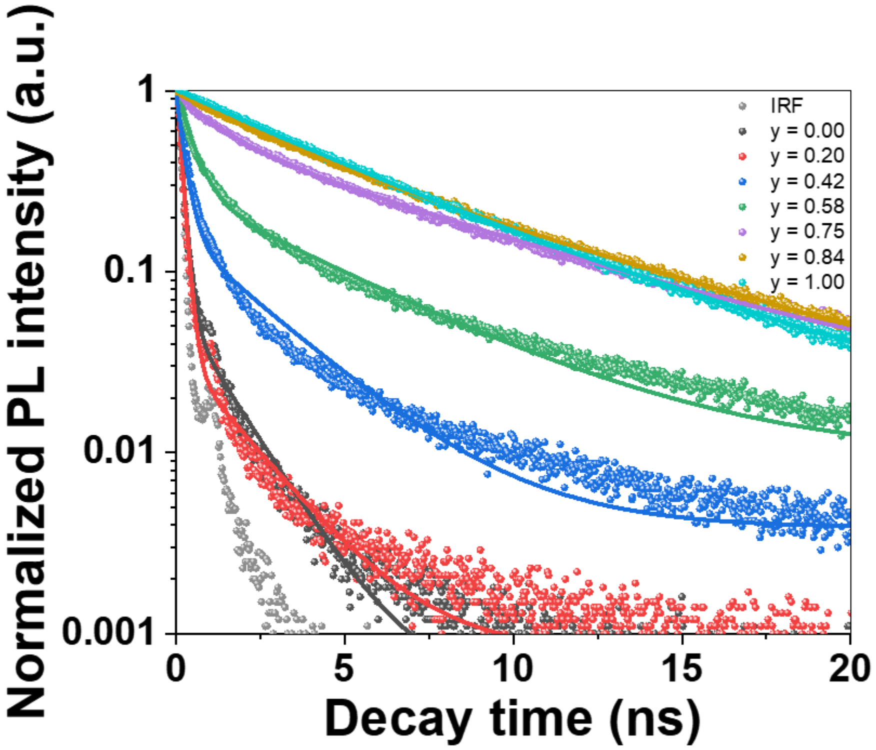

Figure A.24. PL decay traces and kinetic fittings using undoped $CsPbCl_3$ upon bromide exchange from y = 0−1 by monitoring the exciton peak of 405 (y = 0.00), 416 (y = 0.20), 430 (y = 0.42), 440 (y = 0.58), 460 (y = 0.75), 482 (y = 0.84), and 509 nm (y = 1.0) respectively.

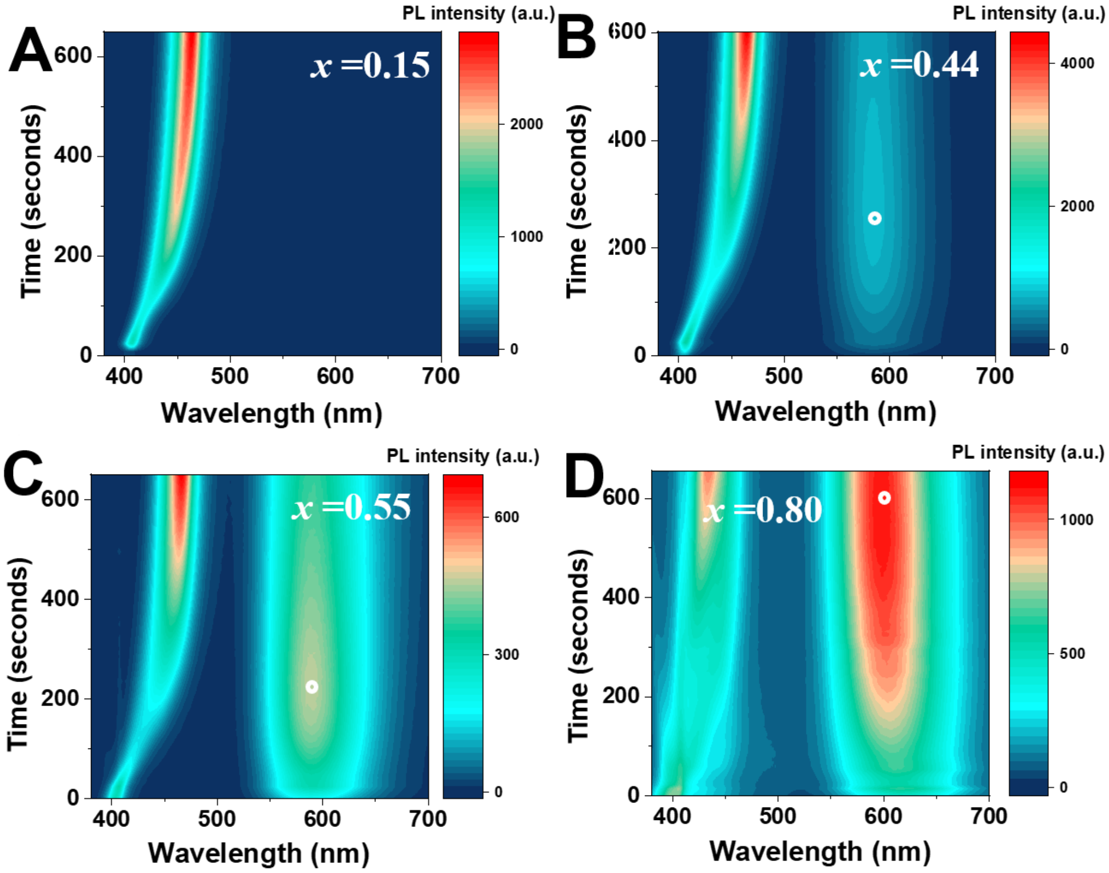

Figure A.25. 2D PL emission color mapping during the course of anion exchange for initial 500 sec by dumping 5 μL of 0.05M PbBr into Mn-doped $CsPbCl_3$ nanocrystals with different Mn concentration: (A) x=0.15, (B) x=0.30, (C) x=0.44, (D) x=0.55, (E) x=0.60, and (F) x=0.80, respectively. The point shown in the color map represent the time corresponding to the maximum peak of Mn.

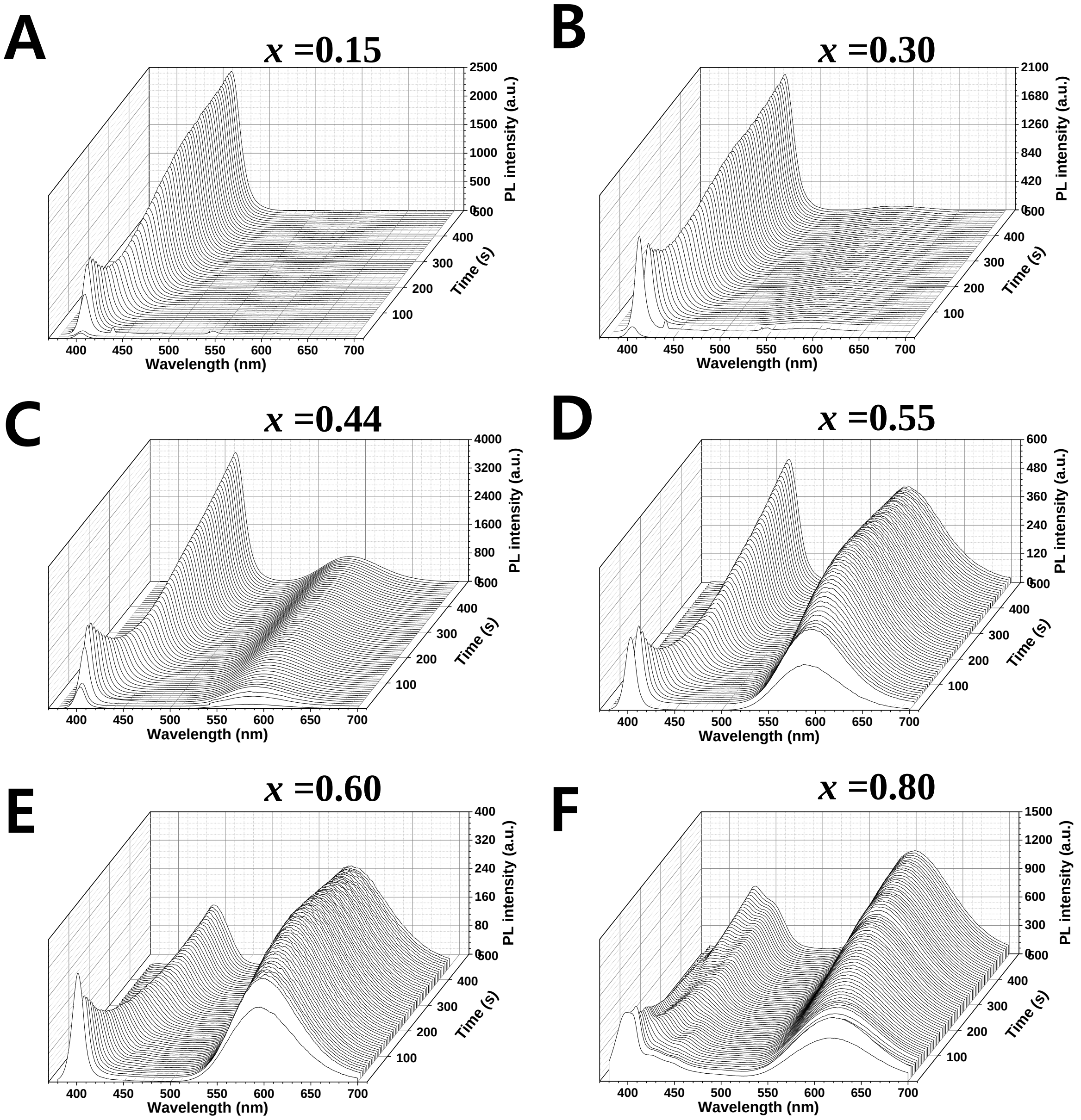

Figure A.26. 2D waterfall PL emission plots during the course of the anion exchange for initial 500 sec by dumping 5 μL of 0.05M PbBr into Mn-doped $CsPbCl_3$ nanocrystals with different Mn concentration: (A) *x*=0.15, (B) *x*=0.30, (C) *x*=0.44, (D) *x*=0.55, (E) *x*=0.60, and (F) *x*=0.80, respectively. 2D waterfall PL emission plots corresponds to the 2D PL emission color maps shown in Figure S10.

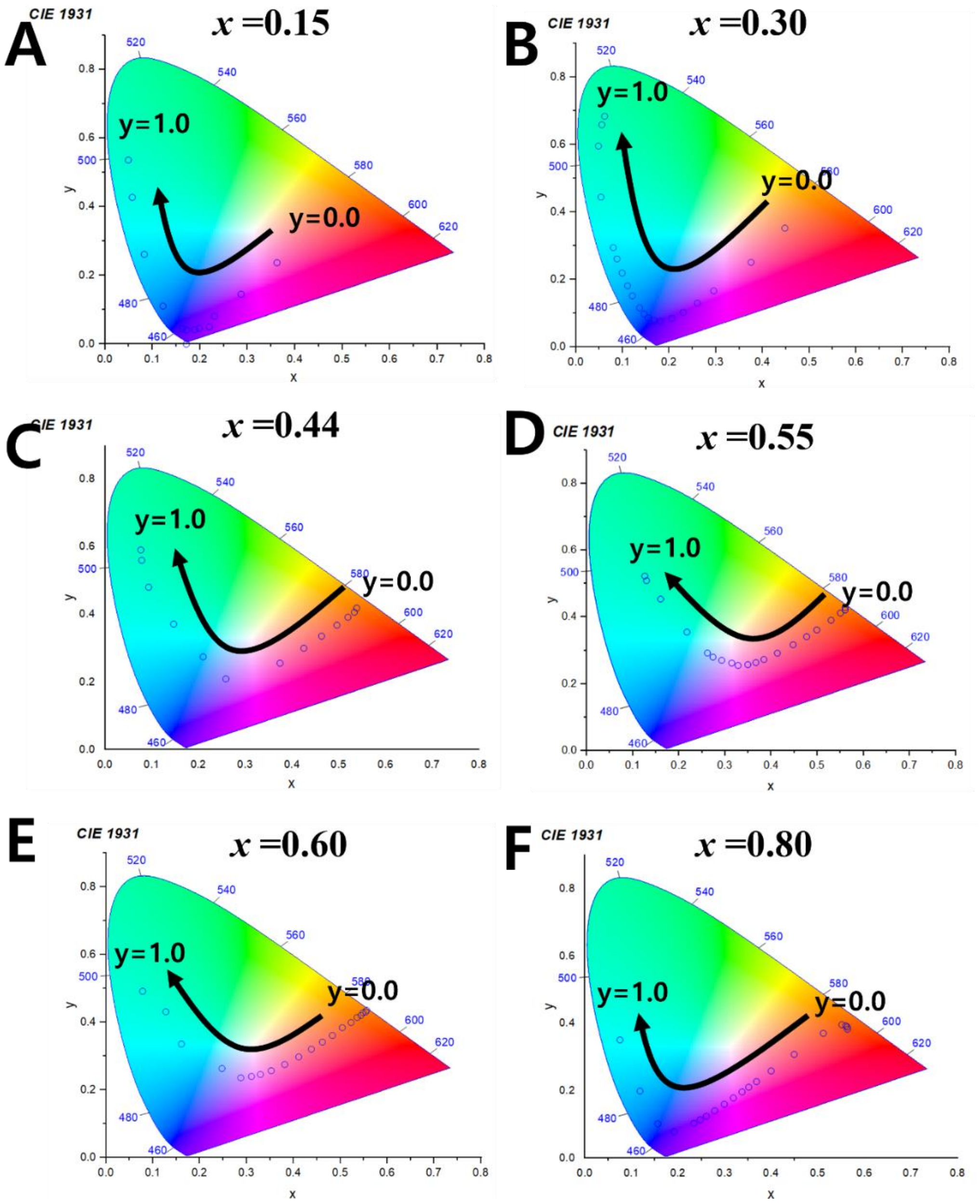

Figure A.27. CIE coordinate diagrams during the anion exchange by adding 0.05M $PbBr_2$ solution from 0−100 μL into Mn−doped $CsPbCl_3$ with different Mn concentration: (A) x = 0.15, (B) x = 0.30, (C) x = 0.44, (D) x = 0.55, and (E) x = 0.80, respectively. The curved arrows indicate the color point changes during anion exchange.

Table A.5. Initial dataset of 86 samples used for machine learning corresponding to PL emission band ratio (Mn/exciton) obtained with varying initial feeding Mn fraction (*x*) and Br concentration (*y*). Five new data was randomly selected and used for validating the finally constructed models.

x ***y***	**0.00**	**0.15**	**0.30**	**0.44**	**0.55**	**0.60**	**0.80**
0.00	0.00	0.30	1.05	6.91	28.80	40.21	34.90
0.13	0.00	0.26	1.33	10.16	38.60	34.78	32.79
0.20	0.00	0.20	0.69	9.63	33.75	33.09	28.08
0.28	0.00	0.18	New data	7.22	19.41	28.57	20.22
0.33	0.00	0.15	0.44	New data	10.94	23.82	New data
0.37	0.00	New data	0.30	3.15	8.04	16.48	2.52
0.42	0.00	0.09	0.18	1.87	5.55	11.74	1.65
0.58	0.00	0.06	0.06	0.52	1.83	3.46	1.01
0.65	0.00	0.03	0.04	0.28	New data	1.76	0.76
0.75	0.00	0.01	0.01	0.14	0.64	0.79	0.43
0.84	0.00	0.00	0.01	0.06	0.42	0.46	0.24
0.96	0.00	0.00	0.00	0.04	0.10	0.12	0.12
1.00	0.00	0.00	0.00	0.01	0.00	0.05	0.06

Table A.6. Hyperparameters search space in grid search.

Machine learning algorithms	Hyperparameters	Search space	Best value
LR	-	-	-
KNN	weights	['uniform', 'distance']	distance
	n_neighbors	[2, 50]	2
	algorithm	['ball_tree', 'kd_tree' , 'brute']	ball_tree
RFR	max_depth	[1,10]	4
	n_estimators	[3,50]	9
GBR	max_depth	[1,10]	3
	n_estimators	[5,500]	200
SVR	C	[1e0,5, 1e1,50, 1e2,5e2,1e3]	500
ETR	n_estimators	[10,500]	20

Table A.7. Performance metrics for all machine learning models using dataset of 86 samples with PL band ratio larger than 0.

PL band ratio > 0	LR	SVR	KNN	RFR	GBR	ETR
CrossValidation RMSE	9.4	7.3	4.0	6.0	5.3	3.6
CrossValidation SD	1.8	6.4	2.3	3.3	2.7	2.1
Train RMSE	8.1	1.8	0.0	1.9	0.3	0.0
Test MSE	56.3	9.2	2.6	3.8	3.3	2.5
Test RMSE	7.5	3.0	1.6	1.9	1.8	1.6
Test MAE	6.2	1.6	0.7	0.9	1.0	0.8
Test R^2	0.556	0.927	0.980	0.970	0.974	0.980

Table A.8. Performance metrics for all machine learning models using dataset of 28 samples with filtering out the PL band ratio value smaller than 10.

PL band ratio > 10	**LR**	**SVR**	**KNN**	**RFR**	**GBR**	**ETR**
CrossValidation RMSE	10.6	9.9	7.3	7.6	7.4	7.7
CrossValidation SD	3.7	6.9	2.7	2.5	2.2	2.7
Train RMSE	8.5	2.6	0.0	2.4	1.0	0.0
Test MSE	85.7	12.9	4.0	26.9	17.2	11.0
Test RMSE	9.3	3.6	2.0	5.2	4.2	3.3
Test MAE	8.3	2.4	1.0	3.8	3.3	2.0
Test R^2	0.653	0.948	0.984	0.891	0.930	0.955

Table A.9. Performance metrics for all machine learning models using new dataset of 5 samples with PL band ratio value larger than 0.

PL band ratio > 0	**LR**	**SVR**	**KNN**	**RFR**	**GBR**	**ETR**
New data MSE	45.6	2.8	0.1	3.2	0.2	0.6
New data RMSE	6.8	1.7	0.4	1.8	0.5	0.8
New data MAE	6.4	1.1	0.2	1.2	0.4	0.4
New data R^2	-6.778	0.517	0.978	0.457	0.963	0.898

Table A.10. Kinetic fitting parameters obtained using biexponential fitting for undoped $CsPb(Cl_{1-y}Br_y)_3$ nanocrystals upon changing Br content y from 0−1.00 : average lifetimes (τ_{ave}), its individual lifetimes (τ_1 and τ_2), and the corresponding amplitudes (A_1 and A_2) of exciton.

Br concentration (*y*)	**A_1**	**τ_1 (ns)**	**A_2**	**τ_2 (ns)**	**$\tau_{ave}^{Exciton}$(ns)**
0.00	0.95	0.15	0.05	1.44	0.58
0.20	0.97	0.15	0.03	1.88	0.59
0.42	0.82	0.20	0.18	2.90	2.25
0.58	0.74	0.46	0.26	4.54	3.61
0.75	0.35	1.00	0.65	5.80	5.39
0.84	0.41	2.90	0.59	7.81	6.79
1.00	0.57	3.95	0.43	7.80	6.24

Table A.11. Kinetic fitting parameters obtained using biexponential fitting for Mn-doped $CsPb(Cl_{1-y}Br_y)_3$ nanocrystals with x = 0.30 upon changing Br content y from 0−1.00 : average lifetimes (τ_{ave}), its individual lifetimes (τ_1 and τ_2), and the corresponding amplitudes (A_1 and A_2) of exciton and Mn emission, respectively.

Br concentration (*y*)	**A_1**	**τ_1 (ns)**	**A_2**	**τ_2 (ns)**	**$\tau_{ave}^{Exciton}$(ns)**
0.00	0.96	0.17	0.04	1.49	0.51
0.20	0.95	0.20	0.05	2.00	0.78
0.42	0.81	0.27	0.19	2.76	2.04
0.58	0.66	0.42	0.34	4.03	3.42
0.75	0.40	0.99	0.60	5.67	5.18
0.84	0.31	1.64	0.69	5.73	5.26
1.00	0.31	2.62	0.69	5.84	5.31
Br concentration (*y*)	**A_1**	**τ_1 (μs)**	**A_2**	**τ_2 (μs)**	**τ_{ave}^{Mn}(μs)**
0.00	0.22	1701	0.78	1772	1757
0.20	0.52	1071	0.48	1599	1377
0.42	0.61	815	0.39	1308	1062
0.58	0.68	230	0.32	881	648
0.75	0.64	240	0.36	659	496
0.84	0.63	60	0.37	263	206
1.00	0.93	8	0.07	70	31

Table A.12. Kinetic fitting parameters obtained using biexponential fitting for Mn−doped CsPb$(Cl_{1-y}Br_y)_3$ nanocrystals with x = 0.60 upon changing Br content y from 0−1.00 : average lifetimes (τ_{ave}), its individual lifetimes (τ_1 and τ_2), and the corresponding amplitudes (A_1 and A_2) of exciton and Mn emission, respectively.

Br concentration (y)	**A_1**	**τ_1 (ns)**	**A_2**	**τ_2 (ns)**	**$\tau_{ave}^{Exciton}$(ns)**
0.00	0.97	0.16	0.03	1.51	0.50
0.20	0.95	0.18	0.05	2.03	0.84
0.42	0.89	0.19	0.11	1.66	0.95
0.58	0.92	0.18	0.08	1.82	0.93
0.75	0.79	0.24	0.21	1.87	1.35
0.84	0.65	0.42	0.35	2.39	1.90
1.00	0.62	0.42	0.38	2.17	1.75
Br concentration (y)	**A_1**	**τ_1 (μs)**	**A_2**	**τ_2 (μs)**	**τ_{ave}^{Mn}(μs)**
0.00	0.19	435	0.81	1512	1445
0.20	0.21	667	0.79	1450	1363
0.42	0.25	536	0.75	1212	1123
0.58	0.26	530	0.74	1144	1059
0.75	0.29	447	0.71	883	807
0.84	0.30	319	0.70	657	599
1.00	0.66	39	0.34	270	219

REFERENCES

(1) Advanced Materials - 2021 - Liu - Perovskite Light-Emitting Diodes with EQE Exceeding 28 through a Synergetic.Pdf. Lin,K; Xing, J.; Quan, L. N.; Arquer, F. P.; Gong, X.; Lu, J.; Xie, L.; Zhao, W.; Zhang, D.; Yan, C.; Li, W.; Liu, X.; Lu, Y.; Kirman, K.; Sargent, E. H.; Xiong, Q.; Wei, Z.;

(2) Chen, H. Y.; Maiti, S.; Son, D. H. Doping Location-Dependent Energy Transfer Dynamics in Mn-Doped CdS/ZnS Nanocrystals. *ACS Nano* **2012**, *6* (1). https://doi.org/10.1021/nn204452e.

(3) Akkerman, Q. A.; Rainò, G.; Kovalenko, M. V.; Manna, L. Genesis, Challenges and Opportunities for Colloidal Lead Halide Perovskite Nanocrystals. *Nat Mater* **2018**, *17* (5), 394–405. https://doi.org/10.1038/s41563-018-0018-4.

(4) Protesescu, L.; Yakunin, S.; Bodnarchuk, M. I.; Krieg, F.; Caputo, R.; Hendon, C. H.; Yang, R. X.; Walsh, A.; Kovalenko, M. V. Nanocrystals of Cesium Lead Halide Perovskites (CsPbX<inf>3</Inf>, X = Cl, Br, and I): *Nano Lett* **2015**, *15* (6), 3692–3696.

(5) Akkerman, Q. A.; Motti, S. G.; Srimath Kandada, A. R.; Mosconi, E.; D'Innocenzo, V.; Bertoni, G.; Marras, S.; Kamino, B. A.; Miranda, L.; De Angelis, F.; Petrozza, A.; Prato, M.; Manna, L. Solution Synthesis Approach to Colloidal Cesium Lead Halide Perovskite Nanoplatelets with Monolayer-Level Thickness Control. *J Am Chem Soc* **2016**, *138* (3), 1010–1016. https://doi.org/10.1021/jacs.5b12124.

(6) Cho, J.; Banerjee, S. Ligand-Directed Stabilization of Ternary Phases: Synthetic Control of Structural Dimensionality in Solution-Grown Cesium Lead Bromide Nanocrystals. *Chemistry of Materials* **2018**, *30* (17), 6144–6155. https://doi.org/10.1021/acs.chemmater.8b02730.

(7) Akkerman, Q. A.; D'Innocenzo, V.; Accornero, S.; Scarpellini, A.; Petrozza, A.; Prato, M.; Manna, L. Tuning the Optical Properties of Cesium Lead Halide Perovskite Nanocrystals by Anion Exchange Reactions. *J Am Chem Soc* **2015**, *137* (32), 10276–10281. https://doi.org/10.1021/jacs.5b05602.

(8) Zhang, W.; Eperon, G. E.; Snaith, H. J. Metal Halide Perovskites for Energy Applications. *Nat Energy* **2016**, *1* (6). https://doi.org/10.1038/nenergy.2016.48.

(9) Manser, J. S.; Christians, J. A.; Kamat, P. V. Intriguing Optoelectronic Properties of Metal Halide Perovskites. *Chem Rev* **2016**, *116* (21), 12956–13008. https://doi.org/10.1021/acs.chemrev.6b00136.

(10) Zhou, Y.; Yong, Z. J.; Zhang, W.; Ma, J. P.; Sadhanala, A.; Chen, Y. M.; Liu, B. M.; Zhou, Y.; Song, B.; Sun, H. T. Ultra-Broadband Optical Amplification at Telecommunication Wavelengths Achieved by Bismuth-Activated Lead Iodide Perovskites. *J Mater Chem C Mater* **2017**, *5* (10). https://doi.org/10.1039/c6tc05539g.

(11) Li, Y.; Lu, Y.; Huo, X.; Wei, D.; Meng, J.; Dong, J.; Qiao, B.; Zhao, S.; Xu, Z.; Song, D. Bandgap Tuning Strategy by Cations and Halide Ions of Lead Halide Perovskites Learned from Machine Learning. *RSC Adv* **2021**, *11* (26), 15688–15694. https://doi.org/10.1039/d1ra03117a.

(12) Akkerman, Q. A.; Rainò, G.; Kovalenko, M. V.; Manna, L. Genesis, Challenges and Opportunities for Colloidal Lead Halide Perovskite Nanocrystals. *Nat Mater* **2018**, *17* (5), 394–405. https://doi.org/10.1038/s41563-018-0018-4.

(13) Protesescu, L.; Yakunin, S.; Bodnarchuk, M. I.; Krieg, F.; Caputo, R.; Hendon, C. H.; Yang, R. X.; Walsh, A.; Kovalenko, M. V. Nanocrystals of Cesium Lead Halide Perovskites (CsPbX<inf>3</Inf>, X = Cl, Br, and I): *Nano Lett* **2015**, *15* (6), 3692–3696.

(14) Akkerman, Q. A.; Motti, S. G.; Srimath Kandada, A. R.; Mosconi, E.; D'Innocenzo, V.; Bertoni, G.; Marras, S.; Kamino, B. A.; Miranda, L.; De Angelis, F.; Petrozza, A.; Prato, M.; Manna, L. Solution Synthesis Approach to Colloidal Cesium Lead Halide Perovskite Nanoplatelets with Monolayer-Level Thickness Control. *J Am Chem Soc* **2016**, *138* (3), 1010–1016. https://doi.org/10.1021/jacs.5b12124.

(15) Cho, J.; Banerjee, S. Ligand-Directed Stabilization of Ternary Phases: Synthetic Control of Structural Dimensionality in Solution-Grown Cesium Lead Bromide Nanocrystals. *Chemistry of Materials* **2018**, *30* (17), 6144–6155. https://doi.org/10.1021/acs.chemmater.8b02730.

(16) Hintermayr, V. A.; Richter, A. F.; Ehrat, F.; Döblinger, M.; Vanderlinden, W.; Sichert, J. A.; Tong, Y.; Polavarapu, L.; Feldmann, J.; Urban, A. S. Tuning the Optical Properties of Perovskite Nanoplatelets through Composition and Thickness by Ligand-Assisted Exfoliation. *Advanced Materials* **2016**, *28* (43), 9478–9485.

https://doi.org/10.1002/adma.201602897.

(17) Zhang, W.; Eperon, G. E.; Snaith, H. J. Metal Halide Perovskites for Energy Applications. *Nat Energy* **2016**, *1* (6). https://doi.org/10.1038/nenergy.2016.48.

(18) Kong, L.; Zhang, X.; Zhang, C.; Wang, L.; Wang, S.; Cao, F.; Zhao, D.; Rogach, A. L.; Yang, X. Stability of Perovskite Light-Emitting Diodes: Existing Issues and Mitigation Strategies Related to Both Material and Device Aspects. *Advanced Materials*. 2022. https://doi.org/10.1002/adma.202205217.

(19) Lin, K.; Xing, J.; Quan, L. N.; de Arquer, F. P. G.; Gong, X.; Lu, J.; Xie, L.; Zhao, W.; Zhang, D.; Yan, C.; Li, W.; Liu, X.; Lu, Y.; Kirman, J.; Sargent, E. H.; Xiong, Q.; Wei, Z. Perovskite Light-Emitting Diodes with External Quantum Efficiency Exceeding 20 per Cent. *Nature* **2018**, *562* (7726), 245–248. https://doi.org/10.1038/s41586-018-0575-3.

(20) Liu, Y.; Li, Z.; Xu, J.; Dong, Y.; Chen, B.; Park, S. M.; Ma, D.; Lee, S.; Huang, J. E.; Teale, S.; Voznyy, O.; Sargent, E. H. Wide-Bandgap Perovskite Quantum Dots in Perovskite Matrix for Sky-Blue Light-Emitting Diodes. *J Am Chem Soc* **2022**, *144* (9), 4009–4016. https://doi.org/10.1021/jacs.1c12556.

(21) Gangishetty, M. K.; Sanders, S. N.; Congreve, D. N. Mn2+ Doping Enhances the Brightness, Efficiency, and Stability of Bulk Perovskite Light-Emitting Diodes. *ACS Photonics* **2019**, *6* (5), 1111–1117. https://doi.org/10.1021/acsphotonics.9b00142.

(22) Wang, Y. K.; Singh, K.; Li, J. Y.; Dong, Y.; Wang, X. Q.; Pina, J. M.; Yu, Y. J.; Sabatini, R.; Liu, Y.; Ma, D.; Liu, J.; Liu, Z.; Gao, Y.; Voznyy, O.; Ma, W.; Fung, M. K.; Liao, L. S.; Sargent, E. H. In Situ Inorganic Ligand Replenishment Enables Bandgap Stability in Mixed-Halide Perovskite Quantum Dot Solids. *Advanced Materials* **2022**, *34* (21). https://doi.org/10.1002/adma.202200854.

(23) Liu, Z.; Qiu, W.; Peng, X.; Sun, G.; Liu, X.; Liu, D.; Li, Z.; He, F.; Shen, C.; Gu, Q.; Ma, F.; Yip, H. L.; Hou, L.; Qi, Z.; Su, S. J. Perovskite Light-Emitting Diodes with EQE Exceeding 28% through a Synergetic Dual-Additive Strategy for Defect Passivation and Nanostructure Regulation. *Advanced Materials* **2021**, *33* (43). https://doi.org/10.1002/adma.202103268.

(24) Liu, Y.; Li, Z.; Xu, J.; Dong, Y.; Chen, B.; Park, S. M.; Ma, D.; Lee, S.; Huang, J. E.; Teale, S.; Voznyy, O.; Sargent, E. H. Wide-Bandgap Perovskite Quantum Dots in Perovskite Matrix for Sky-Blue Light-Emitting Diodes. *J Am Chem Soc* **2022**, *144*

(9), 4009–4016. https://doi.org/10.1021/jacs.1c12556.

(25) Wang, Q.; Zhang, X.; Jin, Z.; Zhang, J.; Gao, Z.; Li, Y.; Liu, S. F. Energy-Down-Shift CsPbCl3:Mn Quantum Dots for Boosting the Efficiency and Stability of Perovskite Solar Cells. *ACS Energy Lett* **2017**, *2* (7). https://doi.org/10.1021/acsenergylett.7b00375.

(26) Meinardi, F.; Akkerman, Q. A.; Bruni, F.; Park, S.; Mauri, M.; Dang, Z.; Manna, L.; Brovelli, S. Doped Halide Perovskite Nanocrystals for Reabsorption-Free Luminescent Solar Concentrators. *ACS Energy Lett* **2017**, *2* (10). https://doi.org/10.1021/acsenergylett.7b00701.

(27) Jeon, N. J.; Na, H.; Jung, E. H.; Yang, T. Y.; Lee, Y. G.; Kim, G.; Shin, H. W.; Il Seok, S.; Lee, J.; Seo, J. A Fluorene-Terminated Hole-Transporting Material for Highly Efficient and Stable Perovskite Solar Cells. *Nat Energy* **2018**, *3* (8). https://doi.org/10.1038/s41560-018-0200-6.

(28) Wang, R.; Mujahid, M.; Duan, Y.; Wang, Z. K.; Xue, J.; Yang, Y. A Review of Perovskites Solar Cell Stability. *Advanced Functional Materials*. 2019. https://doi.org/10.1002/adfm.201808843.

(29) Bhalla, A. S.; Guo, R.; Roy, R. The Perovskite Structure - A Review of Its Role in Ceramic Science and Technology. *Materials Research Innovations*. 2000. https://doi.org/10.1007/s100190000062.

(30) Glazer, A. M. Simple Ways of Determining Perovskite Structures. *Acta Crystallographica Section A* **1975**, *31* (6). https://doi.org/10.1107/S0567739475001635.

(31) Tilley, R. J. D. *Perovskites: Structure-Property Relationships*; 2016. https://doi.org/10.1002/9781118935651.

(32) Dong, H.; Zhang, C.; Liu, X.; Yao, J.; Zhao, Y. S. Materials Chemistry and Engineering in Metal Halide Perovskite Lasers. *Chemical Society Reviews*. 2020. https://doi.org/10.1039/c9cs00598f.

(33) Fu, Y.; Zhu, H.; Chen, J.; Hautzinger, M. P.; Zhu, X. Y.; Jin, S. Metal Halide Perovskite Nanostructures for Optoelectronic Applications and the Study of Physical Properties. *Nature Reviews Materials*. 2019. https://doi.org/10.1038/s41578-019-0080-9.

(34) Lüssem, B.; Riede, M.; Leo, K. Doping of Organic Semiconductors. *Physica Status Solidi (A) Applications and Materials Science*. 2013. https://doi.org/10.1002/pssa.201228310.

(35) Mir, W. J.; Jagadeeswararao, M.; Das, S.; Nag, A. Colloidal Mn-Doped Cesium Lead Halide Perovskite Nanoplatelets. *ACS Energy Lett* **2017**, *2* (3), 537–543. https://doi.org/10.1021/acsenergylett.6b00741.

(36) Dutta, S. K.; Dutta, A.; Das Adhikari, S.; Pradhan, N. Doping Mn 2+ in Single-Crystalline Layered Perovskite Microcrystals. *ACS Energy Lett* **2019**, *4* (1), 343–351. https://doi.org/10.1021/acsenergylett.8b02349.

(37) Dong, Y.; Parobek, D.; Son, D. H. Controlling Quantum Confinement and Magnetic Doping of Cesium Lead Halide Perovskite Nanocrystals. *Journal of the Korean Ceramic Society* **2018**, *55* (6), 515–526. https://doi.org/10.4191/kcers.2018.55.6.11.

(38) Xu, K.; Vickers, E. T.; Luo, B.; Allen, A. C.; Chen, E.; Roseman, G.; Wang, Q.; Kliger, D. S.; Millhauser, G. L.; Yang, W.; Li, X.; Zhang, J. Z. First Synthesis of Mn-Doped Cesium Lead Bromide Perovskite Magic Sized Clusters at Room Temperature. *Journal of Physical Chemistry Letters* **2020**, *11* (3), 1162–1169. https://doi.org/10.1021/acs.jpclett.9b03700.

(39) Guria, A. K.; Dutta, S. K.; Adhikari, S. Das; Pradhan, N. Doping Mn2+ in Lead Halide Perovskite Nanocrystals: Successes and Challenges. *ACS Energy Lett* **2017**, *2* (5), 1014–1021. https://doi.org/10.1021/acsenergylett.7b00177.

(40) Duong, T.; Mulmudi, H. K.; Shen, H.; Wu, Y. L.; Barugkin, C.; Mayon, Y. O.; Nguyen, H. T.; Macdonald, D.; Peng, J.; Lockrey, M.; Li, W.; Cheng, Y. B.; White, T. P.; Weber, K.; Catchpole, K. Structural Engineering Using Rubidium Iodide as a Dopant under Excess Lead Iodide Conditions for High Efficiency and Stable Perovskites. *Nano Energy* **2016**, *30*. https://doi.org/10.1016/j.nanoen.2016.10.027.

(41) Zhao, W.; Yao, Z.; Yu, F.; Yang, D.; Liu, S. F. Alkali Metal Doping for Improved CH3NH3PbI3 Perovskite Solar Cells. *Advanced Science* **2018**, *5* (2). https://doi.org/10.1002/advs.201700131.

(42) Saliba, M.; Matsui, T.; Domanski, K.; Seo, J. Y.; Ummadisingu, A.; Zakeeruddin, S. M.; Correa-Baena, J. P.; Tress, W. R.; Abate, A.; Hagfeldt, A.; Grätzel, M. Incorporation of Rubidium Cations into Perovskite Solar Cells Improves Photovoltaic Performance. *Science (1979)* **2016**, *354* (6309).

https://doi.org/10.1126/science.aah5557.

(43) Begum, R.; Parida, M. R.; Abdelhady, A. L.; Murali, B.; Alyami, N. M.; Ahmed, G. H.; Hedhili, M. N.; Bakr, O. M.; Mohammed, O. F. Engineering Interfacial Charge Transfer in CsPbBr3 Perovskite Nanocrystals by Heterovalent Doping. *J Am Chem Soc* **2017**, *139* (2). https://doi.org/10.1021/jacs.6b09575.

(44) Zhou, Y.; Yong, Z. J.; Zhang, K. C.; Liu, B. M.; Wang, Z. W.; Hou, J. S.; Fang, Y. Z.; Zhou, Y.; Sun, H. T.; Song, B. Ultrabroad Photoluminescence and Electroluminescence at New Wavelengths from Doped Organometal Halide Perovskites. *Journal of Physical Chemistry Letters* **2016**, *7* (14). https://doi.org/10.1021/acs.jpclett.6b01147.

(45) Liu, W.; Lin, Q.; Li, H.; Wu, K.; Robel, I.; Pietryga, J. M.; Klimov, V. I. Mn2+-Doped Lead Halide Perovskite Nanocrystals with Dual-Color Emission Controlled by Halide Content. *J Am Chem Soc* **2016**, *138* (45), 14954–14961. https://doi.org/10.1021/jacs.6b08085.

(46) Parobek, D.; Roman, B. J.; Dong, Y.; Jin, H.; Lee, E.; Sheldon, M.; Son, D. H. Exciton-to-Dopant Energy Transfer in Mn-Doped Cesium Lead Halide Perovskite Nanocrystals. *Nano Lett* **2016**, *16* (12), 7376–7380. https://doi.org/10.1021/acs.nanolett.6b02772.

(47) Tang, Z.; Bessho, T.; Awai, F.; Kinoshita, T.; Maitani, M. M.; Jono, R.; Murakami, T. N.; Wang, H.; Kubo, T.; Uchida, S.; Segawa, H. Hysteresis-Free Perovskite Solar Cells Made of Potassium-Doped Organometal Halide Perovskite. *Sci Rep* **2017**, *7* (1). https://doi.org/10.1038/s41598-017-12436-x.

(48) Dutta, S. K.; Dutta, A.; Das Adhikari, S.; Pradhan, N. Doping Mn 2+ in Single-Crystalline Layered Perovskite Microcrystals. *ACS Energy Lett* **2019**, *4* (1), 343–351. https://doi.org/10.1021/acsenergylett.8b02349.

(49) Gilkes, R. J.; McKenzie, R. M. Geochemistry and Mineralogy of Manganese in Soils. In *Manganese in Soils and Plants*; 1988. https://doi.org/10.1007/978-94-009-2817-6_3.

(50) Acharya, S.; Sarma, D. D.; Jana, N. R.; Pradhan, N. An Alternate Route to High-Quality ZnSe and Mn-Doped ZnSe Nanocrystals. *Journal of Physical Chemistry Letters* **2010**, *1* (2). https://doi.org/10.1021/jz900291a.

(51) Chábera, P.; Lindh, L.; Rosemann, N. W.; Prakash, O.; Uhlig, J.; Yartsev, A.; Wärnmark, K.; Sundström, V.; Persson, P. Photofunctionality of Iron(III) N-Heterocyclic Carbenes and Related D5 Transition Metal Complexes. *Coordination Chemistry Reviews*. 2021. https://doi.org/10.1016/j.ccr.2020.213517.

(52) Su, B.; Zhou, G.; Huang, J.; Song, E.; Nag, A.; Xia, Z. Mn2+-Doped Metal Halide Perovskites: Structure, Photoluminescence, and Application. *Laser Photon Rev* **2021**, *15* (1), 1–29. https://doi.org/10.1002/lpor.202000334.

(53) Ferguson, J.; Guggenheim, H. J.; Tanabe, Y. The Effects of Exchange Interactions in the Spectra of Octahedral Manganese. II. Compounds. *J Physical Soc Japan* **1966**, *21* (4). https://doi.org/10.1143/JPSJ.21.692.

(54) Palumbo, D. T.; Brown, J. J. Electronic States of Mn2+-Activated Phosphors. *J Electrochem Soc* **1970**, *117* (9). https://doi.org/10.1149/1.2407765.

(55) Lanver, U.; Lehmann, G. Luminescence Spectra of Mn(II) in Different Symmetries. *J Lumin* **1978**, *17* (2). https://doi.org/10.1016/0022-2313(78)90088-1.

(56) Kamran, M. A.; Liu, R.; Shi, L. J.; Li, Z. A.; Marzi, T.; Schöppner, C.; Farle, M.; Zou, B. Tunable Emission Properties by Ferromagnetic Coupling Mn(II) Aggregates in Mn-Doped CdS Microbelts/Nanowires. *Nanotechnology* **2014**, *25* (38). https://doi.org/10.1088/0957-4484/25/38/385201.

(57) Ozarowski, A.; McGarvey, B. R.; Sarkar, A. B.; Drake, J. E. EPR Study of Manganese(II) in Two Crystalline Forms of Fe(C6H8N2S2)2(NCS)2 and the High-Spin-Low-Spin Transition That Occurs in Only One Form. X-Ray Structure Determination of Both Forms. *Inorg Chem* **1988**, *27* (4). https://doi.org/10.1021/ic00277a012.

(58) Vink, A. P.; de Bruin, M. A.; Roke, S.; Peijzel, P. S.; Meijerink, A. Luminescence of Exchange Coupled Pairs of Transition Metal Ions. *J Electrochem Soc* **2001**, *148* (7). https://doi.org/10.1149/1.1375169.

(59) Fainblat, R.; Barrows, C. J.; Hopmann, E.; Siebeneicher, S.; Vlaskin, V. A.; Gamelin, D. R.; Bacher, G. Giant Excitonic Exchange Splittings at Zero Field in Single Colloidal CdSe Quantum Dots Doped with Individual Mn2+ Impurities. *Nano Lett* **2016**, *16* (10). https://doi.org/10.1021/acs.nanolett.6b02775.

(60) Barrows, C. J.; Vlaskin, V. A.; Gamelin, D. R. Absorption and Magnetic Circular Dichroism Analyses of Giant Zeeman Splittings in Diffusion-Doped Colloidal Cd1-

XMnxSe Quantum Dots. *Journal of Physical Chemistry Letters* **2015**, *6* (15). https://doi.org/10.1021/acs.jpclett.5b01137.

(61) Beaulac, R.; Archer, P. I.; Ochsenbein, S. T.; Gamelin, D. R. Mn2+-Doped CdSe Quantum Dots: New Inorganic Materials for Spin-Electronics and Spin-Photonics. *Adv Funct Mater* **2008**, *18* (24). https://doi.org/10.1002/adfm.200801016.

(62) Rice, W. D.; Liu, W.; Pinchetti, V.; Yakovlev, D. R.; Klimov, V. I.; Crooker, S. A. Direct Measurements of Magnetic Polarons in Cd1-XMnxSe Nanocrystals from Resonant Photoluminescence. *Nano Lett* **2017**, *17* (5). https://doi.org/10.1021/acs.nanolett.7b00421.

(63) Pradeep, K. R.; Viswanatha, R. Mechanism of Mn Emission: Energy Transfer vs Charge Transfer Dynamics in Mn-Doped Quantum Dots. *APL Mater* **2020**, *8* (2). https://doi.org/10.1063/1.5140888.

(64) Gahlot, K.; Pradeep, K.; Camellini, A.; Sirigu, G.; Cerullo, G.; Zavelani-Rossi, M.; Singh, A.; Waghmare, U. V.; Viswanatha, R. Transient Species Mediating Energy Transfer to Spin-Forbidden Mn d States in II-VI Semiconductor Quantum Dots. *ACS Energy Lett* **2019**, *4* (3). https://doi.org/10.1021/acsenergylett.9b00064.

(65) Rossi, D.; Parobek, D.; Dong, Y.; Son, D. H. Dynamics of Exciton-Mn Energy Transfer in Mn-Doped CsPbCl3 Perovskite Nanocrystals. *Journal of Physical Chemistry C* **2017**, *121* (32), 17143–17149. https://doi.org/10.1021/acs.jpcc.7b06182.

(66) Sapra, S.; Prakash, A.; Ghangrekar, A.; Periasamy, N.; Sarma, D. D. Emission Properties of Manganese-Doped ZnS Nanocrystals. *Journal of Physical Chemistry B* **2005**, *109* (5). https://doi.org/10.1021/jp049976e.

(67) Chen, W.; Malm, J. O.; Zwiller, V.; Wallenberg, R.; Bovin, J. O. Size Dependence of Eu2+ Fluorescence in ZnS:Eu2+ Nanoparticles. *J Appl Phys* **2001**, *89* (5). https://doi.org/10.1063/1.1344582.

(68) Huang, H.; Lin, H.; Kershaw, S. V.; Susha, A. S.; Choy, W. C. H.; Rogach, A. L. Polyhedral Oligomeric Silsesquioxane Enhances the Brightness of Perovskite Nanocrystal-Based Green Light-Emitting Devices. *Journal of Physical Chemistry Letters* **2016**, *7* (21). https://doi.org/10.1021/acs.jpclett.6b02224.

(69) Tirmzi, A. M.; Dwyer, R. P.; Hanrath, T.; Marohn, J. A. Coupled Slow and Fast Charge Dynamics in Cesium Lead Bromide Perovskite. *ACS Energy Lett* **2017**, *2* (2).

https://doi.org/10.1021/acsenergylett.6b00722.

(70) Arora, N.; Orlandi, S.; Dar, M. I.; Aghazada, S.; Jacopin, G.; Cavazzini, M.; Mosconi, E.; Gratia, P.; De Angelis, F.; Pozzi, G.; Graetzel, M.; Nazeeruddin, M. K. High Open-Circuit Voltage: Fabrication of Formamidinium Lead Bromide Perovskite Solar Cells Using Fluorene-Dithiophene Derivatives as Hole-Transporting Materials. *ACS Energy Lett* **2016**, *1* (1). https://doi.org/10.1021/acsenergylett.6b00077.

(71) Nair, V. C.; Muthu, C.; Rogach, A. L.; Kohara, R.; Biju, V. Channeling Exciton Migration into Electron Transfer in Formamidinium Lead Bromide Perovskite Nanocrystal/Fullerene Composites. *Angewandte Chemie - International Edition* **2017**, *56* (5). https://doi.org/10.1002/anie.201610070.

(72) Draguta, S.; Thakur, S.; Morozov, Y. V.; Wang, Y.; Manser, J. S.; Kamat, P. V.; Kuno, M. Spatially Non-Uniform Trap State Densities in Solution-Processed Hybrid Perovskite Thin Films. *Journal of Physical Chemistry Letters* **2016**, *7* (4). https://doi.org/10.1021/acs.jpclett.5b02888.

(73) Wang, S.; Leng, J.; Yin, Y.; Liu, J.; Wu, K.; Jin, S. Ultrafast Dopant-Induced Exciton Auger-like Recombination in Mn-Doped Perovskite Nanocrystals. *ACS Energy Lett* **2020**, *5*, 328–334. https://doi.org/10.1021/acsenergylett.9b02678.

(74) Richter, A.; Glunz, S. W.; Werner, F.; Schmidt, J.; Cuevas, A. Improved Quantitative Description of Auger Recombination in Crystalline Silicon. *Phys Rev B Condens Matter Mater Phys* **2012**, *86* (16). https://doi.org/10.1103/PhysRevB.86.165202.

(75) De, A.; Mondal, N.; Samanta, A. Luminescence Tuning and Exciton Dynamics of Mn-Doped CsPbCl3 Nanocrystals. *Nanoscale* **2017**, *9* (43), 16722–16727. https://doi.org/10.1039/c7nr06745c.

(76) Xu, K.; Vliem, J. F.; Meijerink, A. Long-Lived Dark Exciton Emission in Mn-Doped CsPbCl 3 Perovskite Nanocrystals. *Journal of Physical Chemistry C* **2019**, *123* (1), 979–984. https://doi.org/10.1021/acs.jpcc.8b12035.

(77) Qiao, T.; Liu, X.; Rossi, D.; Khurana, M.; Lin, Y.; Wen, J.; Cheon, J.; Akimov, A. V.; Son, D. H. Magnetic Effect of Dopants on Bright and Dark Excitons in Strongly Confined Mn-Doped CsPbI3Quantum Dots. *Nano Lett* **2021**, *21* (22), 9543–9550. https://doi.org/10.1021/acs.nanolett.1c03114.

(78) Janiesch, C.; Zschech, P.; Heinrich, K. Machine Learning and Deep Learning.

Electronic Markets **2021**, *31* (3). https://doi.org/10.1007/s12525-021-00475-2.

(79) Turcani, L.; Greenaway, R. L.; Jelfs, K. E. Machine Learning for Organic Cage Property Prediction. *Chemistry of Materials* **2019**, *31* (3), 714–727. https://doi.org/10.1021/acs.chemmater.8b03572.

(80) Juneja, R.; Yumnam, G.; Satsangi, S.; Singh, A. K. Coupling the High-Throughput Property Map to Machine Learning for Predicting Lattice Thermal Conductivity. *Chemistry of Materials* **2019**, *31* (14), 5145–5151. https://doi.org/10.1021/acs.chemmater.9b01046.

(81) Rajan, A. C.; Mishra, A.; Satsangi, S.; Vaish, R.; Mizuseki, H.; Lee, K. R.; Singh, A. K. Machine-Learning-Assisted Accurate Band Gap Predictions of Functionalized Mxene. *Chemistry of Materials* **2018**, *30* (12), 4031–4038. https://doi.org/10.1021/acs.chemmater.8b00686.

(82) Wei, J.; Chu, X.; Sun, X. Y.; Xu, K.; Deng, H. X.; Chen, J.; Wei, Z.; Lei, M. Machine Learning in Materials Science. *InfoMat*. 2019. https://doi.org/10.1002/inf2.12028.

(83) Jha, D.; Ward, L.; Paul, A.; Liao, W. keng; Choudhary, A.; Wolverton, C.; Agrawal, A. ElemNet: Deep Learning the Chemistry of Materials From Only Elemental Composition. *Sci Rep* **2018**, *8* (1). https://doi.org/10.1038/s41598-018-35934-y.

(84) Butler, K. T.; Davies, D. W.; Cartwright, H.; Isayev, O.; Walsh, A. Machine Learning for Molecular and Materials Science. *Nature*. 2018. https://doi.org/10.1038/s41586-018-0337-2.

(85) Nasteski, V. An Overview of the Supervised Machine Learning Methods. *HORIZONS.B* **2017**, *4*. https://doi.org/10.20544/horizons.b.04.1.17.p05.

(86) Dy, J. G.; Brodley, C. E. Feature Selection for Unsupervised Learning. *Journal of Machine Learning Research* **2004**, *5*. https://doi.org/10.1007/springerreference_302701.

(87) Liu, W.; Lin, Q.; Li, H.; Wu, K.; Robel, I.; Pietryga, J. M.; Klimov, V. I. Mn2+-Doped Lead Halide Perovskite Nanocrystals with Dual-Color Emission Controlled by Halide Content. *J Am Chem Soc* **2016**, *138* (45), 14954–14961. https://doi.org/10.1021/jacs.6b08085.

(88) Puthenpurayil, J.; Cheng, O. H. C.; Qiao, T.; Rossi, D.; Son, D. H. On the Determination of Absorption Cross Section of Colloidal Lead Halide Perovskite

Quantum Dots. *Journal of Chemical Physics* **2019**, *151* (15). https://doi.org/10.1063/1.5126039.

(89) Ravi, V. K.; Markad, G. B.; Nag, A. Band Edge Energies and Excitonic Transition Probabilities of Colloidal CsPbX3 (X = Cl, Br, I) Perovskite Nanocrystals. *ACS Energy Lett* **2016**, *1* (4), 665–671. https://doi.org/10.1021/acsenergylett.6b00337.

(90) Ravi, V. K.; Scheidt, R. A.; Nag, A.; Kuno, M.; Kamat, P. V. To Exchange or Not to Exchange. Suppressing Anion Exchange in Cesium Lead Halide Perovskites with PbSO4-Oleate Capping. *ACS Energy Lett* **2018**, *3* (4), 1049–1055. https://doi.org/10.1021/acsenergylett.8b00380.

(91) Li, Z. J.; Hofman, E.; Davis, A. H.; Khammang, A.; Wright, J. T.; Dzikovski, B.; Meulenberg, R. W.; Zheng, W. Complete Dopant Substitution by Spinodal Decomposition in Mn-Doped Two-Dimensional CsPbCl3 Nanoplatelets. *Chemistry of Materials* **2018**, *30* (18), 6400–6409. https://doi.org/10.1021/acs.chemmater.8b02657.

(92) Rossi, D.; Parobek, D.; Dong, Y.; Son, D. H. Dynamics of Exciton-Mn Energy Transfer in Mn-Doped CsPbCl3 Perovskite Nanocrystals. *Journal of Physical Chemistry C* **2017**, *121* (32), 17143–17149. https://doi.org/10.1021/acs.jpcc.7b06182.

(93) Cai, T.; Wang, J.; Li, W.; Hills-Kimball, K.; Yang, H.; Nagaoka, Y.; Yuan, Y.; Zia, R.; Chen, O. Mn2+/Yb3+ Codoped CsPbCl3 Perovskite Nanocrystals with Triple-Wavelength Emission for Luminescent Solar Concentrators. *Advanced Science* **2020**, *7* (18), 1–9. https://doi.org/10.1002/advs.202001317.

(94) Chakraborty, R.; Maiti, A.; Ghorai, U. K.; Pal, A. J. Defect Passivation of Mn2+-Doped CsPbCl3Perovskite Nanocrystals as Probed by Scanning Tunneling Spectroscopy: Toward Boosting Emission Efficiencies. *ACS Appl Nano Mater* **2021**, *4* (10), 10155–10163. https://doi.org/10.1021/acsanm.1c01623.

(95) Guan, L. Q.; Shi, S.; Niu, X. W.; Guo, S. C.; Zhao, J.; Ji, T. M.; Dong, H.; Jia, F. Y.; Xiao, J. W.; Sun, L. D.; Yan, C. H. All-Inorganic Manganese-Based CsMnCl3 Nanocrystals for X-Ray Imaging. *Advanced Science* **2022**, *9* (18), 1–7. https://doi.org/10.1002/advs.202201354.

(96) Xu, K.; Vliem, J. F.; Meijerink, A. Long-Lived Dark Exciton Emission in Mn-Doped CsPbCl 3 Perovskite Nanocrystals. *Journal of Physical Chemistry C* **2019**, *123* (1), 979–984. https://doi.org/10.1021/acs.jpcc.8b12035.

(97) Cortecchia, D.; Mróz, W.; Neutzner, S.; Borzda, T.; Folpini, G.; Brescia, R.; Petrozza, A. Defect Engineering in 2D Perovskite by Mn(II) Doping for Light-Emitting Applications. *Chem* **2019**, *5* (8), 2146–2158. https://doi.org/10.1016/j.chempr.2019.05.018.

(98) Guria, A. K.; Dutta, S. K.; Adhikari, S. Das; Pradhan, N. Doping Mn2+ in Lead Halide Perovskite Nanocrystals: Successes and Challenges. *ACS Energy Lett* **2017**, *2* (5), 1014–1021. https://doi.org/10.1021/acsenergylett.7b00177.

(99) Chen, W.; Sammynaiken, R.; Huang, Y.; Malm, J. O.; Wallenberg, R.; Bovin, J. O.; Zwiller, V.; Kotov, N. A. Crystal Field, Phonon Coupling and Emission Shift of Mn2+ in ZnS:Mn Nanoparticles. *J Appl Phys* **2001**, *89* (2), 1120–1129. https://doi.org/10.1063/1.1332795.

(100) Pradhan, N.; Peng, X. Efficient and Color-Tunable Mn-Doped ZnSe Nanocrystal Emitters: Control of Optical Performance via Greener Synthetic Chemistry. *J Am Chem Soc* **2007**, *129* (11), 3339–3347. https://doi.org/10.1021/ja068360v.

(101) Bradshaw, L. R.; May, J. W.; Dempsey, J. L.; Li, X.; Gamelin, D. R. Ferromagnetic Excited-State Mn 2 + Dimers in Zn 1 - X Mn x Se Quantum Dots Observed by Time-Resolved Magnetophotoluminescence. *Phys Rev B Condens Matter Mater Phys* **2014**, *89* (11), 1–11. https://doi.org/10.1103/PhysRevB.89.115312.

(102) Ha, S. K.; Shcherbakov-Wu, W.; Powers, E. R.; Paritmongkol, W.; Tisdale, W. A. Power-Dependent Photoluminescence Efficiency in Manganese-Doped 2D Hybrid Perovskite Nanoplatelets. *ACS Nano* **2021**, *15* (12), 20527–20538. https://doi.org/10.1021/acsnano.1c09103.

(103) Chen, H.; Maiti, S.; Son, D. H. Doping Location-Dependent Energy Transfer Dynamics in Mn-Doped. *American Chemical Society* **2012**, *6* (1), 583–591.

(104) Dang, Z.; Shamsi, J.; Palazon, F.; Imran, M.; Akkerman, Q. A.; Park, S.; Bertoni, G.; Prato, M.; Brescia, R.; Manna, L. In Situ Transmission Electron Microscopy Study of Electron Beam-Induced Transformations in Colloidal Cesium Lead Halide Perovskite Nanocrystals. *ACS Nano* **2017**, *11* (2), 2124–2132. https://doi.org/10.1021/acsnano.6b08324.

(105) Cho, J.; Choi, Y. H.; O'Loughlin, T. E.; De Jesus, L.; Banerjee, S. Ligand-Mediated Modulation of Layer Thicknesses of Perovskite Methylammonium Lead Bromide Nanoplatelets. *Chemistry of Materials* **2016**, *28* (19), 6909–6916.

https://doi.org/10.1021/acs.chemmater.6b02241.

(106) Zou, S.; Liu, Y.; Li, J.; Liu, C.; Feng, R.; Jiang, F.; Li, Y.; Song, J.; Zeng, H.; Hong, M.; Chen, X. Stabilizing Cesium Lead Halide Perovskite Lattice through Mn(II) Substitution for Air-Stable Light-Emitting Diodes. *J Am Chem Soc* **2017**, *139* (33), 11443–11450. https://doi.org/10.1021/jacs.7b04000.

(107) Wang, W.; Li, J.; Duan, G.; Zhou, H.; Lu, Y.; Yan, T.; Cao, B.; Liu, Z. Study on the Mn-Doped CsPbCl3 Perovskite Nanocrystals with Controllable Dual-Color Emission via Energy Transfer. *J Alloys Compd* **2020**, *821*, 153568. https://doi.org/10.1016/j.jallcom.2019.153568.

(108) Yuan, X.; Ji, S.; De Siena, M. C.; Fei, L.; Zhao, Z.; Wang, Y.; Li, H.; Zhao, J.; Gamelin, D. R. Photoluminescence Temperature Dependence, Dynamics, and Quantum Efficiencies in Mn2+-Doped CsPbCl3 Perovskite Nanocrystals with Varied Dopant Concentration. *Chemistry of Materials* **2017**, *29* (18), 8003–8011. https://doi.org/10.1021/acs.chemmater.7b03311.

(109) Mir, W. J.; Jagadeeswararao, M.; Das, S.; Nag, A. Colloidal Mn-Doped Cesium Lead Halide Perovskite Nanoplatelets. *ACS Energy Lett* **2017**, *2* (3), 537–543. https://doi.org/10.1021/acsenergylett.6b00741.

(110) Dong, Y.; Parobek, D.; Son, D. H. Controlling Quantum Confinement and Magnetic Doping of Cesium Lead Halide Perovskite Nanocrystals. *Journal of the Korean Ceramic Society* **2018**, *55* (6), 515–526. https://doi.org/10.4191/kcers.2018.55.6.11.

(111) Yuan, X.; Ji, S.; De Siena, M. C.; Fei, L.; Zhao, Z.; Wang, Y.; Li, H.; Zhao, J.; Gamelin, D. R. Photoluminescence Temperature Dependence, Dynamics, and Quantum Efficiencies in Mn2+-Doped CsPbCl3 Perovskite Nanocrystals with Varied Dopant Concentration. *Chemistry of Materials* **2017**, *29* (18), 8003–8011. https://doi.org/10.1021/acs.chemmater.7b03311.

(112) Fei, L.; Yuan, X.; Hua, J.; Ikezawa, M.; Zeng, R.; Li, H.; Masumoto, Y.; Zhao, J. Enhanced Luminescence and Energy Transfer in Mn2+ Doped CsPbCl3-: XBrx Perovskite Nanocrystals. *Nanoscale* **2018**, *10* (41), 19435–19442. https://doi.org/10.1039/c8nr05492d.

(113) Peng, W. Q.; Qu, S. C.; Cong, G. W.; Wang, Z. G. Concentration Effect of Mn2+ on the Photoluminescence of ZnS:Mn Nanocrystals. *J Cryst Growth* **2005**, *279* (3–4), 454–460. https://doi.org/10.1016/j.jcrysgro.2005.02.066.

(114) Choe, H.; Jeon, D.; Lee, S. J.; Cho, J. Mixed or Segregated: Toward Efficient and Stable Mixed Halide Perovskite-Based Devices. *ACS Omega* **2021**, *6* (38), 24304–24315. https://doi.org/10.1021/acsomega.1c03714.

(115) Cho, J.; Kamat, P. V. Photoinduced Phase Segregation in Mixed Halide Perovskites: Thermodynamic and Kinetic Aspects of Cl–Br Segregation. *Advanced Optical Materials*. 2021. https://doi.org/10.1002/adom.202001440.

(116) Protesescu, L.; Yakunin, S.; Bodnarchuk, M. I.; Krieg, F.; Caputo, R.; Hendon, C. H.; Yang, R. X.; Walsh, A.; Kovalenko, M. V. Nanocrystals of Cesium Lead Halide Perovskites (CsPbX3, X = Cl, Br, and I): Novel Optoelectronic Materials Showing Bright Emission with Wide Color Gamut. *Nano Lett* **2015**, *15* (6), 3692–3696. https://doi.org/10.1021/nl5048779.

(117) Cho, J.; Dubose, J. T.; Kamat, P. V. Charge Carrier Recombination Dynamics of Two-Dimensional Lead Halide Perovskites. *Journal of Physical Chemistry Letters* **2020**, *11* (7), 2570–2576. https://doi.org/10.1021/acs.jpclett.0c00392.

(118) Xu, K.; Meijerink, A. Tuning Exciton-Mn2+ Energy Transfer in Mixed Halide Perovskite Nanocrystals. *Chemistry of Materials* **2018**, *30* (15), 5346–5352. https://doi.org/10.1021/acs.chemmater.8b02157.

(119) Li, F.; Xia, Z.; Gong, Y.; Gu, L.; Liu, Q. Optical Properties of Mn2+ Doped Cesium Lead Halide Perovskite Nanocrystals: Via a Cation-Anion Co-Substitution Exchange Reaction. *J Mater Chem C Mater* **2017**, *5* (36), 9281–9287. https://doi.org/10.1039/c7tc03575f.

(120) Diroll, B. T.; Zhou, H.; Schaller, R. D. Low-Temperature Absorption , Photoluminescence , and Lifetime of CsPbX 3 (X = Cl , Br , I) Nanocrystals. **2018**, *3*, 1–7. https://doi.org/10.1002/adfm.201800945.

(121) Choe, H.; Jin, H.; Lee, S. J.; Cho, J. Exciton Recombination versus Energy Transfer: Mapping Competing Excited-State Dynamics in Various Mn-Doped CsPb(Cl1- YBr y)3Perovskite Nanocrystals for Achieving White Light Emission. *ACS Appl Nano Mater* **2022**, *5* (12), 18385–18395. https://doi.org/10.1021/acsanm.2c04208.

(122) Vegard, L. XV. Die Röntgenstrahlen Im Dienste Der Erforschung Der Materie. *Z Kristallogr Cryst Mater* **1928**, *67* (1–6), 239–259. https://doi.org/doi:10.1524/zkri.1928.67.1.239.

(123) Vegard, L. Die Konstitution Der Mischkristalle Und Die Raumfüllung Der Atome. *Zeitschrift für Physik* **1921**, *5* (1), 17–26. https://doi.org/10.1007/BF01349680.

(124) Tauc, J. Optical Properties and Electronic Structure of Amorphous Ge and Si. *Mater Res Bull* **1968**, *3* (1), 37–46. https://doi.org/https://doi.org/10.1016/0025-5408(68)90023-8.

(125) Rossi, D.; Liu, X.; Lee, Y.; Khurana, M.; Puthenpurayil, J.; Kim, K.; Akimov, A. V; Cheon, J.; Son, D. H. Intense Dark Exciton Emission from Strongly Quantum-Confined CsPbBr3 Nanocrystals. *Nano Lett* **2020**, *20* (10), 7321–7326. https://doi.org/10.1021/acs.nanolett.0c02714.

(126) Singh, R.; Liu, W.; Lim, J.; Robel, I.; Klimov, V. I. Hot-Electron Dynamics in Quantum Dots Manipulated by Spin-Exchange Auger Interactions. *Nat Nanotechnol* **2019**, *14* (11), 1035–1041. https://doi.org/10.1038/s41565-019-0548-1.

(127) Yang, X.; Pu, C.; Qin, H.; Liu, S.; Xu, Z.; Peng, X. Temperature- and Mn2+ Concentration-Dependent Emission Properties of Mn2+-Doped ZnSe Nanocrystals. *J Am Chem Soc* **2019**, *141* (6), 2288–2298. https://doi.org/10.1021/jacs.8b08480.

(128) De, A.; Mondal, N.; Samanta, A. Luminescence Tuning and Exciton Dynamics of Mn-Doped CsPbCl3 Nanocrystals. *Nanoscale* **2017**, *9* (43), 16722–16727. https://doi.org/10.1039/c7nr06745c.

(129) Pradeep, K. R.; Viswanatha, R. Mechanism of Mn Emission: Energy Transfer vs Charge Transfer Dynamics in Mn-Doped Quantum Dots. *APL Mater* **2020**, *8* (2). https://doi.org/10.1063/1.5140888.

(130) Xu, K.; Meijerink, A. Tuning Exciton-Mn2+ Energy Transfer in Mixed Halide Perovskite Nanocrystals. *Chemistry of Materials* **2018**, *30* (15), 5346–5352. https://doi.org/10.1021/acs.chemmater.8b02157.

(131) Rossi, D.; Parobek, D.; Dong, Y.; Son, D. H. Dynamics of Exciton-Mn Energy Transfer in Mn-Doped CsPbCl3 Perovskite Nanocrystals. *Journal of Physical Chemistry C* **2017**, *121* (32), 17143–17149. https://doi.org/10.1021/acs.jpcc.7b06182.

(132) Braham, E. J.; Cho, J.; Forlano, K. M.; Watson, D. F.; Arròyave, R.; Banerjee, S. Machine Learning-Directed Navigation of Synthetic Design Space: A Statistical Learning Approach to Controlling the Synthesis of Perovskite Halide

Nanoplatelets in the Quantum-Confined Regime. *Chemistry of Materials* **2019**, *31* (9), 3281–3292. https://doi.org/10.1021/acs.chemmater.9b00212.

(133) Braham, E. J.; Davidson, R. D.; Al-Hashimi, M.; Arróyave, R.; Banerjee, S. Navigating the Design Space of Inorganic Materials Synthesis Using Statistical Methods and Machine Learning. *Dalton Transactions* **2020**, *49* (33), 11480–11488. https://doi.org/10.1039/d0dt02028a.

(134) Yuan, H.; Qi, L.; Paris, M.; Chen, F.; Shen, Q.; Faulques, E.; Massuyeau, F.; Gautier, R. Machine Learning Guided Design of Single–Phase Hybrid Lead Halide White Phosphors. *Advanced Science* **2021**, *8* (19). https://doi.org/10.1002/advs.202101407.

(135) Noble, W. S. What Is a Support Vector Machine? *Nature Biotechnology*. 2006. https://doi.org/10.1038/nbt1206-1565.

(136) Altman, N. S. An Introduction to Kernel and Nearest-Neighbor Nonparametric Regression. *American Statistician* **1992**, *46* (3). https://doi.org/10.1080/00031305.1992.10475879.

(137) Breiman, L. Random Forests. *Mach Learn* **2001**, *45* (1). https://doi.org/10.1023/A:1010933404324.

(138) Friedman, J. H. Greedy Function Approximation: A Gradient Boosting Machine. *Ann Stat* **2001**, *29* (5). https://doi.org/10.1214/aos/1013203451.

(139) Geurts, P.; Ernst, D.; Wehenkel, L. Extremely Randomized Trees. *Mach Learn* **2006**, *63* (1). https://doi.org/10.1007/s10994-006-6226-1.

(140) Beaulac, R.; Archer, P. I.; van Rijssel, J.; Meijerink, A.; Gamelin, D. R. Exciton Storage by Mn2+ in Colloidal Mn2+-Doped CdSe Quantum Dots. *Nano Lett* **2008**, *8* (9), 2949–2953. https://doi.org/10.1021/nl801847e.

ABSTRACT IN KOREAN

개 요

최혜진
화학과
성신여자대학교 대학원

페로브스카이트에 전이 금속 도핑을 통해 페로브스카이트의 전기적, 자기적, 광학적 특성을 개선할 수 있다. 그러나 호스트 격자 내에서 엑시톤과 도펀트 사이의 에너지 전달을 정확히 이해하기 위해서는 여기된 상태에서 발생하는 복잡한 동역학에 대한 이해를 필요로 한다. Mn이 도핑된 페로브스카이트 나노크리스탈 내에서 Mn의 sensitization을 예측하기는 어려운데, 격자 내 호스트에서의 전자와 정공의 재결합, Mn에서의 재결합, 그리고 엑시톤과 Mn사이에서 발생하는 정방향 및 역방향의 에너지 전달 등이 여기상태에서의 상호작용을 복잡하게 하기 때문이다. 이 연구에서는 Mn 도펀트의 농도와 halide의 조성을 변화시켜 $\mathrm{CsPb(Cl_{1-y}Br_y)_3}$ 나노크리스탈 내에서 일어나는 exciton과 Mn 사이의 에너지 전달에 관한 동역학을 조사했다. 그리고 에너지 전달에 대해 더 정확한 예측을 얻고자 머신러닝 기법을 도입하였고, 총 86개의 실험데이터를 사용하여 K-nearest neighbor (KNN) 기반의 머신러닝 모델을 설계했다. 이를 통해 Mn의 농도, halide의 조성을 변화시켰을 때 엑시톤에서 Mn으로의 에너지 전달이 어떻게 변화하는지 정확하게 예측할 수 있었다. 또 time-correlated single photon counting (TCSPC)를 이용해 lifetime을 측정함으로써, Mn이 도핑된 페로브스카이트

내에서의 엑시톤−Mn의 에너지 전달에 관한 kinetic에 관한 정보를 얻을 수 있었다. 이러한 복잡한 에너지 전달 과정에 대한 이해는 Mn이 도핑된 페로브스카이트에서 발생하는 dual−emission을 더욱 효과적으로 이용할 수 있게 하는 정보를 제공한다. 또한 머신러닝 기반의 접근은 복잡한 특성을 가진 데이터로부터 패턴을 발견하고 원하는 결과를 더욱 쉽게 예측할 수 있도록 도와줌으로써 연구의 효율을 증가시킬 수 있다.